Formation and stability of hybrid perovskites

Dissertation

zur Erlangung des akademischen Grades

doctor rerum naturalium

(Dr. rer. nat.)
im Fach Chemie
eingereicht an der

Mathematisch-Naturwissenschaftlichen Fakultät
der Humboldt-Universität zu Berlin
von

Oleksandra Shargaieva, M.Sc.

Präsidentin der Humboldt-Universität zu Berlin
Prof. Dr.-Ing. Dr. Sabine Kunst

Dekan der Mathematisch-Naturwissenschaftlichen Fakultät
Prof. Dr. Elmar Kulke

Gutachter:	1. Prof. Dr. Norbert H. Nickel
	2. Prof. Dr. Klaus Rademann
	3. Prof. Dr. Norbert Koch
Tag der mündlichen Prüfung:	19.04.2018

Abstract

Hybrid perovskites such as methylammonium lead iodide, $CH_3NH_3PbI_3$, are one of the most promising absorber materials for photovoltaic energy conversion. Hybrid perovskites are solution processed and, thus, the material properties often are determined by the solution-based fabrication technique. Therefore, the first part of this thesis focuses on key aspects of the molecular interactions between precursors and solvents. Two types of PbI_2 complexes were detected in the solution. The first type corresponds to a complex between lead iodide and solvent molecules, while the second, even stronger complex, is formed between PbI_2 molecules only. Importantly, the formation of polyiodide plumbates was observed independently of the solvent choice or the presence of CH_3NH_3I. The polyiodide plumbates exhibited a photoluminescence peak located at 760 nm, similarly to $CH_3NH_3PbI_3$. This finding suggests a common origin of the excited state in PbI_2 complexes and $CH_3NH_3PbI_3$.

Despite the rapid development of perovskite solar cell efficiency, an assessment of the stability of devices and especially the active materials is required. Therefore, the thermal, compositional, and photostability of perovskite thin films were evaluated in the second part of this thesis. The thermal stability of $CH_3NH_3PbI_3$ thin films was studied by a post-annealing procedure. Above 190 °C, $CH_3NH_3PbI_3$ was found to degrade. However, $CH_3NH_3PbI_3$ exhibited a secondary grain growth at temperatures below the stability threshold. The secondary grain growth allowed to tune the grain size between 150 nm and 1 μm. As a result, a linear dependence of the diffusion length of charge carriers on the grain size was observed. In conjunction with increased grain size and diffusion length, the power conversion efficiency of $CH_3NH_3PbI_3$ solar cells increased. Next, the compositional stability of mixed $CsPb(I_{1-x}Br_x)_3$ perovskites was investigated. A fundamental miscibility gap between $0.3 < x < 1$ was demonstrated, that impedes the preparation of high band-gap perovskites. To overcome this intrinsic instability, a new approach for band-gap engineering was developed. An addition of ethylenediammonium diiodide (EDDI) allowed to alter the band gap of $CH_3NH_3PbI_3$ from 1.6 to 1.8 eV.

Finally, the influence of light on the stability of hybrid perovskites was studied. The changes in $CH_3NH_3PbI_3$ thin films were monitored on a molecular level during illumination by means of *in-situ* Fourier-transform infrared spectroscopy. A degradation of $CH_3NH_3PbI_3$ was observed through photo-dissociation of N-H bonds with $h\nu \geq 2.72$ eV. A similar behavior was demonstrated in formamidinium lead iodide, $CH(NH_2)_2PbI_3$, as well as mixed Cs and formamidinium perovskites. In addition, the photo-dissociation of PbI_2 to Pb^0 was observed under prolonged illumination.

Kurzzusammenfassung

Hybridsolarzellen auf Basis von Perowskit-Absorbern, wie zum Beispiel Methylammoniumbleitriiodid ($CH_3NH_3PbI_3$), stellen eine der vielversprechendsten Solarzellenkonzepte der heutigen Zeit dar. Perowskitschichten werden typischerweise aus Lösung abgeschieden, was erheblichen Einfluss auf die Materialeigenschaften hat. Entscheidend dabei sind die molekularen Wechselwirkungen zwischen den Ausgangsstoffen und den gewählten Lösungsmitteln. In dieser Arbeit wird zunachst die Bildung von zwei verschiedenen Bleiiodid(PbI_2)-Komplexen in Lösung festgestellt. Der erste Komplextyp ist aus PbI_2- und Lösungsmittelmolekülen zusammengesetzt, während der zweite Typ vollständig aus PbI_2-Molekülen besteht. Die Bildung von Polyiodidplumbaten, konnte unabhängig von dem gewählten Lösungsmittel, sowie unabhängig von der Beigabe von Methylammoniumiodid (CH_3NH_3I), beobachtet werden. Die Photolumineszenz dieser Polyiodidplumbate lag, ähnlich dem von $CH_3NH_3PbI_3$, bei 760 nm. Diese Ähnlichkeit lässt auf einen gemeinsamen Ursprung des angeregten Zustandes in PbI_2-Komplexen und $CH_3NH_3PbI_3$ schließen.

Im Rahmen dieser Arbeit wurden darüber hinaus die Lichtbeständigkeit, die thermische Stabilität und die Stabilität der chemischen Zusammensetzung untersucht. Die thermische Stabilität dünner $CH_3NH_3PbI_3$-Filme wurde mit Hilfe eines an die Herstellung der Schichten anschließendes Temperverfahren analysiert. Oberhalb einer Temperatur von 190 °C kam es dabei zur Zersetzung des Materials. Unterhalb dieser Stabilitätsgrenze konnte ein sekundäres Kristallwachstum beobachtet werden, wodurch die durchschnittliche Kristallgröße gezielt zwischen 150 nm und 1 µm variiert werden konnte. Ein linearer Zusammenhang zwischen der Diffusionslänge der Ladungsträger und der Kristallgröße konnte festgestellt werden, welcher darüber hinaus mit einer Effizienzsteigerung der $CH_3NH_3PbI_3$-Solarzellen einherging. Die Stabilität der chemischen Komposition wurde anhand von unterschiedlich zusammengesetzten $CsPb(I_{1-x}Br_x)_3$-Perowskiten untersucht. Die Herstellung von Perowskiten mit einer großen Bandlücke war zunächst nicht möglich, da es bei den dafür notwendigen Kompositionen ($0.3 < x < 1$) zur Phasentrennung kommt. Im Gegensatz dazu konnte durch den Zusatz von Ethylendiammoniumdiodid (EDDI) zum $CH_3NH_3PbI_3$ die Bandlücken zwischen 1.6 und 1.8 eV variiert werden.

Die Lichtstabilität von $CH_3NH_3PbI_3$, $CH(NH_2)_2PbI_3$, sowie $Cs_y(CH(NH_2)_2)_{1-y}PbI_3$ wurde mittels *in-situ* Infrarotspektroskopie analysiert. Die Zersetzung des Materials war durch die lichtinduzierte Spaltung der N-H-Bindungen bei $h\nu \geq 2.72$ eV gekennzeichnet. Weiterhin konnte eine Degradation von PbI_2 zu Pb^0 bei längerer Belichtung festgestellt werden.

Table of Contents

1. Introduction

In 2016 the annual global generation of energy by photovoltaics (PV) amounted to 74 GW with a projection to reach up to 920 GW by 2022.[1] Similarly, an increase in the global contribution from renewable energy sources was predicted from 24 % in 2016 to 30 % by 2022. This future growth will allow to reduce the consumption of natural resources such as coal or gas and, simultaneously, will reduce the CO_2 emission. Typically, the solar PV market is dominated by mature technologies such as solar cells based on crystalline Si (c- Si) or GaAs and thin film technologies such as copper indium gallium selenide (CIGS), CdTe, GaAs, and amorphous Si (a-Si).

Since the first certified solar cells in 1976, the power conversion efficiency of such devices increased drastically to 26.6 % for c-Si and 14 % for a-Si in 2017 (Figure 1).[2] In addition, new emerging materials were applied as absorbers in PV devices. The new absorber materials included dyes, semiconducting polymers, various types of quantum dots, and hybrid perovskites. The attention to these new materials was driven by the swift increase in the efficiency of such devices, their low production costs and ease of manufacturing. Currently, hybrid perovskites are the leaders of power conversion efficiency among other solution-processed materials, yielding 22.7 %.[2] Such a vast increase of efficiency resulted in an extensive study of the properties of materials and accelerated commercialization in the future.

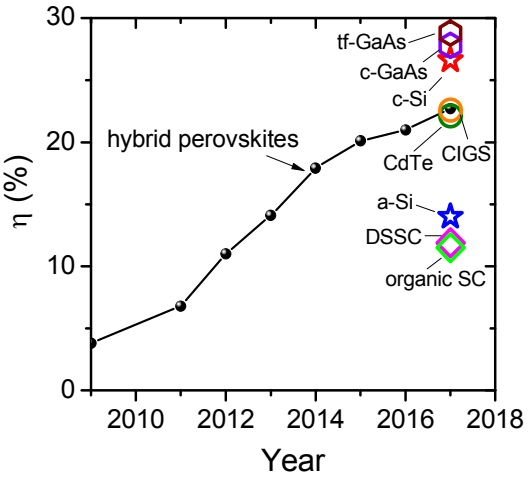

Figure 1. Development of the power conversion efficiency, η, of perovskite solar cells in comparison to other conventional and emerging PV materials such as thin film GaAs (tf - GaAs), crystalline GaAs (c-GaAs), crystalline Si (c-Si), CdTe, copper indium gallium selenide (CIGS), amorphous Si (a-Si), organic and dye-sensitized solar cells (DSSC).[2]

Hybrid perovskites can be processed from solution by spin-coating or by applying large-scale coating techniques as printing or doctor blading.[3,4] The layer is, then, converted to the perovskite phase by a low-temperature annealing at 100 °C. The processing of the perovskite-based devices involves usage of unexpansive abundant materials and solvents.[5] Despite the simplicity of manufacturing, the materials show a high quality of the polycrystalline thin films. For example, values of about 1 μm for the diffusion length were reported in thin films.[6–8] This is accompanied by a relatively high mobility of the charge carriers of about 10^3 $cm^2V^{-1}s^{-1}$ in thin films and a high defect tolerance.[9–12]

The combination of the simple preparation process and the outstanding optoelectronic properties makes perovskites not only promising materials for the solar cells but also attractive for many other applications. The band gap tunability in the visible range of hybrid perovskites makes these materials ideal for the use in tandem solar cells or as colourful light emitting diodes (LED).[13–17] Numerous reports have shown bright LEDs with an emission wavelength in the range from 400 to 800 nm with an external quantum efficiency of about 4 % and above 10 % in hybrid perovskites quantum dots.[18,19] Moreover, hybrid perovskites can be used for detection of photons from the visible range to gamma- and x-ray radiation.[20,21]

Outline of this work

A rapid development of the power conversion efficiency of solar cells and the applicability of the hybrid perovskites in other devices requires a better understanding of the processes occurring in the material from solution to the solid phase. Therefore, the goal of this work was divided between two main topics concerning solution chemistry of hybrid perovskites and stability of perovskite thin films. The aim of the first part is to understand the influence of the preparation conditions on the properties of perovskite thin films. Specifically, the role of intramolecular interactions was investigated between precursor compounds and solvents. Importantly, the formation of different complexes was demonstrated and the properties of such complexes were linked to the properties of the resulting $CH_3NH_3PbI_3$ thin films. The second part of this thesis focuses on the thermal, compositional, and photostability of hybrid perovskites. First, the thermal stability was investigated by studying the influence of various temperatures on the optical and electronic properties of $CH_3NH_3PbI_3$ perovskite layers. Then, the compositional stability was examined in mixed halide $CsPb(I_{1-x}Br_x)_3$ perovskites revealing a fundamental miscibility gap. In addition, this study further demonstrates a successful stabilization of the α-phase of $CsPbI_3$ and band-gap tuning in $CH_3NH_3PbI_3$ by the addition of lager cation, ethylenediammonium diiodide. Finally, light-induced degradation was

demonstrated on a molecular level in $CH_3NH_3PbI_3$ and formamidinium lead iodide, $CH(NH_2)_2PbI_3$.

Chapter 2 gives an introduction to organic-inorganic perovskites, their structure and their optoelectronic properties. The structure and working principles of perovskite solar cells are discussed. In addition, an overview of the different degradation pathways is given for hybrid perovskites and perovskite-based devices.

Chapter 3 contains a description of the experimental methods used within this thesis including the preparation of precursor solutions, deposition and post-treatment techniques. Also, the fabrication procedures for manufacturing of perovskite solar cells are described. In addition, key characterization techniques and their application for investigation of both thin films and devices are discussed in this chapter.

Chapter 4 presents on the main results obtained within this thesis:

Chapter 4.1 describes processes that occur in the precursor solution of $CH_3NH_3PbI_3$. Specifically, intramolecular interactions of precursors with solvents were investigated, as well as the formation of polyiodide plumbate complexes.

Chapter 4.2 discusses the influence of temperature, composition, and light on the optical and electronic properties of hybrid perovskite thin films and solar cells.

Chapter 5 contains the interpretation of the obtained results from Chapter 4 including necessary models and relevant background for an understanding of the results.

Chapter 6 provides with a summary of this thesis and an outlook.

2. Fundamentals

This chapter presents a literature overview required for the understanding of the work presented in this thesis. It provides a background knowledge of the perovskite structure, the optical and electronic properties of hybrid perovskites, as well as the structure and working principles of perovskite solar cells. In addition, different aspects of stability of perovskite thin films and perovskite-based solar cells are reviewed. In particular, the influence of temperature, water, composition, and light are closely revised within this chapter.

2.1. Organic-inorganic perovskites

Hybrid perovskites are a family of materials which follow the general formula ABX_3. The structure and the name of hybrid perovskites were adapted from inorganic oxide perovskites. The first representative of inorganic perovskites, calcium titanate $CaTiO_3$, was found in 1839 in the Ural Mountains by German mineralogist and geologist Gustav Rose and named after Russian mineralogist and nobleman Lev Perovski. Nowadays, the name perovskite combines within itself many materials, which all share the same crystalline structure ABX_3 including hybrid perovskites. Inorganic perovskites typically consist of A (Ca, Ba, Sr) - a large cation with the oxidation state of +2, B (Ti, Si, Fe) – a smaller cation with oxidation state of +4, and X (O, S, Te) is an anion with oxidation state of -2.[22,23] In hybrid perovskites, A is monovalent organic cation, B is a divalent inorganic cation, and X is a halide anion (Figure 2). Within the perovskite structure, materials can be formed in several possible symmetries such as orthorhombic, tetragonal, and cubic. In the ideal cubic structure, the materials consist of octahedra formed by BX_6, where B takes a central position and X is located at the vertices of the octahedra. The A-site cation resides in the cuboctahedral cavity formed by eight BX_6 octahedra.

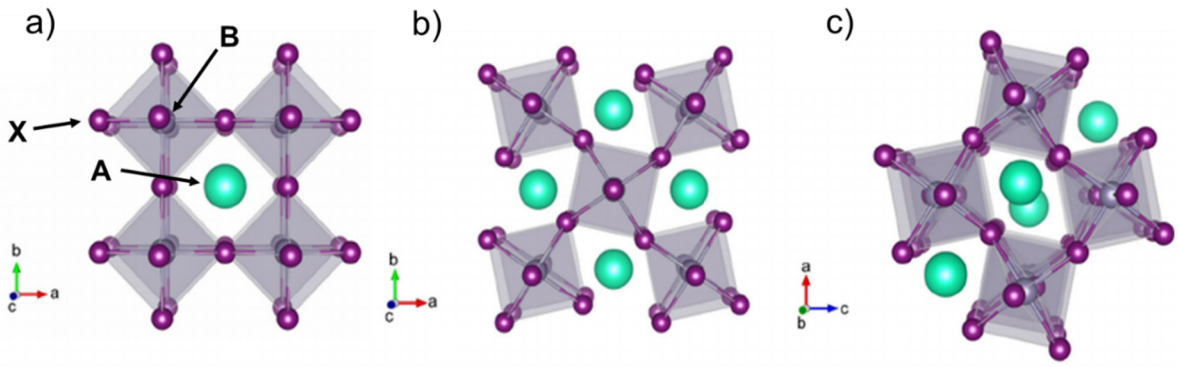

Figure 2. Schematic representation of perovskite structures with (a) cubic, (b) tetragonal, and (c) orthorhombic symmetry, where A is a large cation, B is a smaller cation, and X is an anion. Reprinted figure with permission from Ref.[24] Copyright 2015 by the American Physical Society.

2.2. Properties of hybrid perovskites

2.2.1. Structural properties of hybrid perovskites

The detailed perovskite structure was analyzed by Victor Moritz Goldschmidt in 1926.[25] The analysis resulted in a formulation of the empirical rule, known as Goldschmidt tolerance factor, which can be used to predict the compatibility of ions within the perovskite structure. The rule is based on a calculation of the tolerance factor (t) according to the formula:

$$t = \frac{r_A + r_X}{\sqrt{2(r_B + r_X)}} \quad (1)$$

where r_A, r_B, and r_X are ionic radii of A, B, and X, respectively. According to Goldschmidt, a stable perovskite structure can be formed when $0.71 < t < 1$. Moreover, materials, which have a tolerance factor between 0.9 and 1, form a stable perovskite material with the ideal cubic structure, e.g. $BaTiO_3$. Tolerance factors between $0.71 < t < 0.9$ indicate a small mismatch between the ion's sizes, commonly the A-site cation is smaller than a cuboctahedral cavity. This mismatch lowers the symmetry of the crystal to tetragonal or orthorhombic, e.g. $CaTiO_3$. However, when the A-site cation is too large or too small to form the perovskite structure, the tolerance factor increases above 1 or t decreases below 0.71, respectively. Consequently, such materials, possess a hexagonal or a trigonal crystal symmetry and no longer form a stable perovskite structure.

In the same way, the Goldschmidt tolerance factor can be used to predict the crystalline structure and the stability of hybrid perovskites.[26] Unlike inorganic perovskites, hybrid perovskites are fully synthetic materials. Therefore, the family of hybrid perovskites is not limited and can be easily extended by designing the organic counterpart to fit the Goldschmidt tolerance factor in the perovskite structure.[27,28] Currently, organic ammonium cations are used as the A-site cation and typically represented by methylammonium or formamidinium ions, B often corresponds to the Pb^{2+}, Sn^{2+} or Ge^{2+} cation, while X is the iodide, bromide, or chloride anion.[29] The tolerance factors of some of the most common hybrid perovskites are presented in Figure 3.[30] Formamidinium- and cesium-based lead iodide perovskites exhibit a small mismatch of the ionic radii with the cuboctahedral cavity resulting in the tolerance factor of 1.03 and 0.78, respectively. Thus, both materials exist in the non-perovskite δ-phase at room temperature. However, the materials undergo a high-temperature phase transition to the perovskite α-phase.[31] The tolerance factors of the high-temperature stable α-phase are marked with open symbols, room temperature phases are marked with solid symbols.

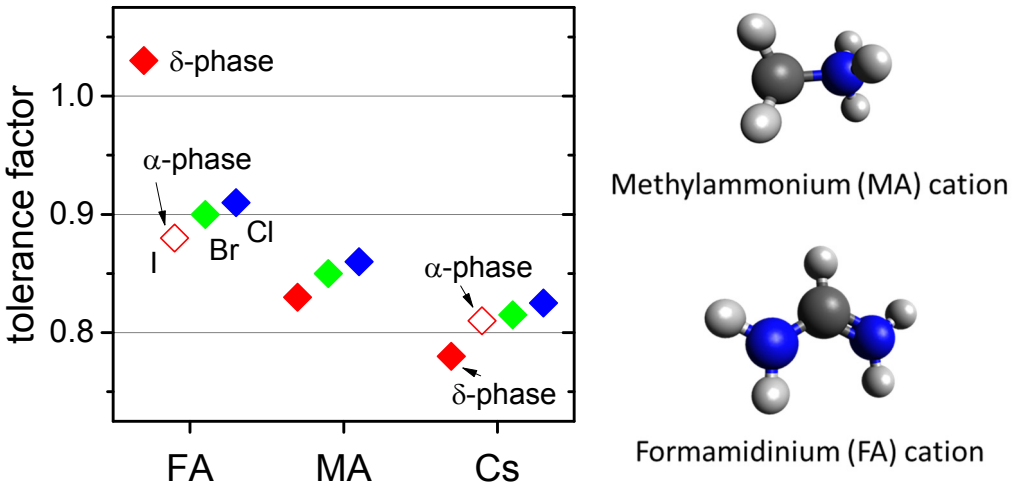

Figure 3. Summarized tolerance factors of lead-based $APbX_3$ hybrid perovskites reported in literature, where A is formamidinium (FA), methylammonium (MA), and cesium (Cs); X is I, Br, and Cl depicted with red, green, and blue symbols respectively. Open symbols indicate high-temperature stable α-phase and filled symbols indicate the values calculated for room temperature stable phases.

2.2.2. Optical properties of hybrid perovskites

Among many reported hybrid perovskites, methylammonium lead iodide ($MAPbI_3$ or $CH_3NH_3PbI_3$) forms a room-temperature stable perovskite phase and has a band gap in the appropriate range for the use in photovoltaic devices. Therefore, it will hereafter be used as an example for a discussion of the optical and electronic properties of hybrid perovskites.

Methylammonium lead iodide, as well as all hybrid perovskites, is a direct semiconductor with a band gap of about 1.6 eV.[32] The calculated band structure corresponding to the cubic structure and three-dimensional sketch of the first Brillouin zone of the *Pm3m* space group are presented in Figure 4. It is commonly agreed that the valence bands of $CH_3NH_3PbI_3$ are formed by antibonding I 5p and Pb 6s orbitals. The conduction bands are formed by Pb 6p orbitals and I 5p orbitals.[33] The contribution from the organic cation is located deeper in the bands, therefore they do not contribute to the band to band transitions.[30,34] However, it is conceivable that the organic cation stabilizes the perovskite structure. The size of the organic cation determines the distances and angles between B and X, which are strongly influencing the band gap energy and are closely related to the absorption and emission properties of the material.

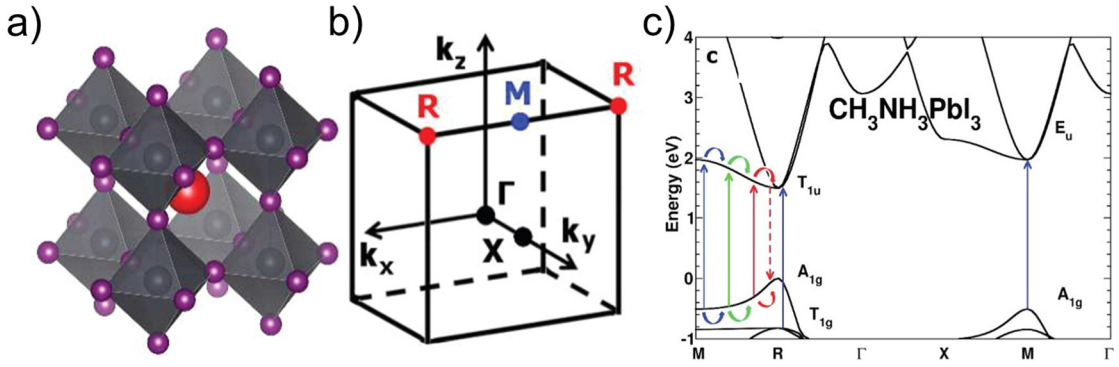

Figure 4 (a) 3D view of the *Pm3m* cubic crystal structure of metal-halide hybrid perovskites, (b) Reciprocal-space 3D view showing the first Brillouin zone (BZ) of the *Pm3m* space group. Points of high symmetry in the cubic BZ are indicated by conventional letters: Γ denotes the origin of the BZ, X is the center of a square face at the BZ boundary, M is a center of a cube edge, and R are vertices of the cube. (c) Electronic band structure for the high-temperature cubic *Pm3m* phase of $CH_3NH_3PbI_3$ at the LDA (local density approximation) level of theory. Adapted with permission from Ref. [35] Copyright 2014 American Chemical Society.

Figure 5 (a) presents typical absorption and emission spectra of methylammonium lead iodide at room temperature.[36] Methylammonium lead iodide exhibits a strong absorption in the visible part of the spectrum. In comparison to many conventional semiconductors, hybrid perovskites have an extremely high absorption coefficient due to the direct nature of their band gap accompanied by a sharp absorption edge (Figure 5b).[37] Such high absorption coefficient allows an efficient application of perovskites as a thin film absorber material in solar cells. Moreover, several studies have shown that even ≈ 500 nm thick perovskite layers enable more than 20 % maximum power conversion efficiency of a solar cell.[38–40] However, absorption of the material can be altered by changing the crystalline properties of the absorber layer. For example, poor crystallinity and the presence of defects or impurities strongly influences the optical properties of the material. In the same way as in conventional semiconducting materials, defect and disorder related transitions within the band gap of hybrid perovskites induce an exponential absorption tail, known as the Urbach tail (Figure 5b). The Urbach tails are attributed to the transitions between band tails below the band edges and follow the dependence:

$$\alpha(E) = \alpha_g \, exp(\frac{h\nu}{E_u}) \tag{2}$$

where E_u is the Urbach energy.

The Urbach energy strongly depends on the material quality and the presence of defects. In addition, the value of the Urbach energy can be altered by a deposition method or simply a substrate below the material. Therefore, it can influence the absorption spectrum of the material and the accuracy of the band gap calculation. For methylammonium lead iodide, values between 15 and 30 meV were reported in literature.[41–43] The values are comparable with the Urbach tail energies obtained for many inorganic semiconductors and below values reported for amorphous silicon (E_u = 50 meV) (Figure 5c).

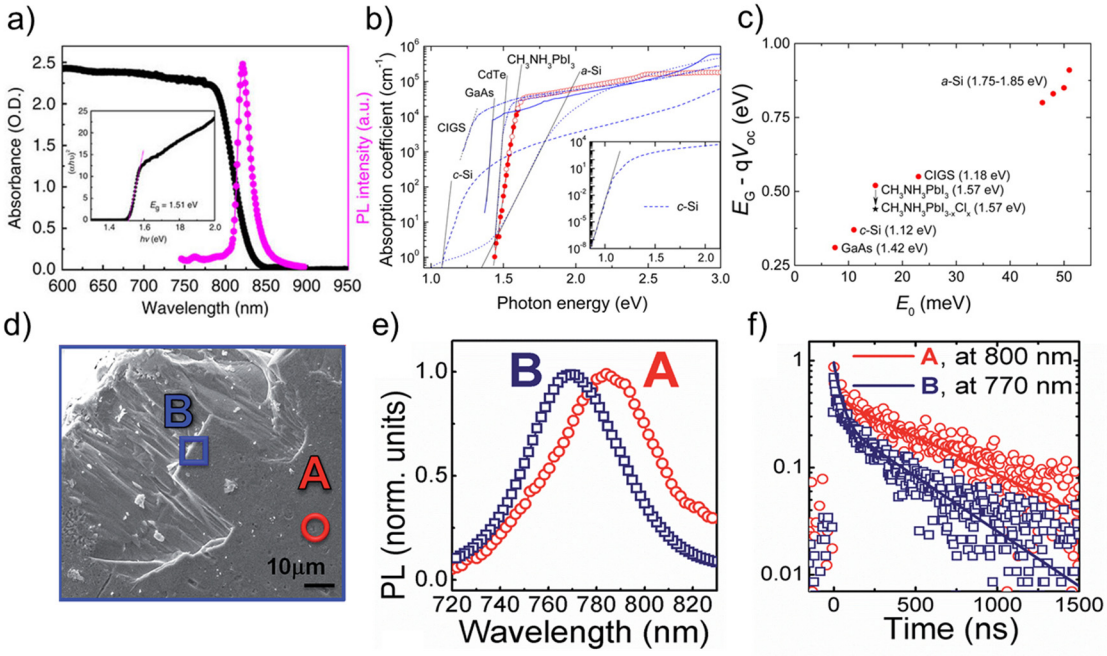

Figure 5. (a) Absorption and photoluminescence spectra of $CH_3NH_3PbI_3$. Adapted from Ref.[36] (b) Absorption coefficient and (c) the slope of the Urbach tail of $CH_3NH_3PbI_3$ in comparison to crystalline silicon (c-Si), amorphous silicon (a-Si), gallium arsenide (GaAs), and copper indium gallium diselenide (CIGS). Adapted with permission from Ref. [37] Copyright 2014 American Chemical Society. (d) Top view SEM image of a mm-sized $CH_3NH_3PbI_3$ single crystal, where spot A and B have been measured, respectively. (e) PL spectra on spot A and B upon excitation at 690 nm (fluence ~ 10 µJ cm^{-2}) under a N_2 atmosphere; (f) PL time decays at 770 nm (peak maximum of point B) and 800 nm (peak maximum of point A). Adapted from Ref. [44] 2015 - Published by The Royal Society of Chemistry.

In addition, the presence of defects and surface inhomogeneities may alter the width, intensity and the position of the photoemission of semiconductors. Grancini et al. reported the presence of an additional photoluminescence (PL) peak at higher energies corresponding to the morphological inhomogeneities (Figure 5d, e).[44] A contribution of the emission induced by the defects states results in a shift of the overall photoluminescence spectrum of methylammonium

lead iodide to smaller wavelengths. In addition, the contribution from local distortions influences strongly the time of the photoluminescence decay. The transient photoluminescence measurements showed that a short-lived part of the decay dominates in the distorted part of the material (Figure 5f). Such strong dependence of the physical properties on the material quality results in a vast difference between reported values of the band gap between 1.55 and 1.63 eV for $CH_3NH_3PbI_3$.[33,45–47] Therefore, it is necessary to analyze the electronic properties of the studied materials to avoid the influence of defects and inhomogeneities when determining the optical properties.

2.2.3. Electronic properties

Similarly to the optical properties, the electronic properties also dependent on the properties of the material. Diffusion lengths rendering between 100 nm and 175 µm were reported in the literature.[6–8,48] This broad distribution of the measured values is caused by the different fabrication processes, e.g. choice of solvents, annealing, and precursor compounds. The record diffusion lengths were measured on single crystals, while lower values are typically measured in polycrystalline thin films. Commonly, the diffusion length of hybrid perovskites derived from photoluminescence decay measurements using the diffusion model. According to the model, the diffusion length (L) is calculated from the equation:

$$L = \sqrt{D\tau_e} \tag{3}$$

where D is the diffusion coefficient and τ_e is the recombination lifetime. In thin films, the diffusion length values ranging between 100 to 1000 nm are typically reported.[7,8,48,49] Interestingly, the values of the diffusion length depend strongly on the morphology and the composition of the thin film. Commonly, pristine $CH_3NH_3PbI_3$ exhibited values of about L_e = 129 nm and L_h = 105 nm corresponding to the diffusion length of electrons and holes, respectively.[8] The addition of a small amount of Cl led to a drastic increase of the grain size and subsequently the diffusion length rose to about L_e = 1069 nm and L_h = 1213 nm. Moreover, values for the charge carrier diffusion length exceeding 175 µm were reported in perovskite single crystals by Dong et al.[50] The diffusion length was calculated from lifetime (τ) and mobility (μ) measurements according to the equation:

$$L = \sqrt{\mu \frac{kT}{e} \tau_e} \tag{4}$$

where k, T, and e are the Boltzmann constant, temperature, and the elementary charge, respectively. The hole- and electron-only devices were built from thick single crystals to perform mobility and trap density measurements. Dark current measurements of such devices exhibited a large mobility of holes μ_h = 164 $cm^2V^{-1}s^{-1}$ and electrons of μ_e = 24.8 $cm^2V^{-1}s^{-1}$. Similar values of the mobility were obtained from Hall measurements for holes μ_h = 105 $cm^2V^{-1}s^{-1}$ and from time-of-flight measurements for electrons μ_e = 24.0 $cm^2V^{-1}s^{-1}$. Combining these values of μ with the lifetime of $\tau \approx 90$ μs obtained from transient photovoltage and impedance spectroscopy, a large diffusion length of the charge carriers, $L >$ 175 μm was obtained. It is possible that larger values of L are attributed to the thin films and especially to single crystals with enhanced crystalline quality. However, there is no direct proof of this correlation reported in the literature so far. Therefore, the influence of morphology on electronic properties of the material and correlation with photovoltaic performance will be further studied in Chapter 4.2.1.

2.3. Perovskite solar cells

A perovskite solar cell is a photovoltaic device where the hybrid perovskite is used as an active light-harvesting layer. Typically, the device consists of selective transport layers for electrons and holes and an absorber layer sandwiched between them. The structure follows a heterojunction concept. Depending on the type of the contact through which the device is illuminated, the structure of the solar cell is divided into regular (n-i-p) and inverted (p-i-n) architecture (Figure 6).

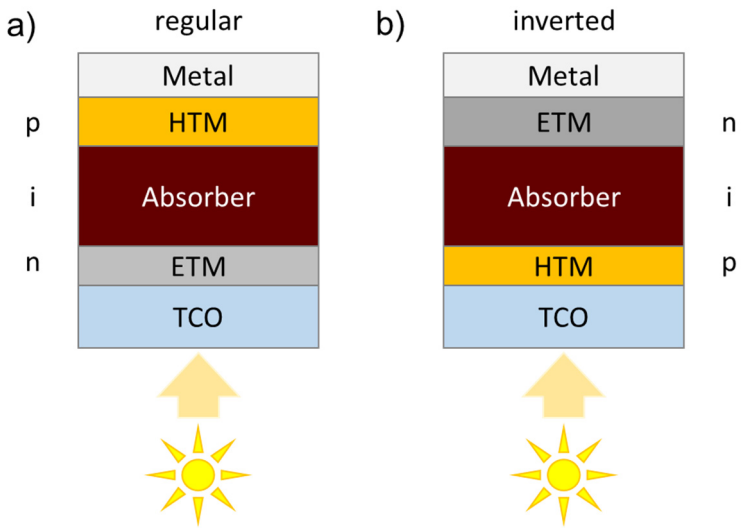

Figure 6. The structure of a solar cell with (a) regular and (b) inverted structure.

Nevertheless, the mechanism of generation, transport, and extraction of the charge carriers is identical for both types of the devices. First, the charge carrier generation takes place under illumination of a device. The photons with an energy, E_{ph}, larger than the band gap E_g ($E_{ph}>E_g$) are absorbed into an active material, e.g. perovskite. The absorption of photons results in an excitation of electrons from the valence band to the conduction band of the semiconductor. The charge carriers are, then, transferred to the corresponding selective contacts by the build-in potential. Then, the carriers, which came into contact with appropriate selective contacts, are extracted towards the external circuit. Figure 7 shows the process of the charge carrier generation and extraction in the device.

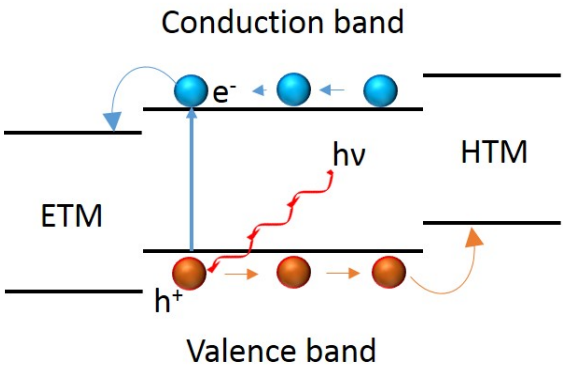

Figure 7. Schematic representation of the charge generation and extraction in a solar cell.

In general, certain energy level alignment needs to be fulfilled for an efficient extraction of the carriers. Figure 8 represents energy alignment and chemical structure of different materials often used as hole and electron extraction layers in perovskite solar cells. Therefore, the choice of materials used as selective contacts depends strongly on a band gap of the active layer.

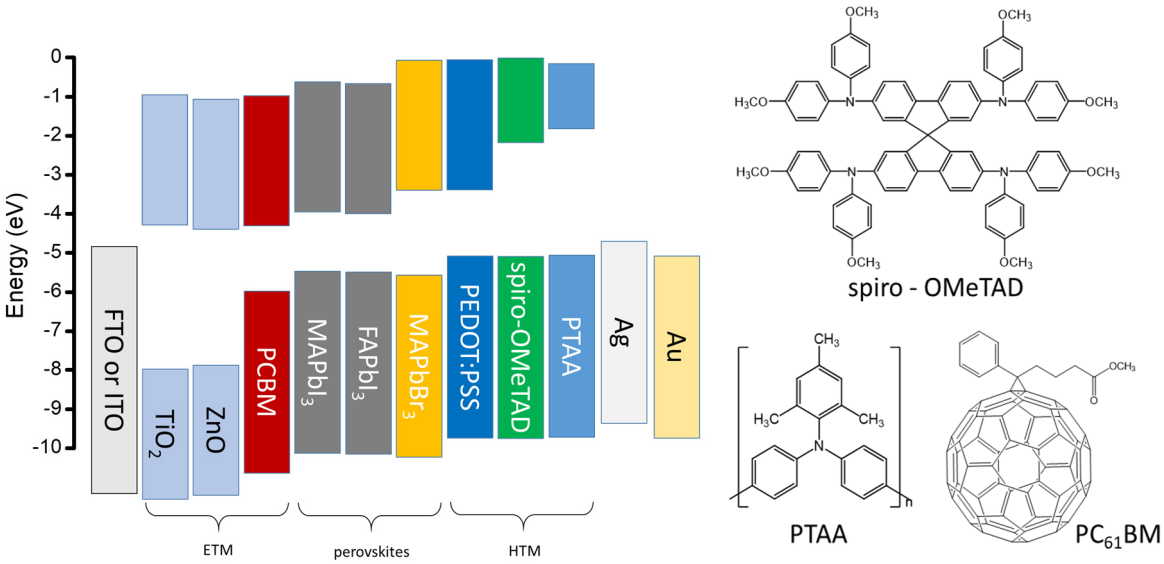

Figure 8. Energy alignment of typical electron transport materials (ETM): titanium oxide, zinc oxide, and PCBM (Phenyl-C61-butyric acid methyl ester), hybrid perovskites, and hole transport materials (HTM): PEDOT:PSS (poly(3,4-ethylenedioxythiophene) polystyrene sulfonate), PTAA (Poly[bis(4-phenyl)(2,4,6-trimethylphenyl)amine]), Spiro-OMeTAD (N^2,N^2,$N^{2'}$,$N^{2'}$,N^7,N^7,$N^{7'}$,$N^{7'}$-octakis(4-methoxyphenyl)-9,9′-spirobi[9H-fluorene]-2,2′,7,7′-tetramine).

Successful extraction of the photo-generated charge carriers results in the energy conversion. The ratio between the electrical power generated by a solar cell and the number of photons incident on the device is called power conversion efficiency (PCE or η). The

theoretical maximum of a solar cell efficiency was first calculated by William Shockley and Hans-Joachim Queisser and is currently known as the Shockley-Queisser limit.[51] Shockley and Queisser calculated the maximum efficiency of an ideal single-junction solar cell when only limited by absorption and re-emission processes, as a function of the band gap. According to Shockley and Queisser, the limit of the maximum efficiency for a single junction solar cell amounts to about 33.5 % and is achievable in materials with a band gap in the range between 1.1 and 1.4 eV (Figure 9).

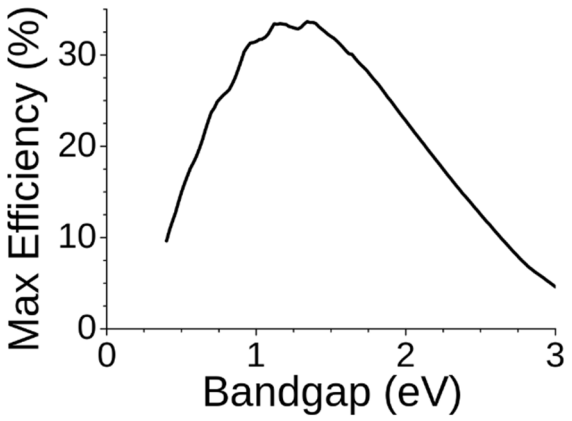

Figure 9. Dependence of maximum efficiency of an ideal photovoltaic device as a function of the band gap energy according to the Shockley-Queisser limit.

Currently, state-of-the-art hybrid perovskite devices reach power conversion efficiencies of 22.7 %.[2] Moreover, the theoretical efficiency of hybrid perovskites with a band gap of about 1.5 eV can reach 32 % of PCE. However, the Shockley-Queisser limit for a single junction solar cells can be surmounted. One of the possible routes is an application of a tandem device. In a multi-junction device, the solar spectrum can be distributed between two or more materials with different band gaps. This allows to reduce thermalization losses and to maximize the absorption. In tandem devices where hybrid perovskites with a large band gap are used as the top cell and crystalline silicon is used as a bottom cell, theoretical values of the PCE can reach as high as 40 %.[52]

2.4. Stability of hybrid perovskites

2.4.1. Thermal and moisture stability

Hybrid perovskites combine the advantageous properties from both, its organic and inorganic component. While the organic components allow an easy solution-based deposition and a broad tunability of the optical and electronic properties, they are also the source of the poor stability of hybrid perovskites. In case of the stability issues, hybrid perovskites are suffering from different degradation pathways related to temperature, humidity, composition, and light. All of which lead to the decomposition under certain conditions. However, some of the decomposition pathways can be suppressed or avoided, even under operational conditions of photovoltaic devices. Temperature- and humidity-driven degradation can be attributed to this category. On the one hand, several reports have demonstrated the destructive influence of temperature on hybrid perovskites and, especially on methylammonium lead iodide. Dualeh et al. have reported a drastic drop in the device performance when samples were annealed at high temperature.[53] On the other hand, substitution of methylammonium cation with another cation such as formamidinium or cesium leads to a noticeable enhancement of the thermal stability of hybrid perovskites. Pure formamidinium lead iodide exhibited remarkable thermal stability up to 170 °C.[54,55] Similarly, perovskites based on cesium as the A-site cation are often annealed at temperatures around 350 °C during preparation.[56] Mixed formamidinium and cesium hybrid perovskites showed no changes in the properties when annealed at 170 °C similarly to their pure predecessors.[31] Moreover, such mixed cation perovskites exhibited not only an improved stability towards high temperatures but towards humidity as well (Figure 10).[57]

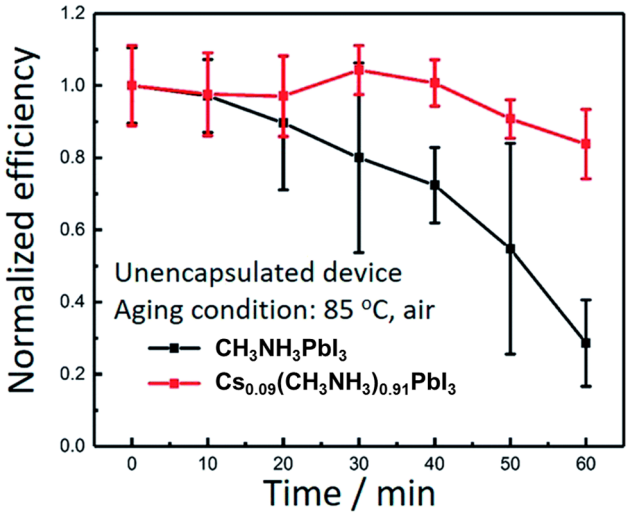

Figure 10. Dependence of the normalized efficiency of the solar cells based on $CH_3NH_3PbI_3$ and $Cs_{0.09}(CH_3NH_3)_{0.91}PbI_3$. Adapted from Ref. [57] 2017 - Published by The Royal Society of Chemistry.

The moisture or water-induced instability of hybrid perovskites is related to a rapid hydrate formation. Leguy et al. showed that an absorption of water molecules by methylammonium lead iodide is directly followed by the formation of hydrate complexes.[58] The process of the interaction of $CH_3NH_3PbI_3$ with H_2O consists of two steps: formation of monohydrate and dihydrate. The former is reversible by annealing of the material in dry conditions. However, further exposure to water leads to the formation of dihydrate. This process is accompanied by the formation of lead iodide and water molecules:

$$(CH_3NH_3)PbI_3 + 4\ H_2O \rightleftarrows [CH_3NH_3PbI_3 \cdot H_2O]$$

$$4[CH_3NH_3PbI_3 \cdot H_2O] \rightleftarrows (CH_3NH_3)_4PbI_6 \cdot 2H_2O + 3PbI_2 + 2H_2O$$

The process is further promoted by a phase segregation of the dihydrate from the monohydrate and the pristine material. Moreover, the different solubility of the precursors in water results in prior dissolution of the methylammonium salt resulting in the formation of lead iodide:

$$(CH_3NH_3)_4PbI_6 \cdot 2H_2O(s) \rightarrow 4CH_3NH_3I\ (l) + PbI_2(s) + 2H_2O$$

The influence of water can be avoided by a proper encapsulation. Another approach to avoid this decomposition pathway is realized by chemical modification of the material itself or selective transport layers. For example, several reports have demonstrated an improved stability by using a layer of hydrophobic molecules as barrier or transport layers.[59–62] In addition, a similar approach can be applied for the protection of perovskite on a molecular level. For instance, a surfactant containing long alkyl chains can be added to a perovskite precursor solution.[63,64] An addition of surfactant leads to the formation of low dimensional materials, where hydrophobic alkyl groups act as a protective coating for perovskite nanocrystals. Numerous reports have indicated a drastic improvement of the stability of photovoltaic devices based on 2D perovskites.[65–68] Lifetime beyond 10,000 h has been demonstrated for solar cells based on such 2D/3D perovskites.[69]

2.4.2. Compositional stability

The properties of hybrid perovskites can be easily tailored by adjusting the composition of the material. Blending two perovskites with different band gaps allows obtaining the material with an intermediate value of the band gap.[70] Moreover, altering the ratio between components enables a tuning of the band gap in a range between values of pure precursors. It has been shown, that the resulting band gap of a mixed perovskite can be estimated with the Vegard's

law.[71] The Vegard's law was developed for a prediction of lattice parameters of a solid solution of two components, where the lattice parameter can be calculated according to the equation:

$$a_{A_{(1-x)}B_x} = (1-x)a_A + xa_B \quad (5)$$

where a_A and a_B are lattice parameters of pure A and B components respectively, and x is a molar fraction of B component in the mixture. Since many properties of materials depend on lattice parameters, the Vegard's law can be adapted for calculation of the band gap, E_g, for example:

$$E_G(A_{(1-x)}B_x) = (1-x)E_G(A) + xE_G(B) \quad (6)$$

The exchange of halide ions within the perovskite structure results in the largest change of the lattice parameters and, as a result, the largest change of the band gap. Therefore, blending perovskites with iodide, bromide, and chloride allows tuning the band gap in the broadest range. In this way, the band gap of $CH_3NH_3Pb(I_{1-x}Br_x)_3$ can be altered between 1.6 and 2.33 eV by increasing the fraction of bromide from x = 0 to x = 1 (Figure 11a, b).[70,72,73]

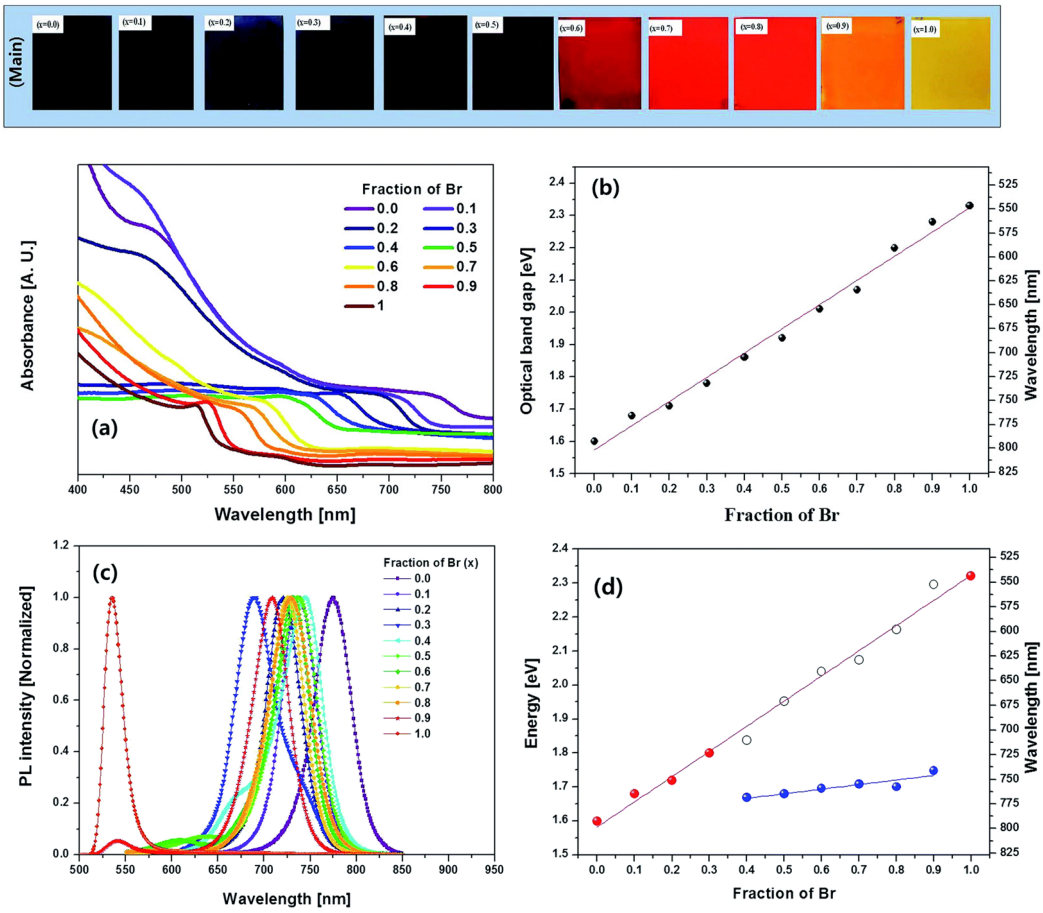

Figure 11. Top: optical photographs of $CH_3NH_3Pb(I_{1-x}Br_x)_3$ films. (a) UV-vis absorption spectra of these samples. (b) Optical bandgap as a function of Br-fraction in

$CH_3NH_3Pb(I_{1-x}Br_x)_3$. (c) Photoluminescence spectra for the same films (normalized at maximum emission peak). (d) PL emission peak energy as a function of Br-fraction in $CH_3NH_3Pb(I_{1-x}Br_x)_3$. Reproduced from Ref.[72] with permission from The Royal Society of Chemistry.

The optical band gap obtained from absorption measurements depended linearly on the fraction of bromide. However, photoluminescence studies revealed an appearance of an additional peak with a lower band gap energy (E_g = 1.65 eV) than the main peak (Figure 11c, d). This peak has been attributed to the formation of a new phase. The composition of the new phase is not yet identified. However, it is conceivable that the new phase consists of an iodine-rich perovskite phase, while the main peak corresponds to a fully mixed perovskite material. Interestingly, the segregation process depends strongly on the illumination of the materials.[74] On the one hand, numerous reports showed that the segregation process is induced by illumination and strongly promoted with the duration of the illumination. On the other hand, the specimens recovered completely after storage in the dark. In fact, the material can be cycled many times between mixed and segregated state by illumination and recovery in the dark.[42,74,75] This reversible segregation upon illumination strongly indicates a photo-induced origin of the effect. Moreover, the intensity of the PL peak corresponding to the iodine-rich phase increases with illumination time. It is possible that the PL spectra are dominated by the emission of the lower energy iodide-rich phase, as photo-generated charge carriers relax from higher to lower state. This results in an enhancement of the PL intensity of the peak corresponding to iodide-rich domains. In addition, the segregation process in $CH_3NH_3Pb(I_{1-x}Br_x)_3$ perovskites is temperature activated. Hoke et al. have demonstrated that the segregation process has the activation energy of 0.27 eV (Figure 12a).[74] This value is in a good agreement with values of the activation energy for halide migration in hybrid perovskites and metal halides.[76–78] Therefore, it is likely that the photo-induced phase segregation is related to ion migration in hybrid perovskites.[79,80]

The study by Bischak et al. suggests that the segregation process is additionally driven by strain in the mixed material.[81] The authors suggested that charged excitations generate a lattice strain in material that is sufficient to induce segregation. Moreover, the study has demonstrated that the segregation process occurs as a formation of iodide-rich domains of about 8 nm (Figure 12b). Figure 12 (b) shows the cathodoluminescence (CL) image of these iodide-rich domains combined with SEM top view image. The domains are marked by yellow colour. Interestingly,

the prolonged illumination leads to an increase of nucleation of the new domains rather than their growth. In addition, the segregation process occurs within seconds.

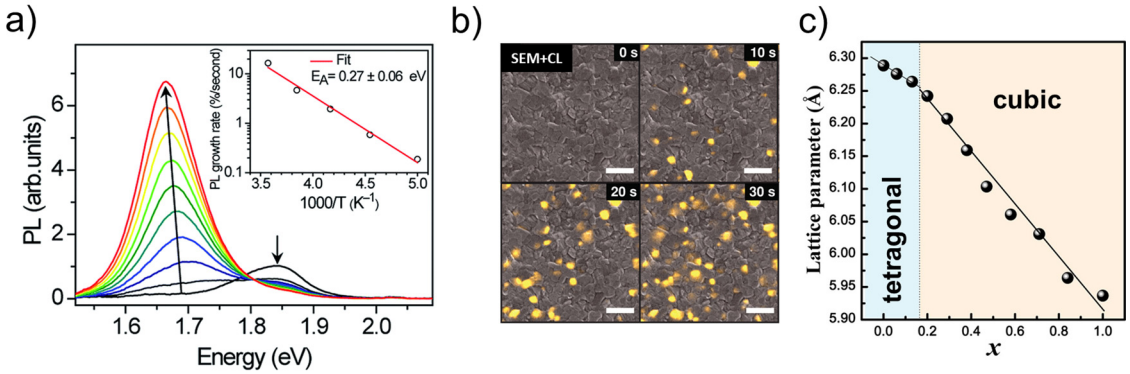

Figure 12. (a) PL spectra of a $CH_3NH_3Pb(Br_{0.4}I_{0.6})_3$ thin film measured over 45 s in 5 s increments under illumination at a wavelength of 457 nm and a power density of 15 $mWcm^{-2}$ (~1/10 sun) at 300 K. Inset shows the temperature dependence of the initial PL growth rate. Adapted from Ref. [74] 2015 - Published by The Royal Society of Chemistry. (b) Cathodoluminescence (CL) image series with 10 s of illumination between each CL image. The scale bars are 2 µm. Reprinted with permission from Ref.[81] Copyright 2017, American Chemical Society. (c) Lattice parameters of pseudocubic or cubic $CH_3NH_3Pb(I_{1-x}Br_x)_3$ as a function of Br composition (x). Reprinted with permission from Ref.[70] Copyright 2013, American Chemical Society.

The process of segregation bears within itself a fundamental limitation of the application of mixed hybrid perovskites as an absorber in solar cells. However, the tendency to segregation depends strongly on the size of the ions in the mixture. For example, the chemical substitution of the A-site cation with formamidinium or cesium leads to a change of the band gap of the iodide-rich phase.[82] Similarly, mixed cation perovskites showed different position of the second PL peak. This effect of other ions might be related to a change of the lattice parameters.

For many materials, the onset of the segregation corresponds to the composition of the material at which the material undergoes a phase transition. For instance, $CH_3NH_3Pb(I_{1-x}Br_x)_3$ begins to segregate under illumination when it contains more than $x > 0.2$ of Br, what corresponds to a band gap of about 1.7 eV. Exactly at this composition, the material crystallizes in cubic phase and no longer in the tetragonal phase (Figure 12c).[70] Formamidinium and cesium-based mixed halide perovskites, on the other hand, showed the onset of segregation at 1.5 and 1.9 eV, respectively.[82,83] Evidently, the change of the lattice parameter induced by the ionic radius of the A-site cation influences the stability of the mixed material during the phase transition. As a result, the addition of the smallest cation, Cs, leads to a reduction of lattice mismatch between iodide- and bromide-based domains. This allows to obtain mixed

perovskites with a band gap of about 1.9 eV.[83] Vast mismatch of lattice parameters of iodide and chloride-based perovskite results in the absence of known mixed iodide/chloride perovskites which strongly supports this conclusion.[84] Nevertheless, the driving force and the mechanism of the phase segregation are yet unknown.

2.4.3. Photostability of hybrid perovskites

Among many different degradation pathways of hybrid perovskites, the understanding of the photo-induced degradation is essential for stable solar cells. On the one hand, absorption of light results in the generation of charge carriers, which then can be extracted and converted into electricity. On the other hand, illumination of the material leads to the phase segregation and, in certain conditions, degradation. The deterioration of perovskite solar cells under constant illumination is vastly reported through the literature.[85,86] Similarly to organic and dye-sensitized solar cells, rapid deterioration of the perovskite-based devices was related to degradation of organic selective layers such as spiro-OMeTAD and PEDOT:PSS or the generation of traps in TiO_2.[87–89] Vast decomposition under illumination was reported for many conductive polymers which are used as a selective layer in perovskite solar cells.[90–93] A drastic improvement of stability was achieved by the substitution of organic transport layers with inorganic ones (NiO_x, ZnO) (Figure 13a).[94] However, several reports showed a reduction of the photovoltaic performance solely due to degradation of the absorber material (Figure 13b).[87,95,96] This effect occurs as a result of the photo-induced generation of defects and can be reversible to certain extent when devices are stored in the dark.[97,98]

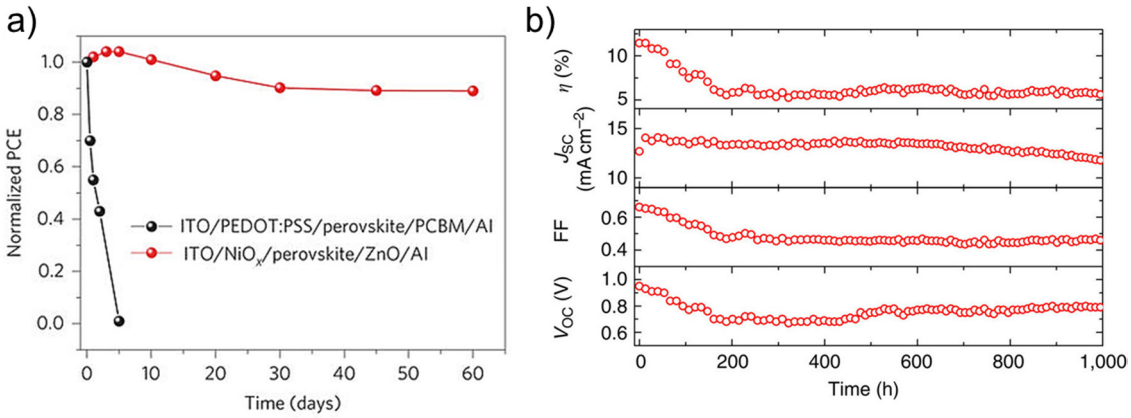

Figure 13. (a) Normalized power conversion efficiency (PCE) of perovskite solar cells following the layer stack ITO/PEDOT:PSS/perovskite/PCBM/Al (black) and ITO/NiO_x/perovskite/ZnO/Al (red) as a function of storage time in ambient environment (30–50% humidity, T = 25 °C). Reprinted by permission from Ref. [94] Copyright 2016, Springer

Nature. (b) Performance of FTO/TiO_2/perovskite-Al_2O_3/spiro-OMeTAD/Au solar cell measured directly during ageing monitored every 15 min under continuous illumination (76.5 mW cm^{-2}) at 40 °C. The device was encapsulated with epoxy resin and a glass coverslip in a nitrogen-filled glove box and no UV cutoff filters are used. Reprinted by permission from Ref.[87] Copyright 2013, Springer Nature.

The study by Zu et al. showed a photo-induced degradation of $CH_3NH_3Pb(I_{(1-x)}Cl_x)_3$ thin films and $CH_3NH_3PbI_3$ single crystals.[99] Using ultraviolet photoelectron spectroscopy (UPS), a reversible shift of the valence band maximum and the work function was observed under the illumination with white light. This shift corresponds to the generation of a surface photovoltage and recovers when stored in the dark. However, when specimens were subjected to a higher photon doses or prolonged illumination, the effect caused by surface photovoltage disappeared. The angle-dependent X-ray photoelectron spectroscopy measurements on the same samples revealed the formation of Pb^0 after prolonged illumination (Figure 14a). In addition, the illuminated materials showed a drastic change in the absorption spectrum. Illuminated thin films no longer showed an absorption or emission in the visible wavelength range.

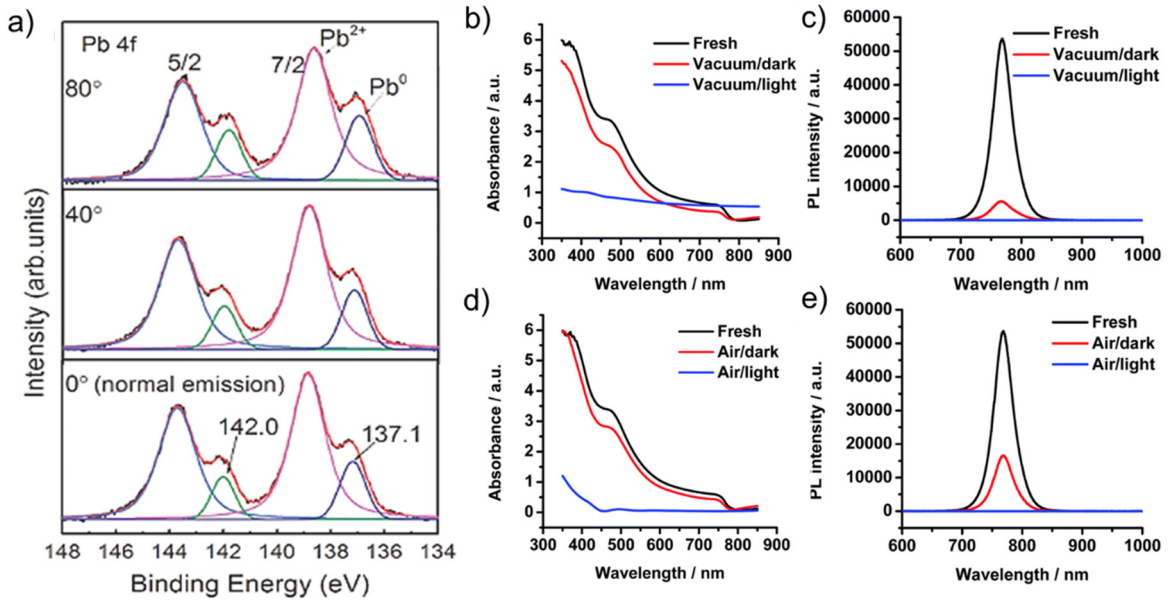

Figure 14. (a) Angle-dependent XPS spectra of the $CH_3NH_3PbI_{3-x}Cl_x$ thin film after multiple on-off illumination cycles (surface photovoltage already quenched). Reproduced with permission from Ref.[99]. Copyright 2017, Wiley. Absorbance spectra of $CH_3NH_3PbI_3$ films degraded for 24 hours in (b) vacuum and (d) air and corresponding steady-state photoluminescence (c, e). Reproduced from Ref. [100] with permission from The Royal Society of Chemistry.

Tang et al. reported a vast decomposition of $CH_3NH_3PbI_3$ under illumination in vacuum and air (Figure 14b-e).[100] The specimens after illumination did not show any absorption or emission in the visible range. Interestingly, the material stored in the dark in both vacuum and air exhibited a drastic reduction of the PL intensity. This behaviour indicates a slow decomposition of the material even in the dark. However, the decomposition rate was accelerated by exposure to white light. In the case of illumination in a vacuum, the specimen was converted to Pb^0, similarly to what reported by Zu.[99] Illumination in air, on the other hand, led to the formation of a variety of oxidation and hydration products. Figure 15 depicts *in-situ* XRD spectra of $CH_3NH_3PbI_3$ in a vacuum (a) in the dark and (b) under white light illumination over time. The formation of PbI_2 was observed after about 10 h in the dark under vacuum conditions (Figure 15a). This observation is indicating a possible out-diffusion of CH_3NH_3I or CH_3NH_2 from a sample under vacuum. In contrast, XRD of the illuminated sample indicates the formation of both lead iodide and metallic lead in the material (Figure 15b). Therefore, it is plausible that the degradation process occurs within two steps: degradation of the material to lead iodide and decomposition of lead iodide to lead.

$$CH_3NH_3PbI_3(s) \rightarrow CH_3NH_2(g) + HI(g) + PbI_2(s)$$

$$PbI_2(s) \rightarrow Pb(s) + I_2(g)$$

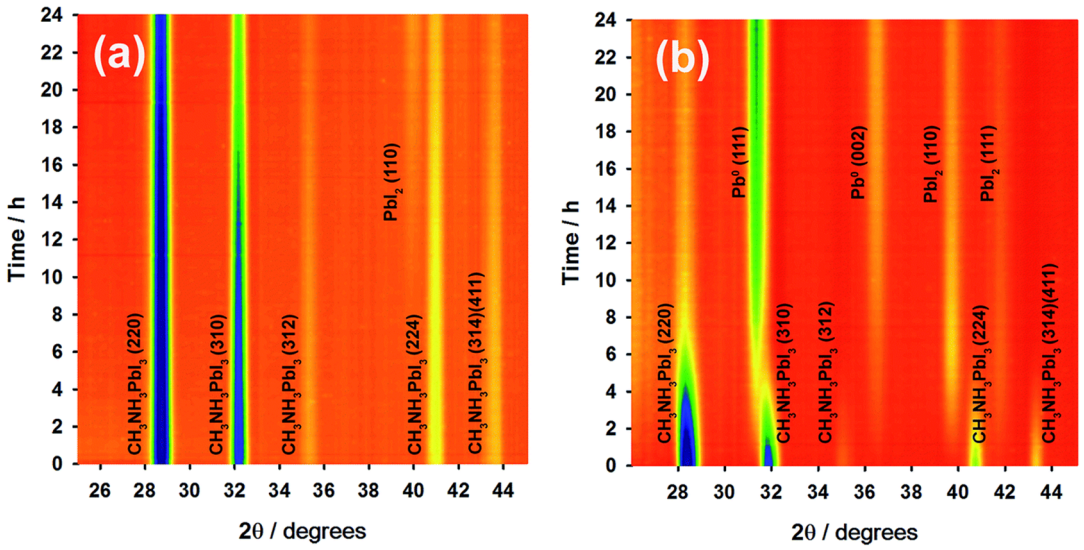

Figure 15. In situ XRD of $CH_3NH_3PbI_3$ films at 350 K under vacuum in the dark (a) and under illumination (b). Reproduced from Ref.[100] with permission from The Royal Society of Chemistry.

A vast number of reports showed an intrinsic problem with the stability of hybrid perovskites under illumination. On the one hand, several reports address the presence of organic components as a prerequisite for photo-induced degradation. On the other hand, the

use of lead iodide in photographic processes indicates a low activation energy for the photo-dissociation of the material.[101,102] In addition, the relative stability of the specimens tested under illumination in a nitrogen atmosphere does not allow to draw a common mechanism of the decomposition process. Therefore, the photo-induced degradation of different hybrid perovskites will be further examined in Chapter 4.2.3 (page 83) and a microscopic model will be drawn in Chapter 5 (page 91).

3. Methods & Experimental techniques

This chapter provides the description of the experimental techniques used within this thesis for characterization of perovskite thin films and devices. The described techniques include X-ray diffraction (XRD), surface photovoltage (SPV) measurements, Fourier-transform infrared (FT-IR) spectroscopy, Current-Voltage (IV) characterization, and External quantum efficiency (EQE) measurements. In addition, the description of the thin film deposition methods and solar cell fabrication procedures is provided in this chapter.

3.1. Experimental techniques

X-ray diffraction

X-ray diffraction is a technique used to determine the atomic structure of a crystal. The technique is based on an interaction of incident X-ray beam with the electronic shell of an atom in a solid. The incoming beam interacts with atoms primary through the elastic scattering of the electrons. When X-ray hits an electron, the electron produces secondary spherical waves. This expanding spherical waves of neighbouring scattering centers interfere with each other leading to constructive and destructive interference. Destructive interference results in canceling out of these waves. However, the waves are added constructively in certain conditions leading to the appearance of the diffraction pattern. The position of the atoms in a three-dimensional lattice can be determined by measuring the intensities dependent on the angle of the diffracted beams. The conditions for the appearance of the diffraction is determined according to the Bragg's law:[103]

$$2d \cdot sin\theta = n\lambda \tag{7}$$

where d is the spacing between neighbouring planes, θ is the incident angle, n is an integer, and λ is the wavelength of the beam. According to Bragg's law, the constructive and destructive interferences can be presented as shown in Figure 16.

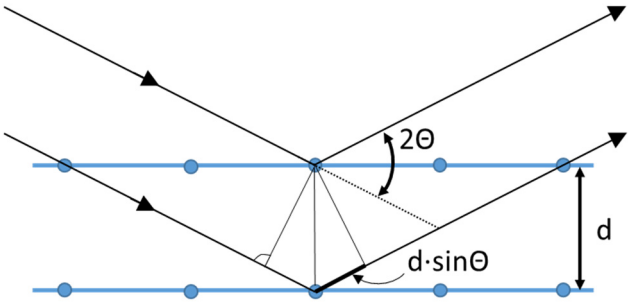

Figure 16. Schematic representation of Bragg's law, where neighbouring lattice planes are irradiated with X-ray beam incident at 2θ angle.

According to Figure 16, the waves will be synchronized and added constructively if electrons arranged symmetrically in the plane with spacing d, only in directions where their path-length difference d·sin θ equals an integer multiple of the wavelength, λ. In case, if the length of the phase shift is not an integer multiple of λ, the shift in the wave trains results in the destructive interference. Since the planes corresponding to the translational symmetry of a crystal, the reflections at certain angles can be assigned to values of the translational vectors.

In addition, Bragg's law can be used for determination of the lattice parameters of a particular crystal structure.[104] For example:

$$cubic\ structure \qquad \frac{1}{d^2} = \frac{h^2+k^2+l^2}{a^2} \tag{8}$$

$$tetragonal\ structure \qquad \frac{1}{d^2} = \frac{h^2+k^2}{a^2} + \frac{l^2}{c^2} \tag{9}$$

Moreover, X-ray diffraction can be used for calculation of crystalline size and strain. Ideally, the reflections should appear as single lines at defined *2*θ values. However, the periodicity, defects, lattice strain, and preferred orientation, as well as instrumental effects could influence the shape of the reflections. The Scherrer equation allows to estimate the size of the crystalline particles which is related to the line broadening and varies with Bragg angle, θ:

$$L = \frac{K\lambda}{\beta cos\theta} \tag{10}$$

where L is the mean size of the crystalline domain, K is the Scherrer constant or shape factor, often assumed to be equal to 0.9, λ is the X-ray wavelength, θ is the Bragg angle, and β is the line broadening at half the maximum intensity.[105]

The modified Scherrer equation is named after Williamson and Hall.[106] The method is based on the assumption that the strain in the material causes a line broadening in X-ray diffraction measurements. Therefore, the equation consists of two parts: the line broadening due to strain (β_e) and the line broadening due to size (β_L):

$$\beta_{tot} = \beta_e + \beta_L = C\varepsilon\, tan\,\theta + \left(\frac{K\lambda}{L\, cos\theta}\right) \tag{11}$$

where ε is the value of strain and C is constant, often C ≈ 4 or 5. Using this equation, the "size-strain plot" can be obtained and values of corresponding crystalline size and strain can be determined from the y-intercept and slope of the linear fit, respectively.

Surface photovoltage (SPV)

Surface photovoltage is a contactless technique which allows to determine the minority carrier diffusion length.[107] The technique is based on the measurement of the surface potential of a semiconductor while generating electron-hole pairs with the light source. The surface potential occurs as a result of a bend-bending induced by the surface charge in a semiconductor in the dark. However, when the surface of the semiconductor is illuminated, the change of the surface potential is a function of the excess minority carrier density injected into the space charge region. The minority carrier density is, in turn, depends on the incident light intensity, the optical absorption coefficient, and the diffusion length.[108] Therefore, the SPV signal can be described according to the equation:

$$SPV = f(\Delta n) = f\left(\frac{QE(\lambda)\cdot I(\lambda)\cdot(1-R(\lambda))}{D/L+s(\Delta n|_{x=0})}\cdot\frac{\alpha(\lambda)\cdot L}{1+\alpha(\lambda)\cdot L}\right) \quad (12)$$

where QE is quantum efficiency, I is the intensity of the incident light, R is optical reflection coefficient, λ – wavelength, D – diffusion coefficient, L – diffusion length, α – absorption coefficient, and s – surface recombination velocity at the illuminated surface. If we assume that QE and R are constant over the α region of interest, the procedure after Goodman can be applied and the SPV equation can be rewritten as:[108]

$$I\cdot\big(\alpha(\lambda)\big) = const\cdot(\alpha(\lambda)^{-1}+L) \quad (13)$$

In the approach after Goodman, the SPV signal is kept constant in order to keep constant surface recombination. The light intensity required for keeping the SPV signal constant is in direct correlation with wavelength and intensity of the SPV signal. The corresponding light intensity is measured as a function of the wavelength and plotted as a function of the related absorption length, also called Goodman plot (Figure 17). The negative value of the diffusion length is found from the intersection point at zero intensity.

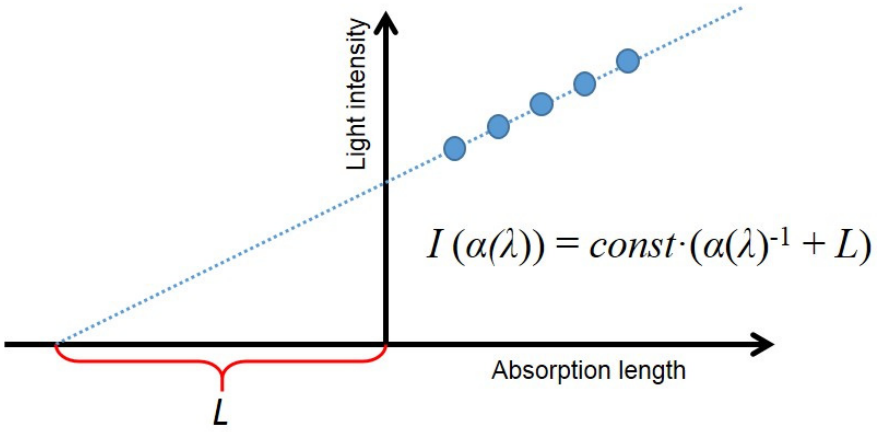

Figure 17. Schematic representation of the Goodman plot.

Fourier-transform infrared spectroscopy (FT-IR)

Fourier-transform infrared (FT-IR) spectroscopy is a technique used for analysis of the structure and composition of the materials in the solid, liquid, or gas phase.[109] FT-IR method is based on the fundamental interaction of infrared light with bound atoms of a compound. The absorption of IR radiation by the bound atoms results in the appearance of a vibration. The requirements for such a vibration to be active in the IR range is a change in the dipole moment of a bond during this vibration. The vibration can be categorized by the direction of the movement into stretching (changing bond length) and deformation vibrations (changing bond angles) and by the symmetry of the vibration into symmetric and asymmetric vibrations.

The vibrations often occur in a specific region, typical for certain structures. Therefore, the concept of characteristic vibrations and fingerprint region can be used for a qualitative analysis and identification of polyatomic molecules. The vibrational frequency can be estimated using a simple model of harmonic oscillators.

In contrast to dispersive infrared spectrometers, the FTIR spectrometer is based on a broadband light source coupled with Michelson interferometer (Figure 18).

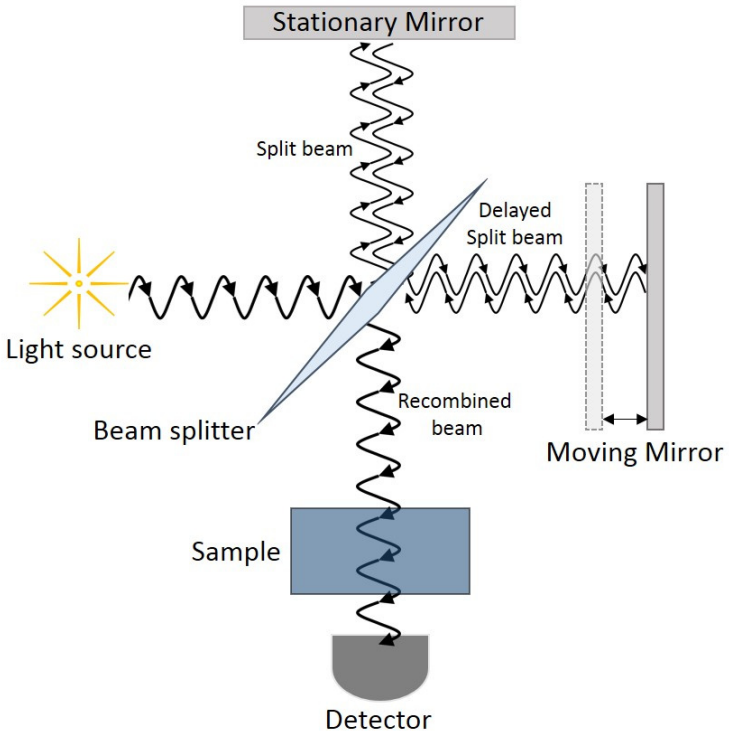

Figure 18. Schematic diagram of Michelson interferometer as a part of FTIR setup.

The broadband IR beam is divided into two beams by a beam splitter. Then, one beam is reflected by the fixed or stationary mirror and the other beam is reflected off of the moving mirror. Both reflected beams are recombined again at the beam splitter and travel through a sample. The recombined beam consists of two beams: the original beam and the delayed or retarded beam. The difference in the optical pathway of two beams is known as the optical path difference (OPD) or retardation. The absorption of IR light is recorded for various OPD values from 0 to maximum length, which allows to obtain an interferogram. Using the Fourier-transform algorithm leads to the calculation of the light absorption as a function of wavenumber. As a result, FT-IR allows to obtain the whole spectral dependence at once and with high sensitivity. Moreover, the maximum spectral resolution of the measurement is inversely proportional to the maximum value of OPD and, hence can be easily adjusted.

Current-Voltage (IV) characteristics

The power conversion efficiency of a solar cell is a measurement of capability of a device to generate electrical power from light. The key characteristics of a device can be determined from its Current-Voltage dependence (IV) under standard testing conditions. At standard test conditions, a device is being measured under simulated illumination equal to 1 sun or air mass 1.5 global (AM 1.5 G) corresponding to 100 mW/cm^2. In the dark, the IV curve can be described by the diode equation.[110] Under illumination, the IV curve is a combination of the diode equation in the dark with an addition of light-generated charge carriers:

$$J = J_0 \left[exp\left(\frac{qV}{nkT}\right) - 1 \right] + I_L \qquad (14)$$

where J is the net current flowing through the diode, J_0 - dark saturation current, q - electron charge, V - applied voltage across the terminals of the diode, k - Boltzmann's constant, T - absolute temperature in K, and I_L is light-generated current. A typical Current-Voltage curve (IV curve) under illumination is shown in Figure 19.

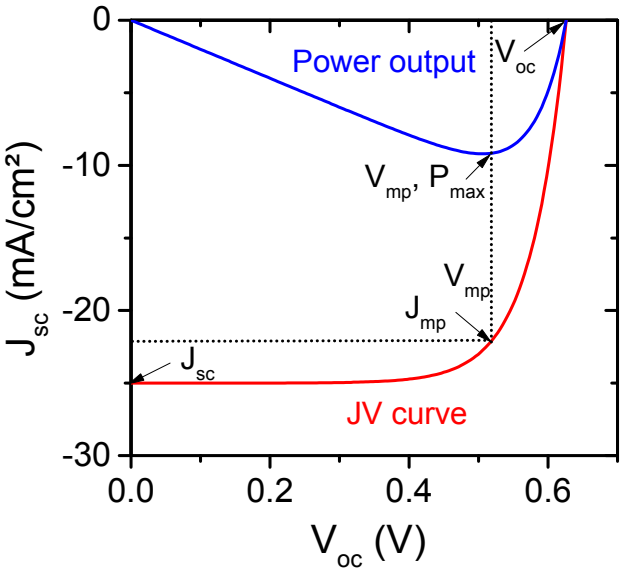

Figure 19. A typical Current-Voltage characteristics of a solar cell (IV curve) under illumination (red curve) and the power output generated by the same solar cell (blue).

The short circuit current (J_{sc}), open circuit voltage (V_{oc}), fill factor (FF), power conversion efficiency (η), and maximum power output (P_{max}) can be determined from this dependence. The values of the open circuit voltage can be determined from an interception point of the IV curve with the x-axis. The value of short circuit is taken from the interception of the curve with

the y-axis. The value of fill factor describes the "squareness" of the curve. It strongly depends on the series and the shunt resistance, as well as diode losses. Experimentally it can be determined from the ratio of products of the maximum power point current (J_{mp}) and voltage (V_{mp}) and products of J_{sc} and V_{oc}:

$$FF = \frac{J_{mp}V_{mp}}{J_{sc}V_{oc}} \tag{15}$$

The power conversion efficiency is equal to the ratio of the power output produced by the solar cell and the incident radiation power of the sun. Then, the efficiency can be calculated according to:

$$\eta = \frac{V_{OC}J_{SC}FF}{P_{in}} \tag{16}$$

where, P_{in} is the input power.

In principle, a device can be operated over a broad range of voltages and currents. Figure 19 shows the power generated by the solar cell power as a function of applied voltage and follows the equation:

$$P_{max} = J_{sc}V_{oc}FF \tag{17}$$

The maximum power can be measured separately by the maximum power point (MPP) tracking. This technique allows to find the stabilized maximum power point at operating conditions and measure it as a function of time.

External Quantum efficiency (EQE)

One of the most important characterization methods of a photovoltaic device is quantum efficiency (QE). The quantum efficiency is the ratio of the incident photons to the number of charge carriers to which these photons are converted. Usually, the QE is measured with monochromatic light of different wavelengths, therefore the measurement results in a spectral dependence. The QE can be considered regarding the optical properties of the sample as external or internal QE. The external quantum efficiency (*EQE*) includes optical losses such as transmission and reflection. The internal quantum efficiency (*IQE*), on the other hand, only considers the photons, which are not reflected or transmitted, but absorbed in the device and can be converted into charge carriers:

$$EQE = \frac{electrons}{photons} \tag{18}$$

$$IQE = \frac{EQE}{1-R-T} \tag{19}$$

where R is reflection and T is the transmission.

Ideally, the QE curves should be a rectangular shape, where a QE of 100 % indicates that all photons shined on the device were converted to charge carriers across the entire absorption spectrum of the absorber layer. However, optical and electrical losses reduce the values of QE. Figure 20 shows a typical EQE curve of a solar cell.

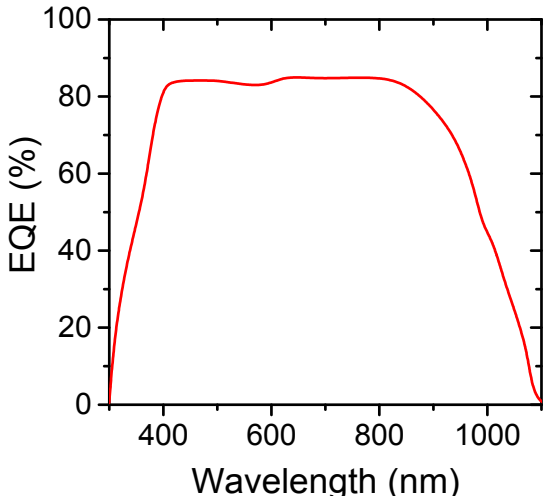

Figure 20 External quantum efficiency of a solar cell.

Often, external quantum efficiency can be improved by reducing effects of recombination of the charge carriers, increasing the diffusion length of charge carriers and by applying light-trapping techniques.

3.2. Sample preparation

Preparation of solutions

ABX_3 perovskite precursor solutions were prepared using equimolar amount of AX and BX_2. The components were combined together and dissolved in appropriate solvent. For the study of the properties of solutions, pure dimethyl sulfoxide (DMSO), dimethylformamide (DMF), γ-butyrolactone (GBL), and N-Methyl-2-pyrrolidone (NMP) were used. The solution of pristine lead iodide was prepared by dissolving lead iodide in a solvent of choice. Then, solutions were stirred and heated at 60 °C for 12 hours.

This film preparation

Thin films of perovskite were deposited on top of a substrate by spin coating procedure. First, substrates were cleaned in ultrasonic bath with deionized water/surfactant, deionized water, acetone, and isopropanol for 15 min in each medium. Then, substrates were dried in the nitrogen flow and cleaned in ozone plasma for 15 min. For the preparation of methylammonium (MA)-based perovskites, the one-step spin-coating procedure was chosen (Figure 21). 70μL of the solution containing 1 mol of CH_3NH_3I and PbI_2 in 1 to 1 ratio in a mixture of γ - butyrolactone (GBL) and dimethyl sulfoxide (DMSO) (7:3) were spread on top of the cleaned substrate.[111] The spin coating procedure consists of two acceleration steps: 1000 rpm for 30 s and 5000 rpm for 10 s. The first step is dedicated to even the distribution of the solution on a surface of the substrate. The second step is dedicated to remove the excess of the solution towards desirable film thickness. During the second step, 150 μL of toluene were dispersed on top of the spinning film. Here, toluene acts as an antisolvent. The antisolvent is used for an acceleration of the precipitation of the perovskite phase due to a reduced solubility of the components in the antisolvent. Similarly, chlorobenzene and ethyl acetate can be used as an antisolvent. After spin-coating, a liquid film of perovskite is formed.

Then, this film is placed on top of a heating plate at 100 °C for 10 min to remove solvent residuals (Figure 21). Finally, the films were cooled down to room temperature and can be used for further processing. All steps of the perovskite deposition and annealing were performed in a nitrogen-filled glove-box.

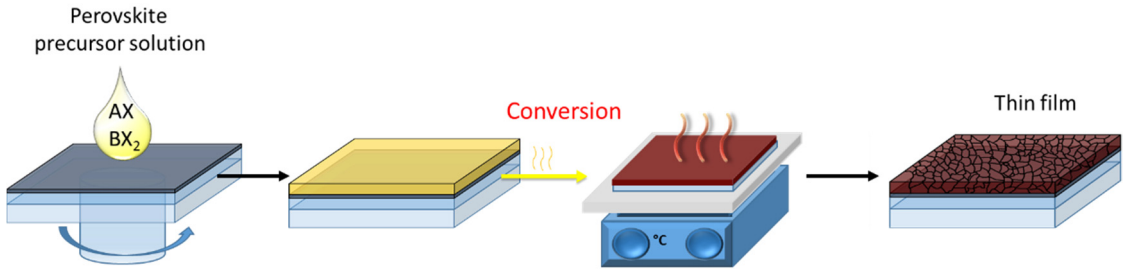

Figure 21. Schematic representation of the one-step spin coating procedure.

Cesium lead iodide thin films were prepared by the one-step spin-coating of 1 molar solution of cesium iodide and lead iodide in one to one ratio in DMSO as described above. The thin films containing Cs-based perovskite were annealed at 300 °C. Bromide ions in $CsPb(I_{1-x}Br_x)_3$ were introduced into the film by adjusting the content of $CsPbBr_3$ in the mixture of $CsPbBr_3$ and $CsPbI_3$.

In addition, thin films of $CsPb(I_{1-x}Br_x)_3$ were prepared by the two-step spin-coating process (Figure 22). First, the film of lead halide was spin-coated on top of a substrate from 1 molar solution of PbI_2 in DMF. Then, this liquid film was exposed to 70 µl of CsI and CsBr mixture in methanol. After intercalation of cesium halide into the lead halide, the film was rinsed with pure methanol to remove excess of cesium halide. Then these thin films were annealed at 300 °C to convert the material to the perovskite phase.

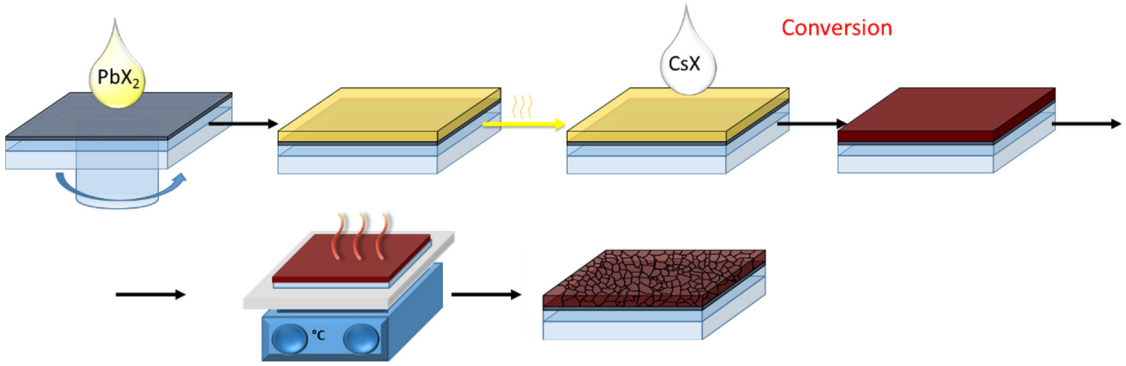

Figure 22. Schematic representation of the two-step spin-coating procedure used for deposition of $CsPb(I_{1-x}Br_x)_3$.

Device preparation

The one-step spin-coating procedure was used for the deposition of the perovskite layers. For this work, both inverted and regular structures were used. The more robust TiO_2-based regular structure was used for the study of the influence of the temperature on the device performance (Chapter 4.2.1). The solar cells with the regular architecture consisted of FTO/TiO_2/perovskite/spiro-OMeTAD/Au (Figure 23a). First, SnO2:F –coated glass (FTO) was cleaned with detergent/de-ionized water, acetone and isopropanol. On top of SnO_2:F glass a 60 nm thick compact TiO_2 layer was deposited via spin-coating from a sol-gel solution and calcined at 500 °C for 1 hour.[58] Next, a 300 – 400 nm thick layer of perovskite was deposited as described above. Then, the samples were post-annealed at different T_{set}. After post-annealing, the samples were left to cool down to room temperature. Then, the hole conductor - 2,2',7,7'-tetrakis[N,N-di(4-methoxyphenyl)amino]-9,9'-spirobifluorene (spiro-OMeTAD) was spin-coated at 2000 rpm on top of the perovskite layers from a precursor solution. The solution contained 80 mg of spiro-OMeTAD in 1 mL of chlorobenzene, 46.4 µL of a bis(trifluoromethane) sulfonimide lithium salt (LiTFSI) stock solution (170 mg/mL in acetonitrile), and 8.5 µL of 4-tert-butylpyridine. Finally, 80 nm thick Au contacts were deposited by thermal evaporation through a shadow mask. The active area of the devices amounted to 0.16 cm^2.

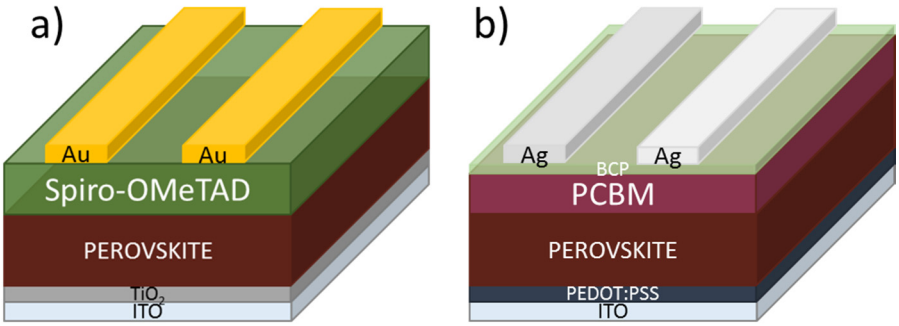

Figure 23. Schematic representation of a solar cell structure with (a) regular and (b) inverted architecture.

Solar cells based on $CH_3NH_3PbI_3$/EDDI blends were prepared in the inverted architecture – ITO/PEDOT:PSS/perovskite/PCBM/BCP/Ag (Figure 23b). First, Indium tin oxide (ITO)-coated glass substrates were cleaned with detergent/de-ionized water, acetone, isopropanol, and ozone plasma. Then, water-based solution of poly(3,4-ethylenedioxythiophene) polystyrene sulfonate (PEDOT:PSS) was spin-coated at 3000 rpm for 30 s on top of ITO substrates and subsequently annealed at 150 °C for 30 min. After annealing, the samples were

transferred to the nitrogen filled glovebox, where the deposition of the perovskite layers was conducted as described above. The electron selective contact, [6,6]-phenyl-C61-butyric acid methyl ester (PCBM), was spin-coated on top of perovskite layers at 2500 rpm for 60 s and annealed at 100 °C for 10 min. Next, a thin layer of bathocuproine (BCP) was spin-coated on top of PCBM at 4000 rpm for 45 s and subsequently annealed at 70 °C for 15 min. Finally, 100 nm of Ag contacts were thermally evaporated using a shadow mask. The active area of the device amounted to 0.16 cm^2.

3.3. Sample characterization

Photoluminescence (PL)

Photoluminescence spectra of hybrid perovskites were measured in air. Perovskite layers were deposited on glass substrate. The spectra were excited with a pulsed laser. The excitation wavelengths of 365, 415, and 500 nm were used with a pulse width of 0.5 ns, pulse energy of 10-20 nJ, and 10 Hz repetition rate. The time-resolved photoluminescence spectra were excited with 500 nm laser and measured at the peak maximum.

Fourier-transform infrared spectroscopy (FT-IR)

Fourier-transform infrared spectra were measured on thin films of perovskite deposited on crystalline Si wedge. The thin films were deposited as described above. For room temperature measurements, samples were mounted on the sample holder in the environmental chamber of FT-IR spectrometer. The chamber was then evacuated up to the basic pressure of $p = 3\times10^{-5}$ mbar and reference measurement of an as-prepared sample was conducted. Then the sample was illuminated with blue or UV light emitting diodes (LED) with a photon energy of $h\nu$ = 2.72 eV and photon flux of $F \approx 3 \times 10^{17}$ s^{-1} cm^{-2} and $h\nu = 3.4$ eV, $F \approx 5 \times 10^{17}$ s^{-1} cm^{-2}, respectively. The FT-IR spectra of illuminated samples were recorded after the noted time of illumination was reached. All spectra were normalized to the spectrum of the corresponding Si substrate. A typical FT-IR spectrum of $CH_3NH_3PbI_3$ at room temperature is shown in Figure 24 (a).

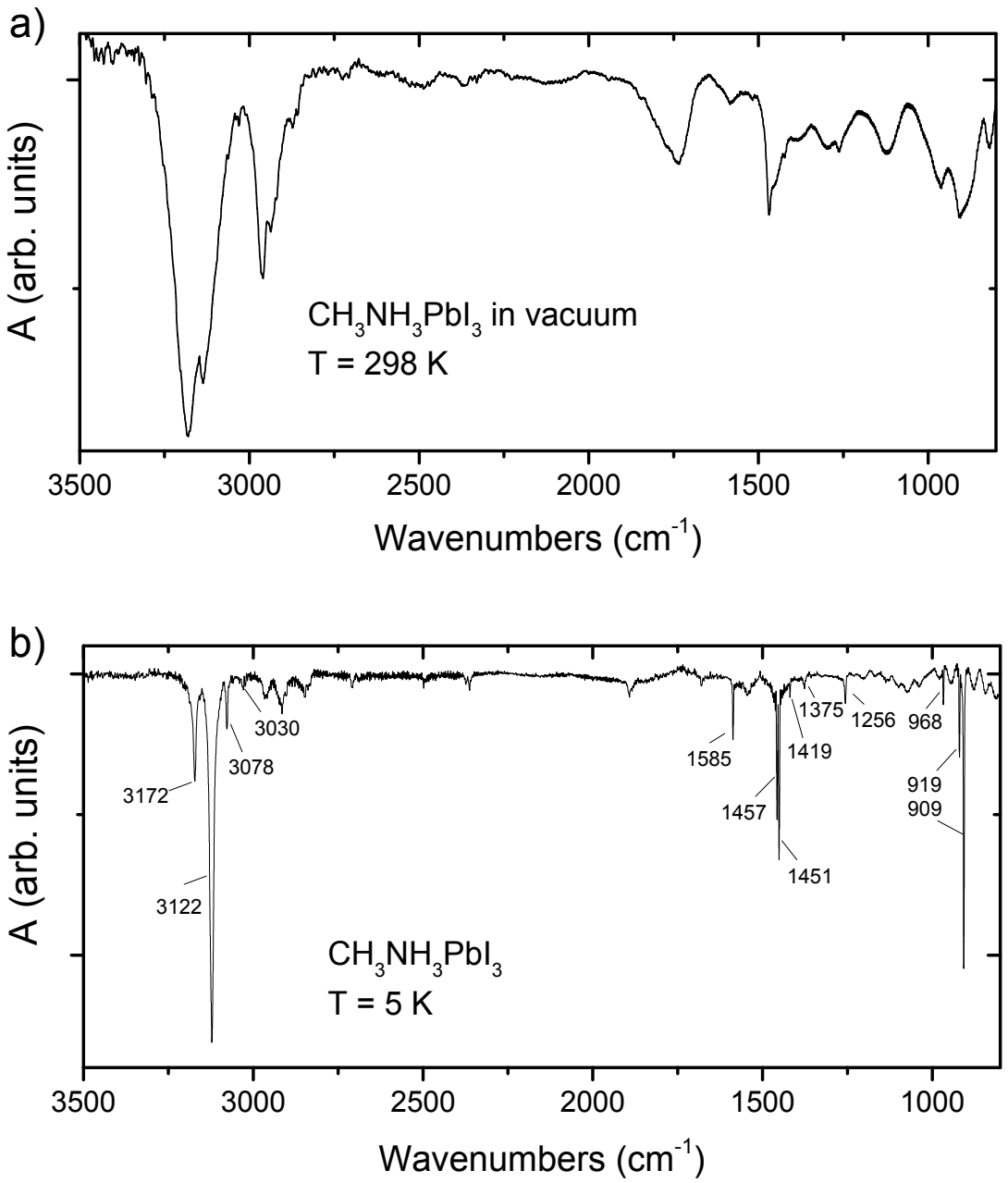

Figure 24. FT-IR spectrum of $CH_3NH_3PbI_3$ in vacuum at 298 K (a) and 5 K (b).

For the FT-IR measurements at low temperatures, a sample was mounted on a cryostat sample holder and placed into a continuous-flow cryostat chamber cooled with liquid helium. The reference measurement was recorded after noted temperature was reached. Then, the samples were kept at the working temperature and illuminated with blue LED, $h\nu = 2.72$ eV and photon flux of $F \approx 3 \times 10^{17}$ s^{-1} cm^{-2}. Similarly, the FT-IR spectra of illuminated samples were recorded after the noted time of illumination was reached. A typical FT-IR spectrum of

$CH_3NH_3PbI_3$ at 5 K is presented in Figure 24 (b). The peaks were assigned in Table 1 according to literature.[112]

Table 1. Position of the peaks of $CH_3NH_3PbI_3$ at 5 K and estimated peak assignment.[112]

peak	5 K	
	Position (cm^{-1})	Peak assignment
1	3172	ν_{as} (NH_3^+)
2	3122	ν_s (NH_3^+)
3	3078	ν_{as} (CH_3, NH_3^+)
4	3030	ν_s (CH_3)
5	1585	δ_s (NH_3^+)
6	1457	δ_s (NH_3^+)
7	1451	δ_{as} (CH_3)
8	1419	δ_s (CH_3)
9	1375	δ_s (CH_3)
10	1256	ρ ($CH_3NH_3^+$)
11	968	ν(C-N)
12	919	ρ ($CH_3NH_3^+$)
13	909	ρ ($CH_3NH_3^+$)

SEM

Morphology of hybrid perovskites was analyzed by scanning electron microscopy (SEM). The grain diameter was obtained by processing of the top view SEM micrographs with ImageJ software.

XRD

X-ray diffractograms were recorded by means of the Panalytical X'Pert Pro Multipurpose Diffractometer (MPD) in Bragg-Brentano geometry. Cu*K*α was used as a source of radiation with current of 40 mA and tension of 40 kV. The PIXcel detector was used for the detection of a signal with 255 channels with 0.0131° resolution.

SPV

The surface photovoltage spectra were measured in the fixed capacitor arrangement. The surface photovoltage was generated by the illumination of the sample through the reference electrode with a halogen lamp. The SPV signals were detected with a high impedance buffer and measured with a double phase lock-in amplifier (EG&G 7260). A part of the modulated light was coupled out with a beam splitter and directed to a detector with a silicon photodiode. The intensity of the modulated light was measured with a second lock-in amplifier (EG&G 7260). The setup used for the SPV measurement is depicted in Figure 25.

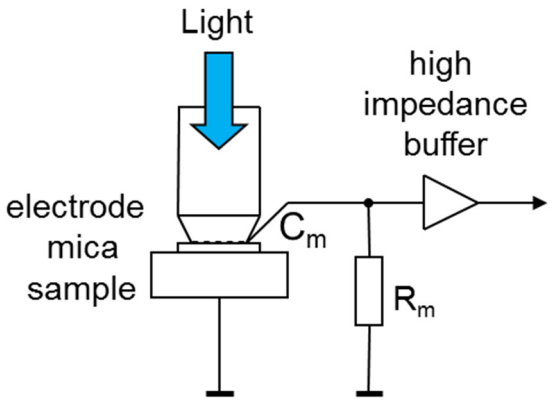

Figure 25. Schematic representation of experimental setup used for SPV measurements after Goodman.

For measurements after Goodman, the analogue output of the in-phase signal was connected to the input of a power supply with an integrated feedback unit (Elektronik Manufaktur Mahlsdorf) at which the desired SPV signal was set. The in-phase SPV signal was kept constant

by adjusting the light intensity of the halogen lamp. Then, the light intensity was plotted as a function of the absorption length. The value of the diffusion length (L) was obtained at the intersection point of the linear function. The analysis was performed over a wide range of constant SPV signals.

Resistivity measurements

For the resistivity measurements, perovskite layers were deposited on top of a glass substrate with Au contacts. The voltage was applied between two neighbouring contacts with a power supply. The generated current was measured by means of a micro-ammeter (Figure 26).

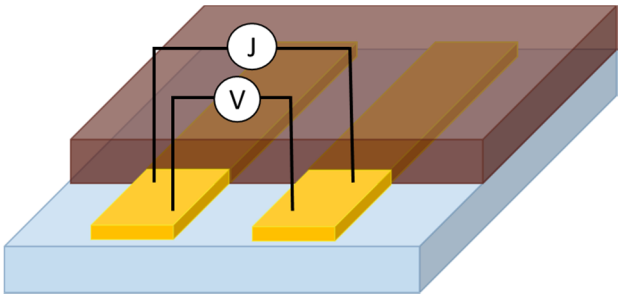

Figure 26. Schematic representation of resistivity measurement.

The values of the resistivity (ρ) were calculated according to the equation:

$$R = \frac{V}{I} \tag{20}$$

$$\rho = R \cdot \frac{A}{L} \tag{21}$$

where R is resistance in Ω, V is applied voltage in V, I is measured current in A, A is a cross-sectional area in cm^2, and L is a length of the channel between contacts in cm.

JV characterization

The current-voltage characterization was performed in air under AM1.5g illumination generated by "Steuernagel Lichtechnik" solar simulator. The solar simulator was adjusted to 100 mW/cm^2 by calibrated silicon solar cell (Fraunhofer ISE). The delay-time was set to 60 s and the acquisition time to 40 s. The current-voltage dependence was recorded in forward and reverse directions of the scan. The MPP tracking was performed over course of 60 s. Typical JV curves of the perovskite solar cell with regular (a) and inverted (b) structures and their corresponding MPP are shown in Figure 27 and Figure 28.

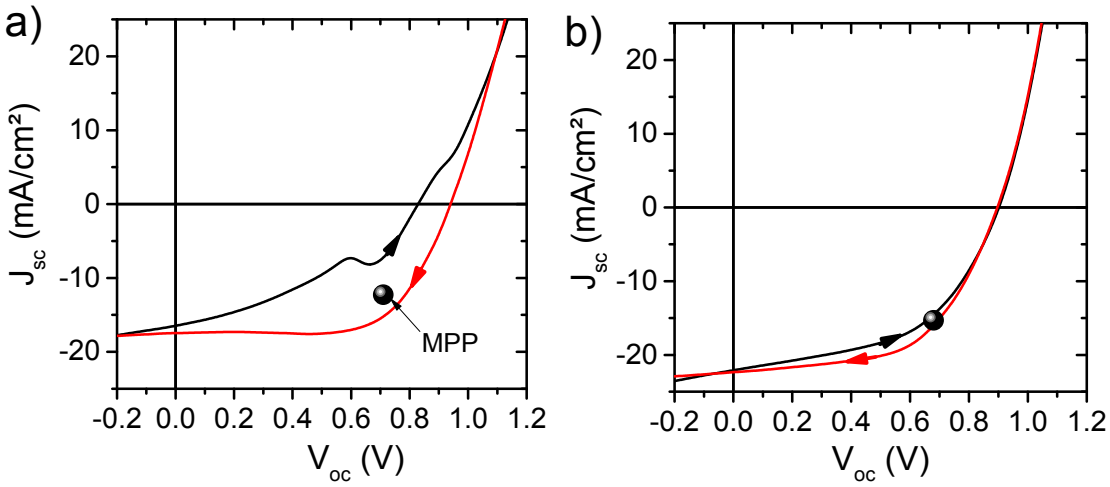

Figure 27. Current-voltage characteristics of a typical perovskite solar cell with (a) regular structure (n-i-p) and (b) inverted structure (p-i-n). The direction of the scan is indicated by arrows. Black circle indicates maximum power point stabilized after 60 s of MPP tracking.

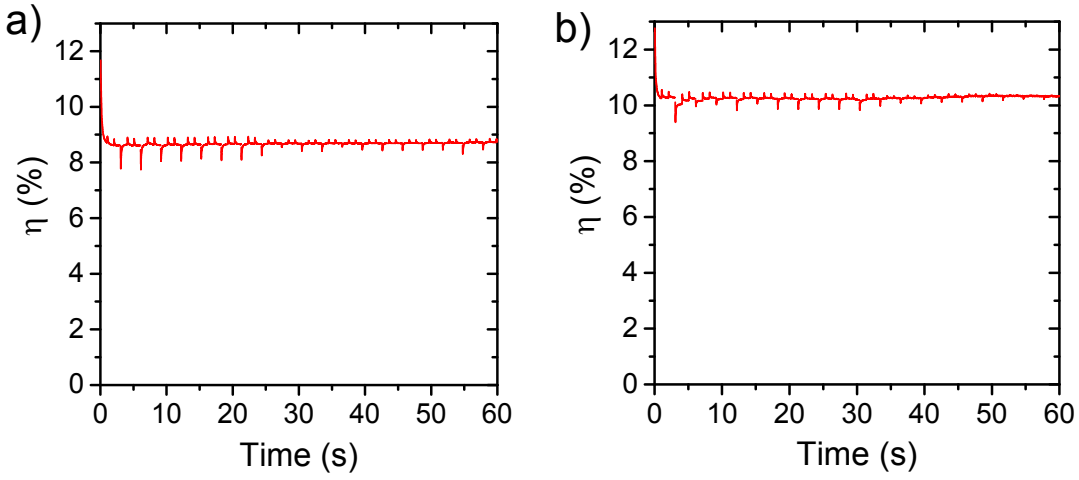

Figure 28. The maximum power point tracking of the corresponding devices with regular (a) and inverted structure (b) from Figure 27.

EQE

The external quantum efficiency (EQE) was measured in a nitrogen atmosphere using an Oriel Instruments QEPVSI-b system with a Xenon arc lamp (Newport 300 W, 66902) chopped at 35.5 Hz. The measurements were performed in a wavelength range from 300 to 850 nm with 10 nm steps. The illumination beam size on the sample amounted to 2.5 × 2.5 mm^2. The EQE measurements were performed without background illumination or applied bias voltage. Typical EQE spectrum of a perovskite solar cell is shown in Figure 29.

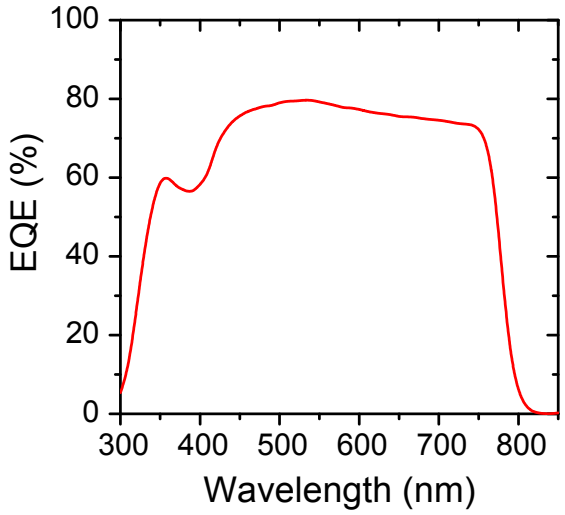

Figure 29. EQE measurement of a perovskite solar cell.

4. Results

This chapter presents the results obtain within this thesis. The first part is dedicated to a study of chemical interactions occurring between precursors and precursors and solvent. The aim of this study is to identify the processes which influence the formation of perovskites and to understand the correlation between these processes and properties of the resulting material. The second part of this work focuses on different instability mechanisms related to temperature, composition, and light. Within this part, the influence of temperature on the optical and electronic properties of $CH_3NH_3PbI_3$ thin films was revealed. Then, the compositional stability of hybrid perovskite blends was studied. In particular, the stability of mixed halide $CsPb(I_{1-x}Br_x)_3$ perovskites and blends of $CH_3NH_3PbI_3$ and $CsPbI_3$ with ethylenediammonium diiodide was investigated. In the last part of this chapter, the photostability of $CH_3NH_3PbI_3$, $CH(NH_2)_2PbI_3$ was revised.

4.1. Formation of hybrid perovskites: Solvation and complexation of PbI_2

First, an influence of solvent on optical properties of $CH_3NH_3PbI_3$ was investigated. The photoluminescence spectra of methylammonium lead iodide ($CH_3NH_3PbI_3$) thin films are presented in Figure 30. The films were prepared from N-Methyl-2-pyrrolidone (NMP), dimethyl sulfoxide (DMSO), and dimethylformamide (DMF). Interestingly, all specimens exhibited a slightly different position of the maximum of the normalized photoluminescence intensity (I_{PL}).

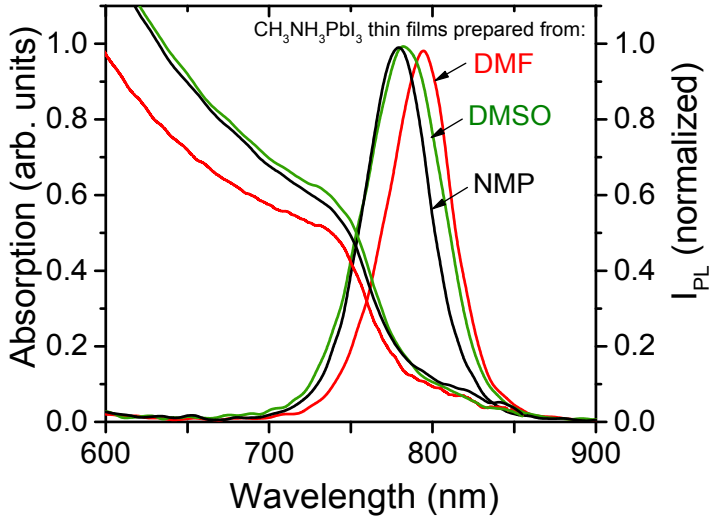

Figure 30. Photoluminescence and absorption spectra of perovskite thin films fabricated from dimethylformamide (DMF), dimethyl sulfoxide (DMSO), and N-methyl-2-pyrrolidone (NMP) as solvents in the precursor solutions.

Specifically, the thin film deposited from DMF solution had the maximum of the PL peak at 794.8 nm, which corresponds to an optical band-gap of 1.56 eV. Using DMSO and NMP as solvents for the precursor solutions led to a blue shift of the PL peak maximum to 782.4 nm (1.58 eV) and 779.1 nm (1.59 eV), respectively. A similar trend can be observed in the absorption spectra of these layers. Different absorption onsets for layers fabricated from different solvents this support the observation. Moreover, this indicates that the choice of solvent influences strongly the material properties of the fabricated layers.

To elaborate on the influence of the solvent on the material properties, PL- and absorption spectra of the $CH_3NH_3PbI_3$ precursor solution were measured using DMF as the solvent (Figure 31a). The solution exhibited an absorption onset at 465 nm (2.66 eV), which is in a good agreement with values reported in literature.[113] However, the PL spectrum of the same solution

showed a strong red-shifted PL peak with a maximum at 764.9 nm (1.62 eV). This behaviour is unexpected and might occur due to a precipitation of perovskite crystallites on the walls of the cuvette. To exclude the influence of $CH_3NH_3PbI_3$ particles, a solution of pure lead iodide (PbI_2) was measured under the same conditions. The associated spectra are depicted in Figure 31(b) for a 0.1 M PbI_2 solution in DMF. Additionally, the spectra of PbI_2 powder are plotted (dotted lines). The solution of lead iodide exhibited a blue-shifted absorption onset at about 445 nm in comparison to 465 nm of the $CH_3NH_3PbI_3$ solution. Both PbI_2 and perovskite solutions, exhibited shifted absorption onsets to smaller wavelength values compared to PbI_2 powder. The PbI_2 powder showed an absorption onset at 505 nm and a PL peak maximum at 506 nm, which corresponds to a band gap of 2.45 eV.[114] In contrast to the powder specimen, the PL spectrum of lead iodide in solution has its peak maximum close to the value of $CH_3NH_3PbI_3$ in solution at 760.5 nm (1.63 eV). Thus, it is conceivable that the energetic position of the emission of $CH_3NH_3PbI_3$ in a solution is due to the formation of a complex structure related to PbI_2.

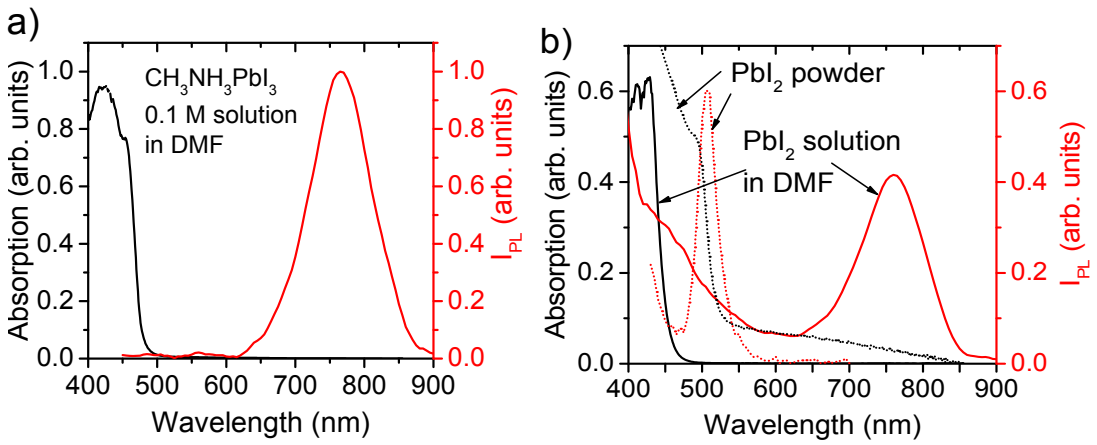

Figure 31. (a) Photoluminescence (red) and absorption (black) spectra of the precursor solution of $CH_3NH_3PbI_3$ in DMF. (b) Photoluminescence (red) and absorption spectra (black) of PbI_2 powder and PbI_2 solved in DMF.

As usual for semiconductors, the PbI_2 powder showed the PL maximum at the onset of the absorption spectrum. This is not the case for the solution of PbI_2 in DMF, what points to the formation of Pb-related complexes with the solvent. It is feasible, that the nature of the observed complex structures of PbI_2 should depend on the solvent used. Therefore, the formation of such complex structures and their properties were studied in different solvents previously reported in literature for the preparation of $CH_3NH_3PbI_3$.[111,115–117] Figure 32 shows the PL spectra of PbI_2 solutions in various solvents. Additionally to DMF, gamma-

butyrolactone (GBL), acetonitrile (ACN), N-Methyl-2-pyrrolidone (NMP), dimethyl sulfoxide (DMSO), and water were used.

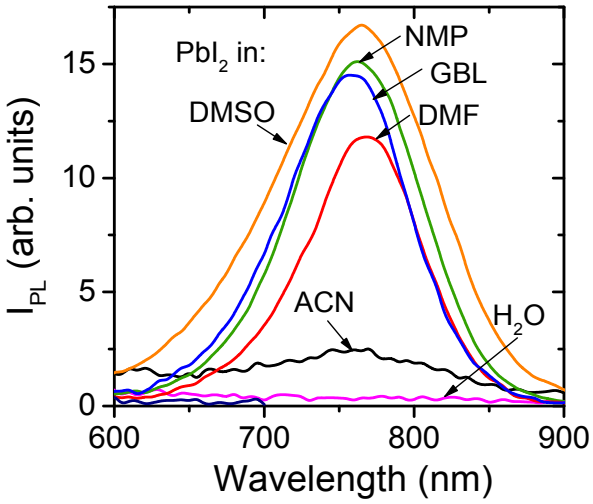

Figure 32. PL spectra of PbI_2 solutions in different solvents: gamma-butyrolactone (GBL), acetonitrile (ACN), N-Methyl-2-pyrrolidone (NMP), dimethyl sulfoxide (DMSO), dimethylformamide (DMF), and water.

Similarly to the solution of PbI_2 in DMF (Figure 31b), the PL spectra of the solutions of PbI_2 in DMSO, NMP, and GBL exhibited a pronounced emission peak at about 760 nm. The solution of lead iodide in acetonitrile (ACN) exhibited only a modest PL intensity around 760 nm. On the other hand, the aqueous solution did not show any PL signal related to lead iodide or the complexes. Moreover, none of the solutions showed PL peak at 530 nm which corresponds to pristine PbI_2. Remarkably, the PL peak position was not altered by an exchange of the solvent. Thus, the structure of the photoactive species might be independent of the solvent used. Such an observation indicates that the emission at 760 nm is due to the complex structures formed through the intermolecular interactions of lead iodide molecules. However, the different PL intensity of the measured solutions suggests a different tendency to the formation of the complexes in different solvents.

The concentration dependency of the PL intensity of lead iodide in DMSO is shown in Figure 33(a). A decrease of the concentration of the solution resulted in a reduction of the intensity of the PL peak at 760 nm. The decrease of the PL intensity was accompanied by an appearance of a PL peak at 500 nm. The solution containing 0.01 mM of lead iodide exhibited both emission peaks at 760 and 500 nm. However, a solution containing 50 µM of PbI_2 exhibited a PL peak at 500 nm only. This behaviour indicates the formation of the solvation shell, which prohibits from the interaction between PbI_2 molecules. The dependence of the PL

intensity on the concentration of PbI_2 solutions in DMSO, DMF, and NMP is presented in Figure 33(b).

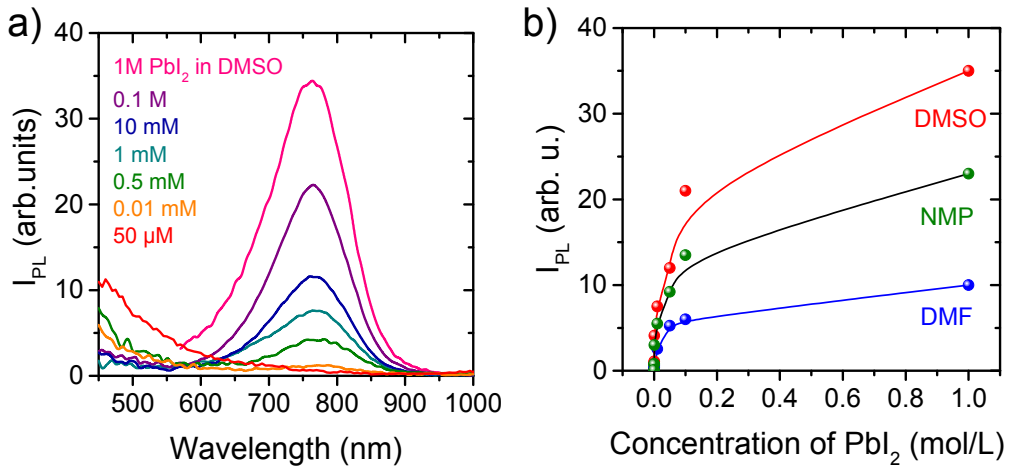

Figure 33. (a) PL spectra of PbI_2 solutions at different concentrations in DMSO. (b) Dependence of the PL intensity on the concentration of PbI_2 solved in DMSO, NMP, and DMF.

Similarly, the influence of concentration on the structure of the complexes was studied with UV-vis spectroscopy. The absorption spectra of lead iodide solutions in NMP are presented in Figure 34(a), the concentrations of the solutions amounted to 0.1 M, 0.05 M, 1 mM, and 10 µM. The solution containing 0.1 M of PbI_2 showed an absorption onset at 450 nm, similarly to Figure 31 (b). A decrease of the concentration to 0.05 M led to an appearance of a fine structure in the absorption spectrum. Specifically, absorption bands at 365, 300, and 250 nm were observed. Further decrease of the concentration led to the reduction of the intensity of the bands at 365 and 300 nm. The absorption bands at about 365, 300, and 250 nm were reported previously as bands related to the different polyiodide plumbate complexes of PbI_2S_4, $PbI_3^-S_3$, and $PbI_4^{2-}S_2$ structure, respectively, where S corresponds to a solvent.[113,118,119] According to literature, these complexes are formed in the presence of an additional source of I^- ions, what is not a case in this study. On the other hand, absorption spectra with a similar fine structure were reported for 1D lead iodide chains.[120]

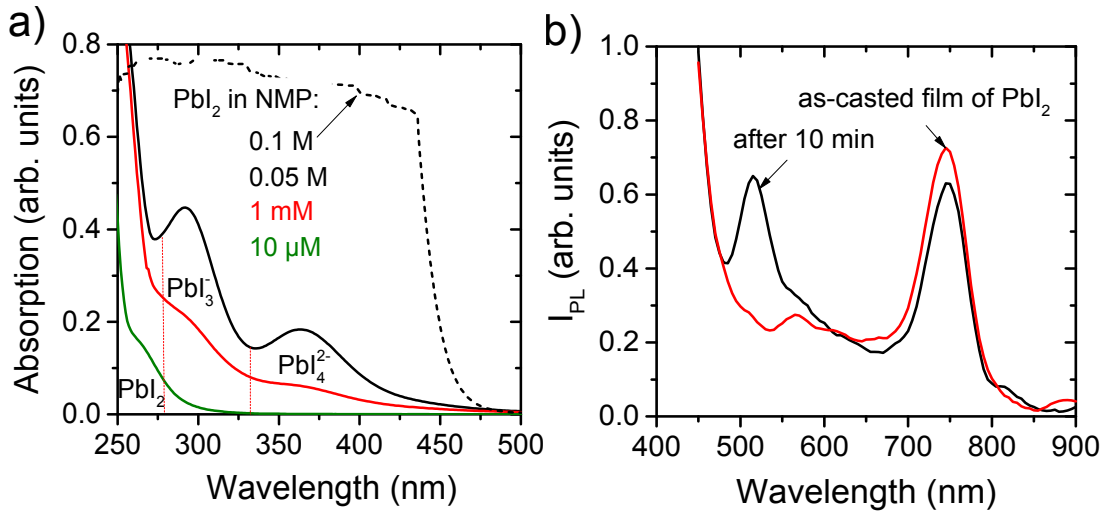

Figure 34. (a) Absorption spectra of the solutions of PbI_2 in NMP where the concentration of PbI_2 was 0.1 M, 0.05 M, 1 mM, and 10 µM. (b) PL spectra of an as-casted lead iodide layer containing DMSO and after 10 min of drying in ambient air at room temperature.

The complexes formed in lead iodide solutions probably are an intermediate stage for the formation of perovskite. Therefore, it is necessary to analyze their stability. The 1 M solution of lead iodide in DMSO was used for casting a film on top of a glass. Figure 34 (b) shows PL spectra of an as-cast film of lead iodide and after 10 minutes of drying in ambient air at room temperature. The as-cast film shows an emission peak around 760 nm. After 10 min of drying, a new peak appeared at about 520 nm. The appearance of this peak indicates the formation of lead iodide due to the evaporation of the solvent. This observation suggests a stabilizing effect of the solvent on polyiodide complexes of lead in solution. Additionally, the ability of the solvents to alter the optical properties of the resulting materials (Figure 30) suggests a strong interaction of the solvents with the perovskite precursors. Therefore, it is plausible that solvent molecules might remain in the perovskite film after annealing. Thus, the $CH_3NH_3PbI_3$ thin films prepared from DMSO were investigated by Fourier-transform infrared spectroscopy (FT-IR). Figure 35 shows the change of the vibrational signature in the most important range of CH_X and NH_X stretching modes of the annealed layer normalized to the pre-annealed layer. The annealing was performed at 100°C for 10, 30, and 60 minutes. The $CH_3NH_3PbI_3$ thin films were pre-annealed at 70 °C for 10 min prior to the annealing step at 100 °C. The intensities of CH_3 related stretching vibrations point upwards since the amount of CH_3 groups (2800 – 3000 cm^{-1}) is reduced with the annealing time at 100 °C.[121] This reduction of CH_3 groups shows that DMSO is driven out during annealing and not methylammonium since no IR peak due to NH_X around 3100 – 3300 cm^{-1} is present in the spectra.[112]

The IR investigation shows that an annealing step for 60 min at 100 °C is needed to markedly reduce the number of solvent molecules by evaporation. This behaviour further confirms the strong binding of the solvent DMSO to polyiodide complexes of lead.

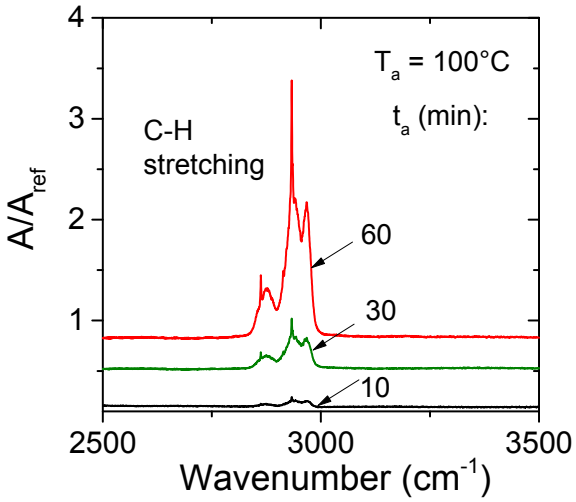

Figure 35. FT-IR spectra of the $CH_3NH_3PbI_3$ thin film prepared from DMSO in the range of CH_X and NH_X stretching modes. The spectra were recorded after annealing at 100 °C for 10, 30, and 60 min. The IR spectra were normalized to the spectrum of $CH_3NH_3PbI_3$ thin film pre-annealed at 70 °C for 10 min.

Furthermore, the structures of the complexes were analyzed with x-ray diffraction (XRD) method. Figure 36 shows x-ray diffractograms of a PbI_2 thin film and a lead iodide solution in DMSO, a PbI_2·n(DMSO) powder extracted from the same solution and a $CH_3NH_3PbI_3$ thin film obtained from the DMSO-based solution. The PbI_2·n(DMSO) powder was prepared by precipitation of PbI_2·n(DMSO) with toluene from 1 M solution of PbI_2 in DMSO. The diffractogram of pristine PbI_2 consists of four main reflexes at 12.6, 25.5, 38.6, and 52.3° corresponding to the hexagonal crystal structure of lead iodide.[122] The x-ray diffractograms of lead iodide in solution shows diffraction peaks, indicating the presence of a long-range order in the solution. In addition, the diffractograms exhibited all of the reflexes ascribable to the hexagonal PbI_2 phase. This observation indicated the formation of PbI_2-clusters already in the solution.

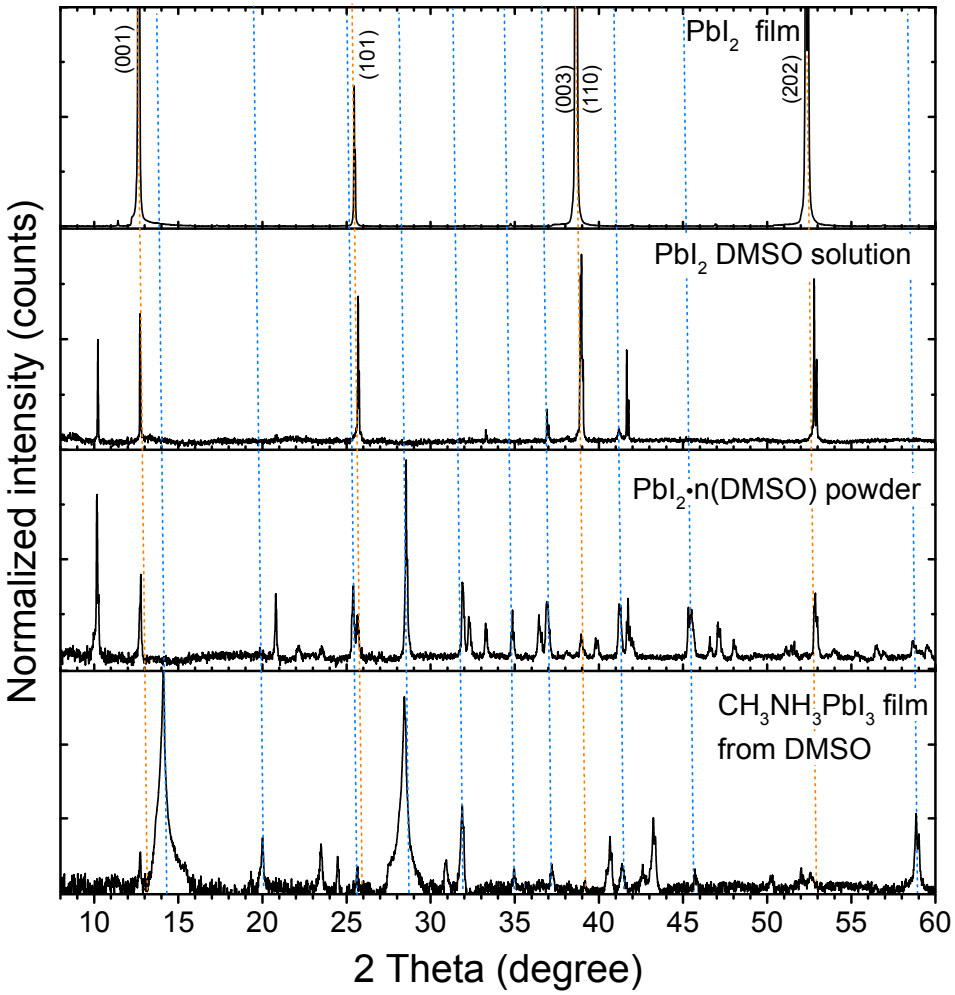

Figure 36. X-ray diffractograms of a $CH_3NH_3PbI_3$ thin film, PbI_2·n(DMSO) powder, a 1 M PbI_2 solution in DMSO and a PbI_2 thin film.

The diffractogram of the extracted PbI_2·n(DMSO) powder revealed a similar pattern as the solution of PbI_2 in DMSO. The peaks corresponding to the pristine PbI_2 were accompanied by the reflexes at 10.1, 36.8, 41.06, and 41.6° observed in the solution. The new, additional reflexes occur at the same positions as the peaks ascribable to the tetragonal structure of $CH_3NH_3PbI_3$. The peak positions of the $CH_3NH_3PbI_3$ are marked with blue dashed lines, orange dashed lines indicate the position of the PbI_2 reflexes.

The results shown in this chapter indicate the formation of complex structures in the solutions of $CH_3NH_3PbI_3$ and pure PbI_2. These complexes exhibited a similar to $CH_3NH_3PbI_3$ thin films photoluminescence at about 760 nm. This behaviour indicates a strong link between optical properties of PbI_2 complexes and hybrid perovskites. Thus, the structures of these complexes and their relation to hybrid perovskites will be further discussed in Chapter 5.

4.2. Stability of hybrid perovskites

4.2.1. Influence of temperature on properties of $CH_3NH_3PbI_3$

This chapter addresses the influence of temperature on properties of $CH_3NH_3PbI_3$. Figure 37 shows a dependence of surface temperature, T_s, of a perovskite layer on top of an FTO-coated glass substrate and TiO_2 layer on time of annealing, t_{ann}. The dependence was measured as a function of different set temperatures, T_{set}, of the heating plate.

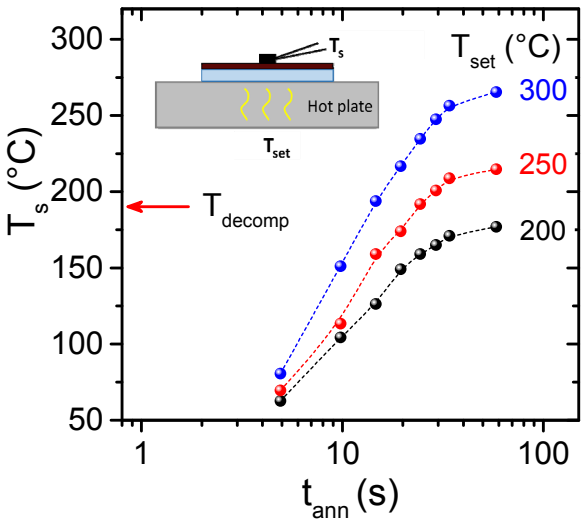

Figure 37. Dependence of the surface temperature (T_s) of $CH_3NH_3PbI_3$ on top of FTO coated glass on time of annealing (t_{ann}) for set temperatures (T_{set}) of 200, 250, and 300 °C. The inset shows a schematic representation of the setup used for measurement of T_s. Reproduced with permission from Ref.[49] Copyright 2017 American Chemical Society.

To study the influence of the surface temperature on properties of $CH_3NH_3PbI_3$, three set temperatures of the heating stage were chosen (T_{set} = 200, 250, and 300 °C) to obtain a broad range of T_s. A slow saturation rate of the surface temperature allows controlling the temperature of a perovskite layer by adjusting the annealing time. Higher set temperature leads to a faster saturation of the surface temperature. The inset in Figure 37 represents a schematic setup used for the measurement of the surface temperature. The setup consisted of a hot plate set at T_{set} = 200, 250, 300 °C, the perovskite layer on top of an FTO-coated glass and TiO_2, and a thermocouple. The samples were placed on top of a hot plate at given T_{set} and the time dependence of the surface temperature (T_s) evolution was recorded.

The influence of the surface temperature on the morphology of $CH_3NH_3PbI_3$ thin films is shown in Figure 38. The samples were post-annealed at T_{set} = 200, 250, and 300 °C for t_{ann} = 5,

15, and 25 s. The reached surface temperatures are indicated in white rectangles. The top view scanning electron microscope (SEM) micrographs of the specimens annealed at the lowest surface temperature, T_s = 61 °C (T_{set} = 200 °C for 5 s), showed a polycrystalline film with about 100 nm grain size. (a.1, Figure 38). The same morphology was observed for all samples annealed at T_s < 100 °C independent of the used T_{set} (b.1, c.1, Figure 38). When the surface temperature was increased to 125 °C, a small increase of the grain size was observed.

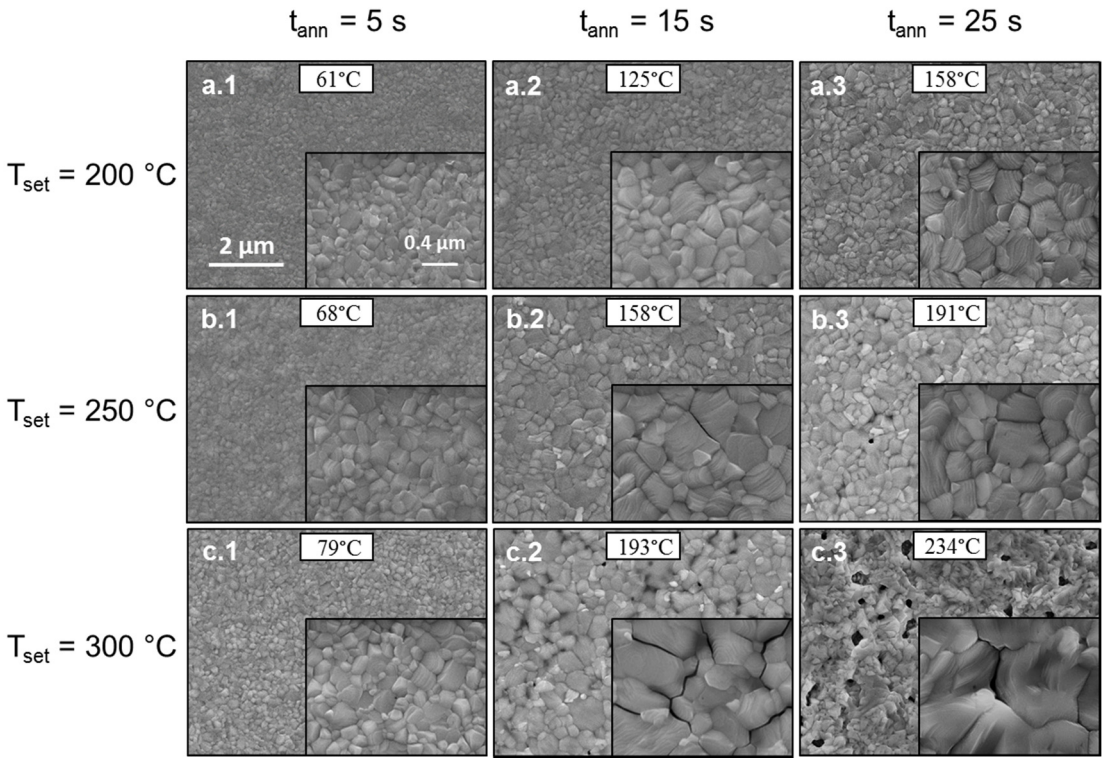

Figure 38. Top view SEM micrographs of the $CH_3NH_3PbI_3$ layers after post-annealing at T_{set} = 200 (a), 250 (b), and 300 °C (c) during t_{ann} = 5, 15, and 25 s. The white insets indicate the surface temperature reached after the indicated annealing time at the given set temperature.

The grain size increased significantly when the surface temperature reached T_s = 158 °C (b.2, a.3, Figure 38). However, a further increase of T_s to $T_s \geq 190$ °C led to the formation of microscopic holes which indicate the onset of the decomposition of the material. Severe decomposition features occurred at T_s = 234 °C (c.3, Figure 38). The observed decomposition temperature of about 190 °C is consistent with previous reports in the literature.[123] Thus, the decomposition of $CH_3NH_3PbI_3$ at this T_s was correlated with the evaporation of methylammonium iodide.

According to Figure 37, usage of the lowest set temperature (T_{set} = 200 °C) allows longer post-annealing of the samples at temperatures $T_s < T_{decomp}$ due to the slower saturation of T_s.

The influence of prolonged t_{ann} on the morphology of the specimens is shown in Figure 39. The increase of the annealing time to 35 s resulted in an increase of T_s to 170 °C accompanied by a significant enhancement of the morphology of the specimen. Further prolongation of the post-annealing process led to a rather modest increase of T_s by 6 °C (176 °C), however, the grain size of the specimen increased vastly to about 1 µm. Moreover, the specimens did not exhibit any signs of decomposition.

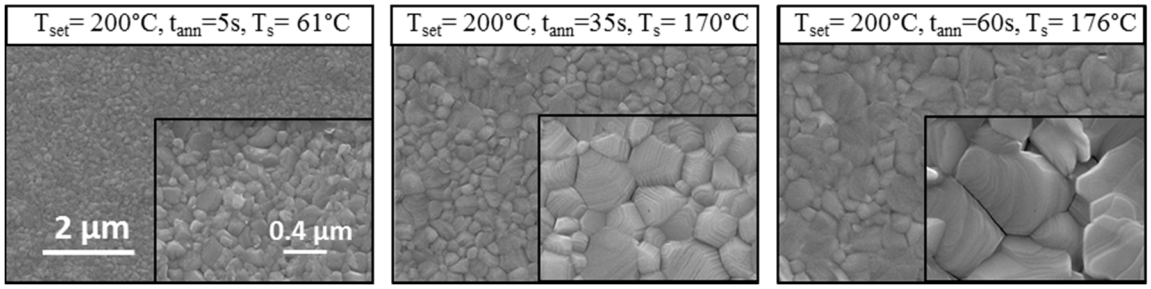

Figure 39. Top view scanning electron micrographs of $CH_3NH_3PbI_3$ layers after post-annealing at T_{set} = 200 °C for t_{ann} = 5, 35, and 60 s. Surface temperatures of T_s = 61, 170, and 176 °C were reached, respectively. Reproduced with permission from Ref.[49] Copyright 2017 American Chemical Society.

Cross-sectional SEM micrographs of the as-prepared $CH_3NH_3PbI_3$ layer and after annealing at T_s = 176 °C demonstrate the influence of the post-annealing on the grain size (Figure 40). The as-prepared sample had a thickness of about 345 nm and the average grain size was approximately 150 nm. This resulted in the presence of numerous grain boundaries parallel to the substrate. After annealing at T_s = 176 °C the microscopic structure of the samples changed significantly. The grain boundaries parallel to the substrate vanished completely and the grains extended from the surface of the sample to the substrate. This led to the formation of the grains with a grain diameter exceeding the film thickness.

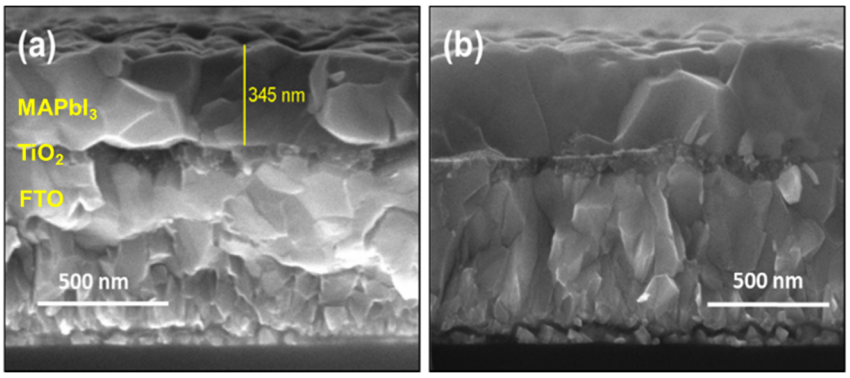

Figure 40. Cross-sectional SEM micrographs of an as-prepared (a) and post-annealed sample at T_s = 176 °C (b). The samples were prepared on top of an FTO-coated glass and TiO_2 layer. Adapted with permission from Ref.[49] Copyright 2017 American Chemical Society.

The top view SEM micrographs were used for calculation of an average grain size of the specimens after post-annealing. Figure 41(a) shows the average grain size, <x>, of the samples as a function of surface temperature. The dashed line and arrow indicate the decomposition temperature of $CH_3NH_3PbI_3$. Interestingly, an intense grain-growth was observed only at temperatures T_s > 150 °C. Moreover, the largest grain size of the specimens was obtained by annealing at the highest surface temperature (T_s = 234 °C, t_{ann} = 25 s) or longer annealing time at lower temperature (t_{ann} = 60 s, T_s = 176 °C). Although both approaches led to large grain sizes of about 1 µm, only annealing at T_s = 176 °C resulted in non-degraded samples with the grain size of <x> = 1048 nm.

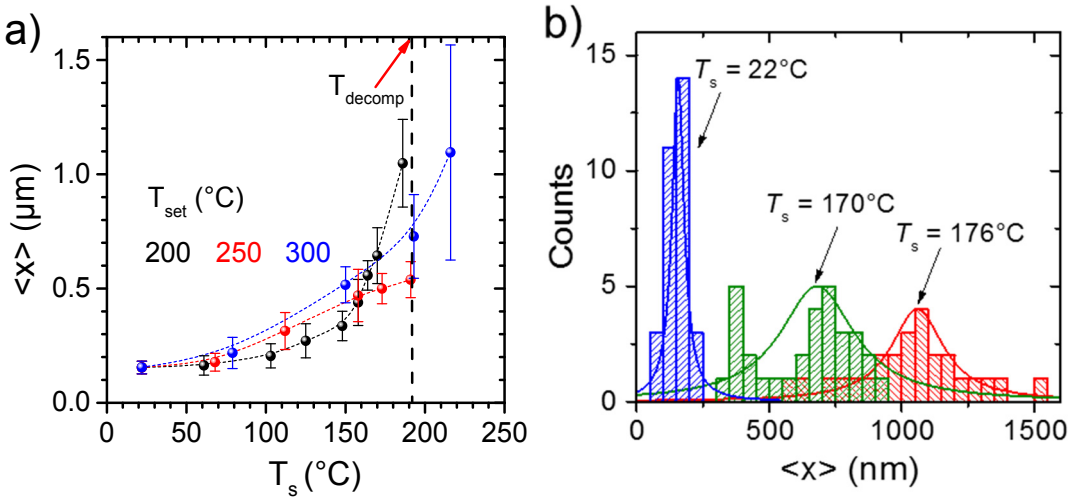

Figure 41. (a) Average grain size, <x>, of the post-annealed $CH_3NH_3PbI_3$ layers as a function of T_s, reached at T_{set} = 200, 250, and 300 °C. The error bars represent standard deviation. (b) Grain-size distribution of as-prepared (22 °C) and post-annealed samples at T_{set} = 200 °C. Reproduced with permission from Ref.[49] Copyright 2017 American Chemical Society.

The grain size distribution is presented in Figure 41 (b) for as-prepared (T_s = 22 °C) and post-annealed at T_s = 170 and 176 °C $CH_3NH_3PbI_3$ layers. The as-prepared sample exhibited an average grain size of about 150 nm with sharp grain size distribution. The specimen after annealing at T_s = 170 °C exhibited the increase of the average grain size to <x> = 644 nm. Interestingly, this specimen showed a bimodal grain size distribution with a second maximum at <x> = 400 nm. The specimen annealed at T_s = 176 °C showed a broad monomodal distribution of the grain size with an average value of 1048 nm. This behaviour indicates a possible secondary grain growth as a mechanism of the increase in the grain size with the rise of the surface temperature.

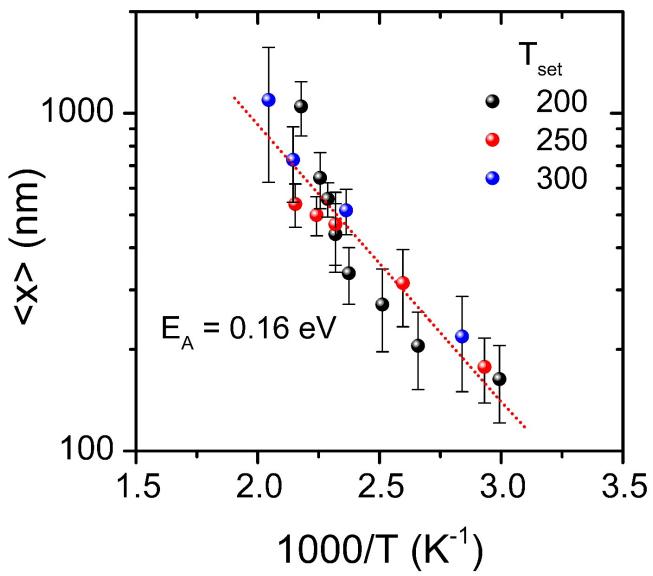

Figure 42. Dependence of the average grain size on the inverse temperature of the post-annealed $CH_3NH_3PbI_3$ layers at T_{set} = 200, 250, and 300 °C. Reproduced with permission from Ref.[49] Copyright 2017 American Chemical Society.

Since the grain growth exhibited a thermally activated behavior, an activation energy of the growth was calculated. Figure 42 shows the dependence of the average grain size on the inverse temperature for the specimens post-annealed at T_{set} = 200, 250, and 300 °C. The dependence exhibited a linear trend. This dependence is known as Arrhenius plot and a slope of a linear fit corresponds to the activation energy of the growth process. Therefore, the slop of a least-squares fit of the data was used for the calculation of the activation energy. The activation energy amounted to E_a = 0.16 eV.

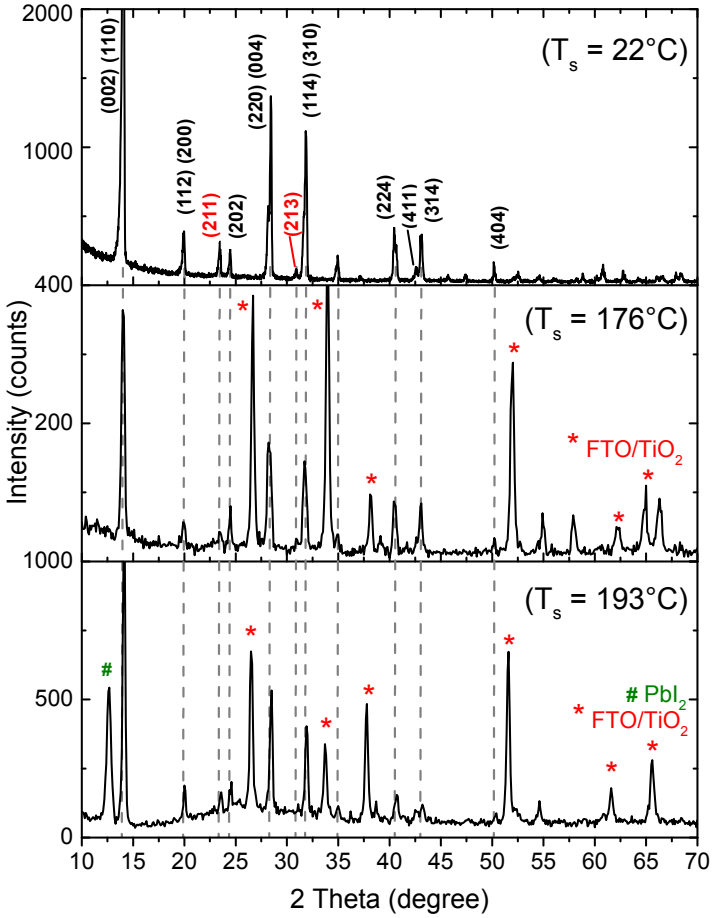

Figure 43. X-ray diffractograms of as-prepared $CH_3NH_3PbI_3$ layer (T_s = 22 °C) and post-annealed at T_s = 176 and 193 °C. Red asterisks indicate the reflexes attributed to the FTO- coated glass substrate and TiO_2. The green hashtag indicates the (001) reflex ascribed to the hexagonal lattice of PbI_2. Reproduced with permission from Ref.[49] Copyright 2017 American Chemical Society.

Post-annealing at different surface temperatures confirmed the strong influence of the temperature on the morphology of $CH_3NH_3PbI_3$ layers. According to literature and the experimental data (Figure 38), the decomposition of the material commences at temperatures above 190 °C.[123] Nevertheless, it is necessary to ensure the absence of the damage in specimens annealed at $T_s < T_{decomp}$. X-ray diffractograms are presented in Figure 43 of an as-prepared $CH_3NH_3PbI_3$ layer and layers after post-annealing with the largest values of <x> (T_s = 176 and 193 °C). The as-prepared sample (T_s = 22 °C) exhibited reflexes ascribable to the perovskite phase reported elsewhere.[124] The presence of the diffraction peaks (211) and (213) at 23.4 and 30.9 °, respectively, indicates the tetragonal crystalline lattice of the perovskite phase. Therefore, all reflexes of the as-prepared specimen were assigned to *I4/mcm* symmetry. The specimen annealed at T_s = 176 °C showed the same position of the reflexes ascribable to the tetragonal crystalline lattice. The specimen was prepared on top of an FTO-coated glass and

TiO_2 layer, therefore, the peaks attributed to these layers are marked with red asterisks. Interestingly, the specimen annealed at T_s = 176 °C did not show any signs of the decomposition. On the contrary, the x-ray diffractograms of the specimen annealed at T_s = 193 °C showed a strong diffraction peak at 12.6 °, while showing a general similarity of the position of the main reflexes. The peak at 12.6 ° is attributed to (001) reflex of hexagonal PbI_2. The (001) reflex is indicated by a green hashtag. This observation supports the presence of PbI_2 as a product of the decomposition of the material due to the loss of methylammonium iodide in the film. In addition, this behavior is consistent with the decomposition of the specimens observed in SEM micrographs (Figure 38).

The influence of high-temperature post-annealing on the optical and electronic properties was studied with photoluminescence (PL) spectroscopy. The PL spectra of the specimens annealed at T_{set} = 200 °C are presented in Figure 44 (a) in comparison to the as-prepared $CH_3NH_3PbI_3$ layer (T_s = 22 °C). The as-prepared sample exhibited a strong PL signal at 777 nm corresponding to the band gap of 1.6 eV which is in a good agreement with literature.[125] The specimens after post-annealing exhibited a stronger PL intensity when compared to the as-prepared sample. The intensity of the PL peak of the sample annealed at T_s = 176 °C was enhanced by about 80 % in comparison to the as-prepared sample. This improvement is due to the reduction of the defect density in the samples with larger grain-size. Moreover, the specimens after annealing at T_{set} = 200 °C exhibited a shift of the maximum of the PL peak to longer wavelengths with an increase of T_s. The sample annealed at T_s = 176 °C showed a PL peak at 782 nm. This corresponds to a reduction of the band-gap by about 20 meV. The same behavior was observed for the $CH_3NH_3PbI_3$ layers annealed at T_{set} = 250 and 300 °C.

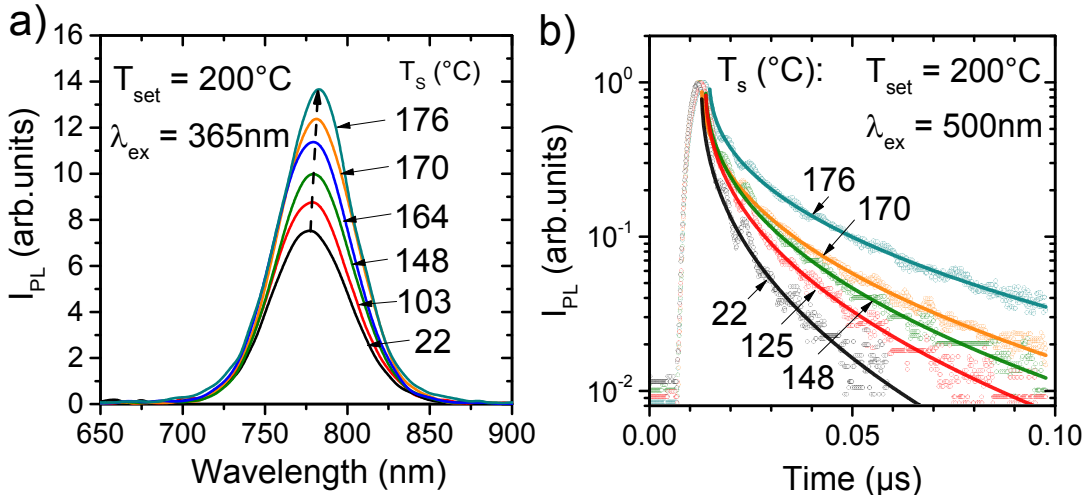

Figure 44. (a) Photoluminescence spectra of an as-prepared $CH_3NH_3PbI_3$ layer on top of a glass substrate and post-annealed at T_{set} = 200 °C. The spectra were taken after the indicated

temperatures, T_s, were reached. The samples were excited with a pulsed laser (λ_{ex} = 365 nm). (b) Time-resolved photoluminescence intensity of as-prepared $CH_3NH_3PbI_3$ layer on top of a glass substrate and post-annealed at T_{set} = 200 °C. The excitation wavelength was λ_{ex} = 500 nm. Adapted with permission from Ref.[49] Copyright 2017 American Chemical Society

Figure 44 (b) shows the time-resolved photoluminescence intensity of the as-prepared (T_s = 22 °C) and post-annealed $CH_3NH_3PbI_3$ layers (T_{set} = 200 °C). A strong dependence of the decay of the PL intensity on surface temperature was observed for the specimens after post-annealing. The decay of the PL was fitted with stretched exponential to obtain the lifetime of the charge carriers. The post-annealed samples showed an increase of the lifetime with an increase of T_s. $CH_3NH_3PbI_3$ layer annealed at T_s = 176 °C exhibited a lifetime of the charge carriers of 5 ns in comparison to 1.4 ns of the as-prepared sample. This observation corresponds to the improvement of the quality of the material and is consistent with the rise of the PL intensity (Figure 44a).

The increased lifetime of the charge carriers of the specimens with the enhanced grain size indicated a possible increase in the diffusion length of charge carriers. Therefore, the diffusion length of the light-induced charge carriers (L) was studied with surface photovoltage (SPV) method after Goodman as a function of the grain size. Figure 45 (a) shows the dependence of the light intensity required for constant SPV signal on the absorption length of $CH_3NH_3PbI_3$ layer annealed at T_s = 176 °C. The light intensity required for keeping the SPV signal constant is in a direct correlation with the wavelength and intensity of the SPV signal. The measurement was conducted for SPV signals of 20, 30, 40, and 50 μV. The intersection of the linear fit of the light intensity dependence with the x-axis gives the negative value of the diffusion length of the light-induced charge carriers (L). The specimen with the average grain size of 1048 nm exhibited a diffusion length of about 900 nm.

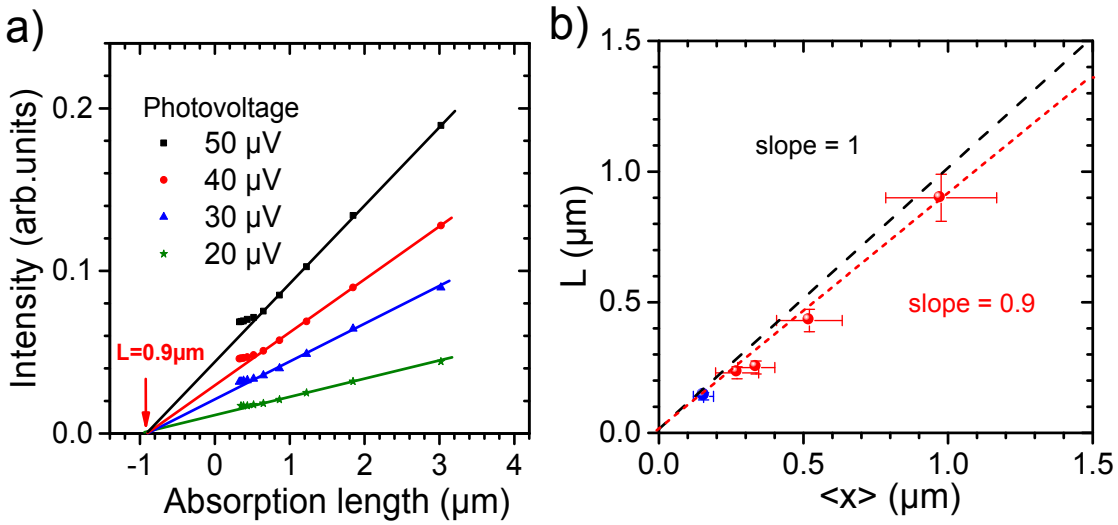

Figure 45. (a) Dependence of the light intensity required for keeping the surface photovoltage signals (20, 30, 40, and 50 µV) constant on absorption length of $CH_3NH_3PbI_3$. The measurements were performed on a post-annealed sample at T_s = 176 °C. (b) Dependence of the diffusion length of the charge carriers, L, on the average grain-size, <x>, determined from SEM micrographs of as-prepared and post-annealed $CH_3NH_3PbI_3$ layers at T_{set} = 200 °C. The error bars represent the standard deviation of the grain-size measurement and accuracy of SPV method. Reproduced with permission from Ref.[49] Copyright 2017 American Chemical Society.

The SPV measurements after Goodman were conducted on the as-prepared $CH_3NH_3PbI_3$ layer and after annealing at T_{set} = 200 °C. Figure 45 (b) presents the dependence of the diffusion length, L, on the average grain size, <x>. Interestingly, the diffusion length of $CH_3NH_3PbI_3$ is in direct correlation with the grain size. The samples after annealing exhibited a linear increase of L from 150 nm for the as-prepared sample (<x> = 150 nm) to 900 nm for the specimen annealed at T_s = 176 °C (<x> = 1048 nm). Moreover, the linear fit of the data showed a slope of 0.9. This behavior clearly indicates that the diffusion length is limited by the grain size.

To investigate the influence of the crystalline and electronic properties of the material on the photovoltaic performance of the devices, the as-prepared and subjected to the post-annealing $CH_3NH_3PbI_3$ layers were used as absorbers in solar cells. Figure 46 (a) shows the current-voltage characteristics of the solar cells based on the as-prepared $CH_3NH_3PbI_3$ layer (T_s = 22 °C, red curves) and after annealing at T_s = 176 °C (black curves). The direction of the IV scan is indicated by arrows.

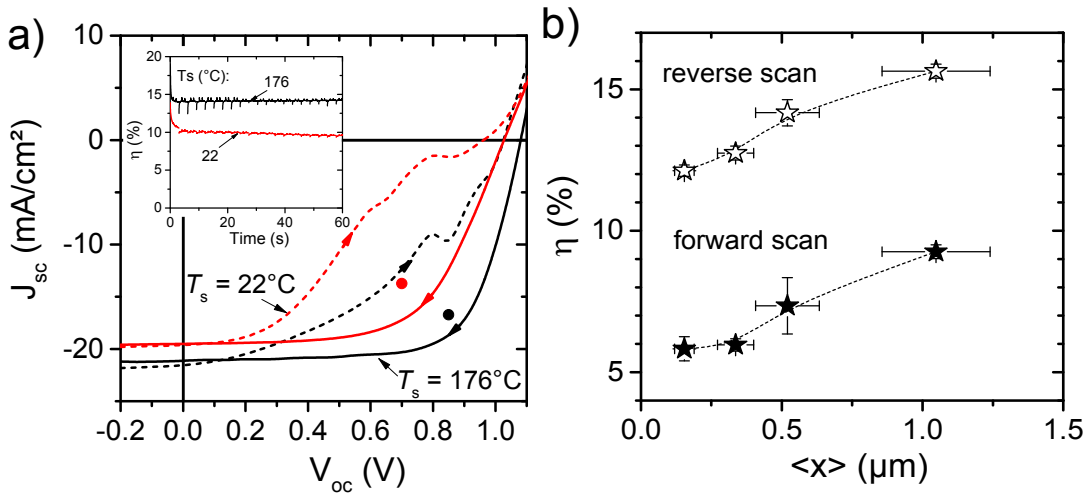

Figure 46. (a) Current-voltage characteristics of the solar cells with the as-prepared (T_s = 22 °C, red curve) and post-annealed at T_s = 176 °C (black curve) $CH_3NH_3PbI_3$ layer. The arrows indicate the direction of the scan and the circles indicate stabilized power output after maximum power-point tracking for 60 s. The inset shows the power conversion efficiency during maximum power-point tracking of the corresponding devices. (b) The dependence of the power conversion efficiency in forward and reverse directions on the average grain size of the absorber layer. The error bars represent the standard deviation of the power conversion efficiency and the average grain size. Reproduced with permission from Ref.[49] Copyright 2017 American Chemical Society.

The as-prepared sample exhibited an open circuit voltage of V_{oc} = 1.02 V and a short circuit current of J_{sc} = 19.8 mA/cm^2. The specimen after post-annealing at T_s = 176 °C showed an increase in both open circuit voltage and short circuit current resulting in V_{oc} = 1.1 V and J_{sc} = 21.5 mA/cm^2. Both devices exhibited a strong hysteresis. Therefore, maximum power-point tracking was performed to obtain an accurate value of the power conversion efficiency. The power conversion efficiency during maximum power-point tracking of the devices is shown in the inset. The stabilized power conversion efficiency after 60 s is depicted by red and black dots for the as-prepared $CH_3NH_3PbI_3$ layer (T_s = 22 °C) and after annealing at T_s = 176 °C, respectively. The stabilized power conversion efficiency of the as-prepared sample with <x> = 150 nm amounted to η = 9.5 %. The increase of the grain size and the diffusion length of the charge carriers led to an enhanced power conversion efficiency of η = 14 % for the specimen annealed at T_s = 176 °C.

Figure 46 (b) shows a dependence of the photovoltaic performance of the device based on perovskite layer subjected to the post-annealing at T_{set} = 200 °C on the grain size. The power conversion efficiency increased in both forward and reverse directions with the increase of the

grain size. The error bars represent the standard deviation of the power conversion efficiency and the grain size.

In this chapter, the influence of temperature on properties of $CH_3NH_3PbI_3$ thin films was demonstrated. The post-annealing procedure below decomposition temperature led to a drastic enhancement of grain size and, as a result, the optical and electronic properties of the films. In addition, the photovoltaic performance of the devices with large grains was increased noticeably. The mechanism of this grain growth will be discussed in more details in Chapter 5.

4.2.2. Compositional stability of hybrid perovskites

Phase segregation in mixed $CsPb(I_{1-x}Br_x)_3$ perovskite

In this chapter, the compositional stability of mixed $CsPb(I_{1-x}Br_x)_3$ perovskites was studied. The band gap of all-inorganic perovskite $CsPbI_3$ was tuned by altering the content of bromide ions in mixed $CsPb(I_{1-x}Br_x)_3$ material. Figure 47 (a) shows Tauc plots of the thin films of $CsPb(I_{1-x}Br_x)_3$ with a different content of bromide, x. The film of pure $CsPbI_3$ exhibited the onset of light absorption at 1.75 eV, which is in a good agreement with the band gap reported in literature.[126] Addition of x = 0.16 of Br led to the shift of the absorption onset to 1.79 eV. Further increase of the bromide content led to an increase in the band gap. The film of pure $CsPbBr_3$ exhibited a band gap of 2.36 eV. Therefore, alteration of the content of bromide allowed tuning the band gap in a range from 1.75 to 2.36 eV. The dependence of the band gap on the content of Br in the material is presented in Figure 47 (b). Theoretical values of the band gap as a function of the composition were calculated according to Vegard's law (Chapter 2). Interestingly, the measured band gap shows a small deviation from the calculated values. However, the band gap follows a linear trend in a broad range of the bromide content indicating a comparable to the predicted amount of Br incorporated into the film.

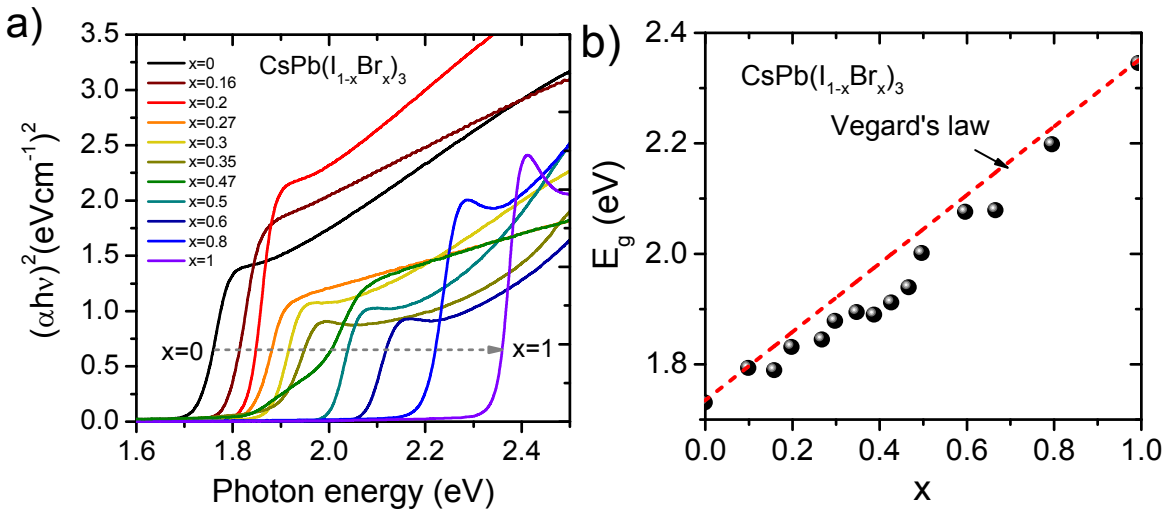

Figure 47. (a) Tauc plots of thin films of $CsPb(I_{1-x}Br_x)_3$ prepared by the one-step spin-coating procedure. (b) Band gap, E_g, of $CsPb(I_{1-x}Br_x)_3$ obtained from corresponding Tauc plots as a function of Br content, x. Dashed line represents the theoretical band-gap calculated according to the Vegard's law.

The corresponding specimens were additionally studied with photoluminescence spectroscopy. Normalized PL spectra of $CsPb(I_{1-x}Br_x)_3$ layers are presented in Figure 48 (a). Pristine $CsPbI_3$ (x =0) exhibited an emission peak maximum at 709 nm, corresponding to the

band gap of 1.75 eV what is similar to E_g obtained from Tauc plot (Figure 47a). Similarly to the behavior of the absorption onset, the PL of the specimens shifts to shorter wavelength with increasing content of bromide. Material with x = 0.1 of bromide showed a pronounced shift of the luminescence to 683 nm. The sequential increase of the content of bromide induced a further shift of the PL peak. Interestingly, the material with x = 0.3 exhibited a strong broadening of the photoluminescence peak. In addition, further increase of Br content led to an appearance of a second peak at longer wavelength.

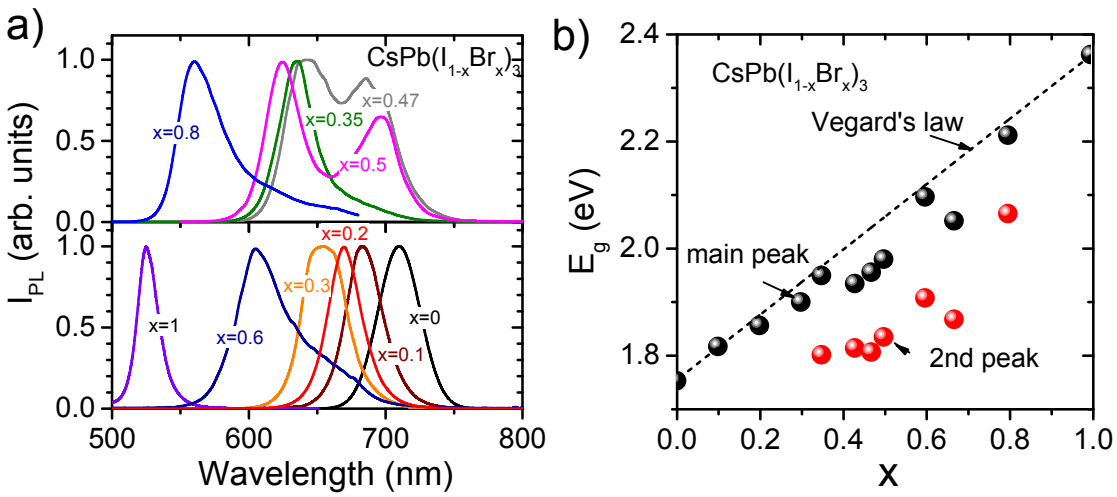

Figure 48. (a) PL spectra of $CsPb(I_{1-x}Br_x)_3$ prepared by the one-step spin-coating procedure. (b) Dependence of the band gap, E_g, on the content of bromide in $CsPb(I_{1-x}Br_x)_3$. The band gap values are calculated from corresponding PL spectra.

The second peak became pronounced with an increase of the bromide content to x = 0.47. Further increase of x led to the decrease of the intensity of the second peak to a shoulder only. The second peak disappeared when the content of Br reached x = 1. Figure 48 (b) shows the band gap calculated from corresponding PL spectra as a function of the Br content. The main PL peak is presented in black, the position of the second peak is indicated in red. Interestingly, the main PL maximum shifted towards larger values of the band gap independently on the appearance of the second peak. Moreover, the second peak showed a similar shift of the position with an increase of the content of bromide. In addition, a constant discrepancy of 0.15 eV between main and the second peak can be observed. Similarly to other hybrid perovskites, this observation indicated a segregation of the materials with high content of bromide into two phases: iodide-rich and mixed phase (Chapter 2.4.2).

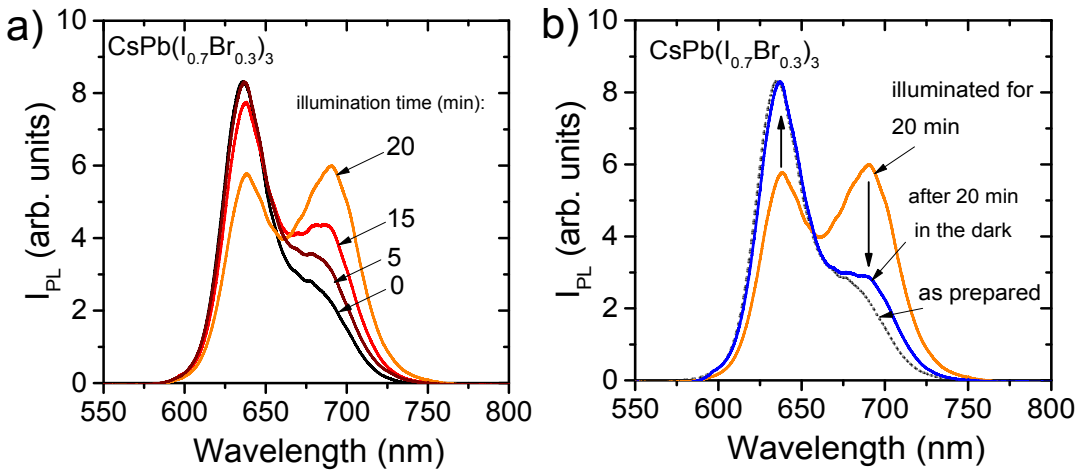

Figure 49. (a) Change of the PL spectrum of a $CsPb(I_{0.7}Br_{0.3})_3$ layer during illumination with a 450 nm laser. The layer was prepared by the one-step spin-coating procedure. (b) PL spectrum of the layer illuminated for 20 min using 450 nm laser and after 20 min storing in the dark.

To analyze the influence of light on the stability of the mixed halide perovskite materials, the specimen with x = 0.3 was chosen. Figure 49 (a) shows an evolution of the PL spectra of $CsPb(I_{0.7}Br_{0.3})_3$ with illumination at 450 nm with time. The thin film of $CsPb(I_{0.7}Br_{0.3})_3$ was prepared by the one-step spin-coating procedure. The PL spectrum of the as-prepared film exhibited an intense peak at about 638 nm and a small shoulder at about 670 nm. The intensity of the PL of the shoulder increased noticeably after the specimen was illuminated for 5, 10, and 20 min with a laser at 450 nm excitation wavelength. After 20 min of illumination, the intensity of the main peak dropped to 70 % of the initial value, while the intensity of the second peak increased to 72 % of the intensity of the main peak. Then, the specimen was placed for 20 min in the dark. Surprisingly, this procedure led to the change of the intensity of both PL maxima back to their initial values (Figure 49b). This observation indicates a reversible character of light-induced segregation.

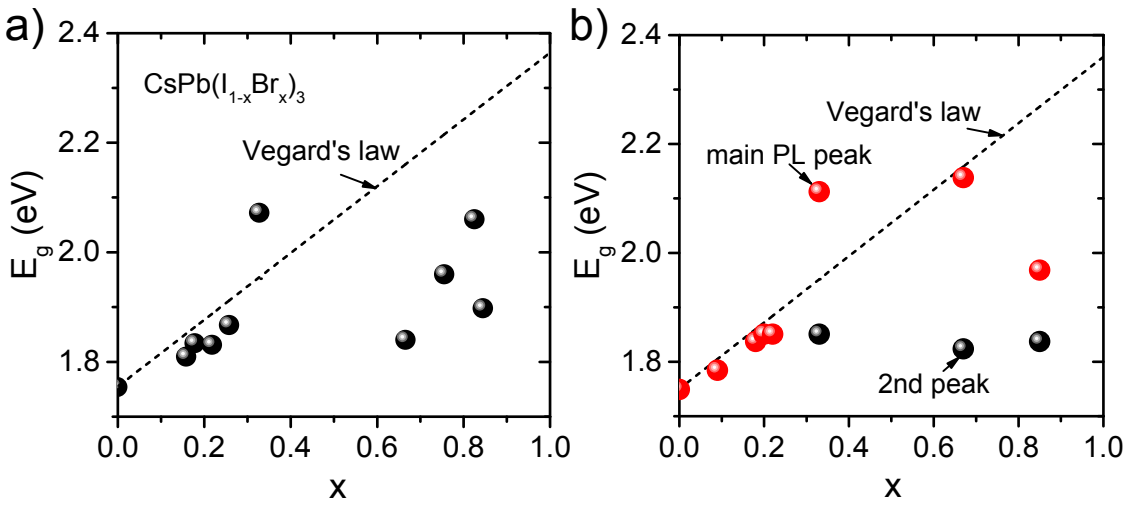

Figure 50. Dependence of the band gap of $CsPb(I_{1-x}Br_x)_3$ on the content of bromide, x. The band gap was determined from Tauc plots (a) and from PL spectra (b).

To investigate the influence of the preparation method on the properties of the $CsPb(I_{1-x}Br_x)_3$, layers containing different amount of Br were prepared by the two-step spin-coating (see Chapter 3, Page 42). The specimens were analyzed by means of absorption and photoluminescence spectroscopies. Figure 50 shows the dependence of the band gap obtained from Tauc plot (a) and from the PL peak maxima (b) on the content of Br. The specimen with $x = 0$ exhibited the band gap of 1.75 eV, see Figure 50 (a). An addition of $x = 0.16$ of Br led to the increase of the absorption onset to 1.8 eV. Moreover, the addition of Br up to $x = 0.3$ showed a linear dependence of the band gap on x. However, further increase of the bromide content led to a discontinuity of the linear trend and formation of the material with significantly lower band-gap then predicted by Vegard´s law.

Similarly to the absorption measurements, the specimens containing $0 < x < 0.3$ of Br showed a linear dependence of the optical band-gap on x following the Vegard's law, see Figure 50 (b). Furthermore, the specimens containing $x > 0.3$ exhibited a strong deviation from the linear trend. In addition, an evolution of the second peak was observed in the PL spectra of the specimens with $x > 0.3$. Interestingly, the position of the second PL peak maximum remained constant at about 1.8 eV, while the maximum of the main peak shifted towards higher energy values. This observation indicates the formation of two phases of the $CsPb(I_{1-x}Br_x)_3$ material, which can be assigned as I-rich and Br-rich with corresponding PL position at ≈ 1.8 eV and ≈ 2.1 eV respectively.

Influence of ethylenediammonium diiodide on properties of $CH_3NH_3PbI_3$/EDDI blends

In this chapter, the influence of a large cation, ethylenediammonium diiodide, on the properties and stability of the mixed hybrid perovskites was investigated. Figure 51 shows the chemical structure of the ethylenediammonium diiodide (EDDI or $C_2H_4(NH_3I)_2$) in comparison to the methylammonium cation. The indicated scale bar represents the ionic radius of the methylammonium cation of methylammonium iodide taken from the literature.[127] The ionic radius of the ethylenediammonium cation can be estimated as twice the value of the methylammonium cation.

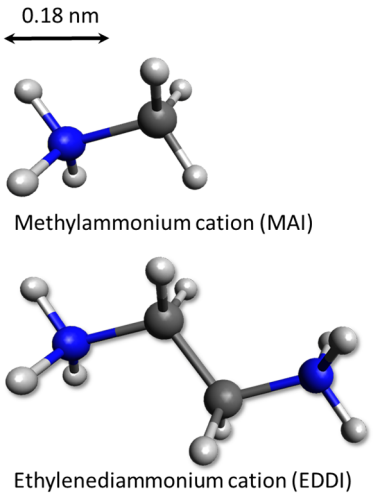

Figure 51. Chemical structure of methylammonium (top) and ethylenediammonium (bottom) cations. The scale bar represents an ionic radius of the methylammonium cation reported in the literature.[127]

First, the influence of ethylenediammonium diiodide (EDDI) in EDDI/$CH_3NH_3PbI_3$ perovskite blends was studied with PL and UV/Vis spectroscopies (Figure 52). Figure 52 (a) shows the normalized PL spectra of the layers as a function of the EDDI molar fraction, $x_{(EDDI)}$. Pristine $CH_3NH_3PbI_3$ perovskite is indicated as 0 % of EDDI. This sample shows a PL maximum at 783 nm, that corresponds to a band gap energy of 1.58 eV. This value is in a good agreement with literature.[32] When only 0.05 % of EDDI was added to $CH_3NH_3PbI_3$, the PL spectrum shows a blue shift of the peak by 4.3 nm to 779 nm. This corresponds to an increase of the band gap by 0.01 eV. The increase of the EDDI content results in a further pronounced blue shift of the maximum of the PL peak. Blends with 0.6 % of EDDI exhibited an optical band-gap of E_g = 1.74 eV.

Complementary to the PL measurements, transmission and reflectance spectra were acquired to correlate the shift of the optical band-gap with the amount of EDDI. In Figure 52 (b) the Tauc plots are shown. The optical band-gap was determined by extrapolating the linear region of the absorption onset to the axis of the abscissae. Similar to the PL spectra shown in Figure 52 (a), a systematic blue shift of the absorption onset was observed with increasing EDDI content.

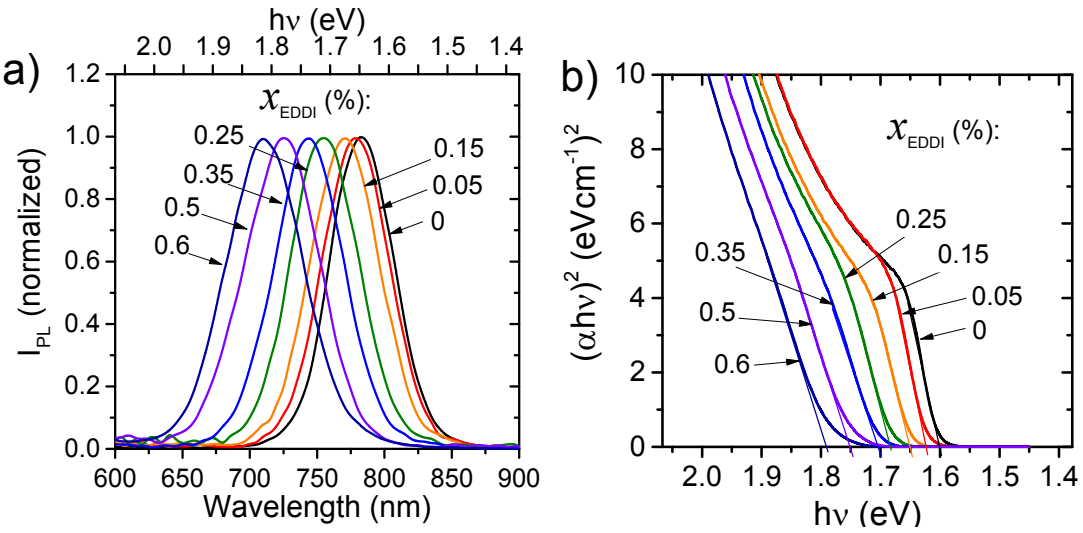

Figure 52. (a) PL spectra of the films of $CH_3NH_3PbI_3$/EDDI blends, where molar fraction of EDDI was varied between 0 and 0.6 %. 0% of EDDI represents a pristine $CH_3NH_3PbI_3$. The PL was excited with low energy laser pulses at λ_{ex} = 504 nm. (b) Tauc plots of the corresponding thin films.

The stability of obtained blends towards phase segregation was further studied with PL spectroscopy as presented in Figure 53. The specimen containing 0.6 % of EDDI was excited with low energy short laser pulses at 504 nm and the PL intensity at the peak maximum was recorded as a function of time, see Figure 53 (a). Figure 53 (a) shows a stable value of the PL intensity during the measurement of the EDDI/$CH_3NH_3PbI_3$ blend. In addition, the PL spectrum of the specimen was recorded before and after the experiment Figure 53 (b). The spectra did not show any pronounced change of the shape or intensity of the PL peak. This observation confirmed the higher stability of the mixed phase when compared to mixed halide perovskites.

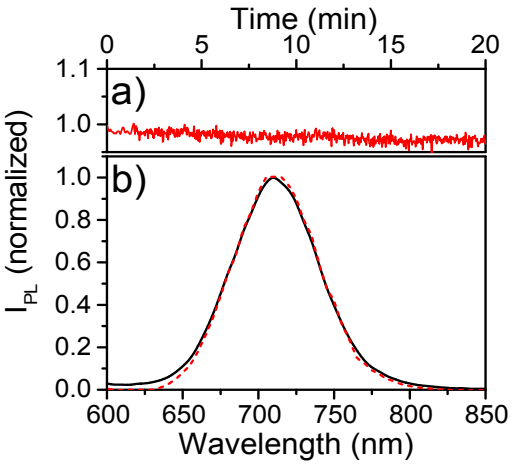

Figure 53 (a) Intensity of the PL peak at 710 nm of the $CH_3NH_3PbI_3$ with 0.6 % of EDDI as a function of time. (b) The PL spectra measured before (black curve) and after (red dashed curve) the time-dependent PL experiment presented in (a). The PL signal was excited with low energy pulsed laser at 504 nm.

The observed changes of the optical properties indicated a strong influence of the additive on the structure of the EDDI/$CH_3NH_3PbI_3$ perovskite blends. Therefore, specimens containing different molar fractions of EDDI were examined by X-ray diffraction. Figure 54 (a) shows the X-ray diffractograms of pure $CH_3NH_3PbI_3$ and of the EDDI/$CH_3NH_3PbI_3$ blends, where the EDDI molar fraction ranging from 0.05 to 0.6 %. Pure $CH_3NH_3PbI_3$ exhibits a peak at 23.45°, the (211) plane, which is a signature reflex of the tetragonal phase with *I4/mcm* symmetry.[124] Adding 0.05 % of EDDI to the $CH_3NH_3PbI_3$ perovskite did not lead to the appearance of new diffraction peaks. Interestingly, independent of the incorporated EDDI content, all samples with different content of EDDI exhibited the main XRD reflexes that are ascribed to the perovskite phase. However, an increase of the EDDI fraction from 0.15 to 0.35 % leads to a dramatic decrease in the intensity of the (211) diffraction peak at 23.45° (Figure 54b). The peak vanishes completely for samples containing 0.5 % of EDDI. The disappearance of the signature (211) peak for the tetragonal phase indicates a phase transition during the crystallization of the sample. Hence, the reflexes of the samples containing 0.5 and 0.6 % of EDDI are assigned to a cubic crystal lattice with *Pm-3m* symmetry.

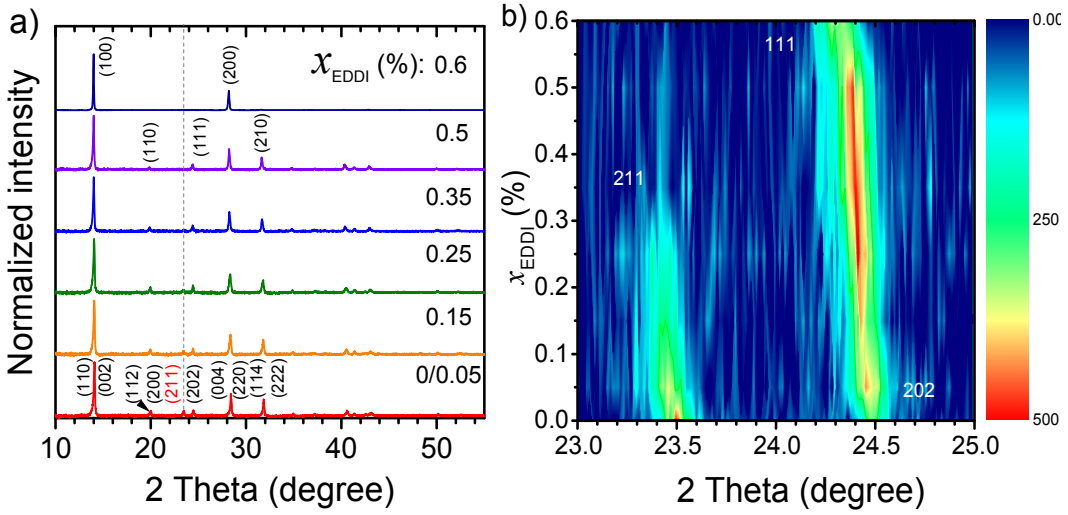

Figure 54. (a) X-ray diffractograms of the thin film of $CH_3NH_3PbI_3$/EDDI blends, where molar fraction of EDDI is x = 0, 0.05, 0.15, 0.25, 0.35, 0.5, and 0.6 %. (b) Contour plot of the intensity of the (211) and (202) diffraction peaks as a function of $x_{(EDDI)}$.

Using Bragg's law, the lattice parameters were calculated from XRD of the blends with different content of EDDI. Figure 55 (a) shows the band gap values obtained from photoluminescence data and from the Tauc plots as a function of the pseudocubic lattice parameter, a. Interestingly, for both methods, a linear dependence of the optical band-gap on a was obtained. However, a small discontinuity of the linear trend was observed at $x_{(EDDI)} > 0.35$ % indicating the phase transition. On the other hand, the dependence of the band gap on $x_{(EDDI)}$ exhibited a linear trend despite the phase transition occurring when $x_{(EDDI)} > 0.35$ % (Figure 55b). Moreover, an increase of the EDDI fraction from 0 to 0.6 % allowed tuning the band gap in a range from 1.6 to 1.79 eV continuously.

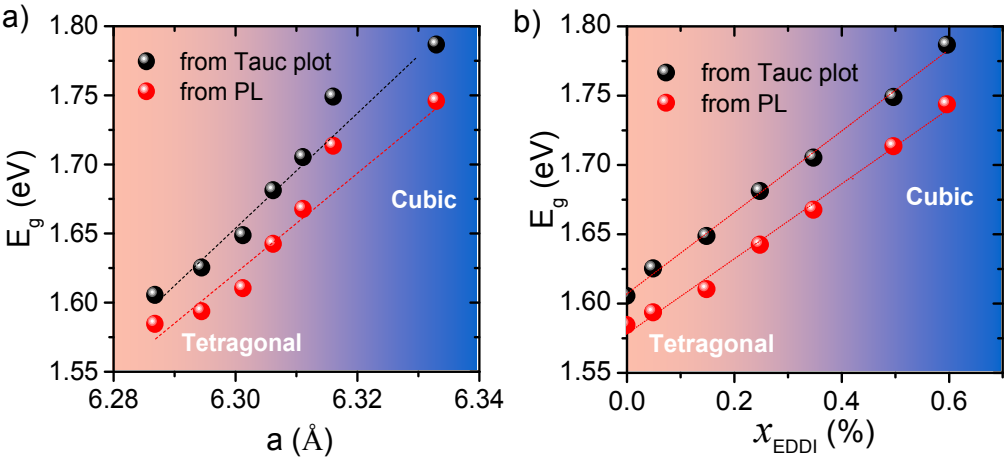

Figure 55. (a) The dependence of the band gap of $CH_3NH_3PbI_3$/EDDI blends on pseudocubic lattice parameter, a. (b) The dependence of the band gap on molar fraction of

EDDI in $CH_3NH_3PbI_3$/EDDI blends. The band gap values were calculated from Tauc plots and PL spectra.

The increase of the lattice parameters and phase transition indicated a possible inclusion of the larger cation in the crystalline lattice of $CH_3NH_3PbI_3$. Since the size of the cation was estimated to be twice of the size of methylammonium, this inclusion should lead to a strain in the material. The position of the diffraction peaks and their FWHM (β) were used for calculation of the strain by the Williamson-Hall method (Figure 56a). The intercept of the least squares fit of the data is indicating the crystalline domain size, while the slope of the fit can be used for calculation of the micro-strain. For a detailed description of the Williamson-Hall method see chapter Experimental techniques (page 29). The slope of the Williamson-Hall plot was determined for all used molar fractions of EDDI and the values are plotted as a function of $x_{(EDDI)}$, see Figure 56 (b). The pristine $CH_3NH_3PbI_3$ has about 0.5 % of strain in the layer. Similarly, the blends with $x_{(EDDI)}$ below 0.25 % did not show a change in the strain. However, the material with 0.25 % of EDDI exhibited a drastic increase of the strain to about 2 %. Further increase of the content of EDDI led to the rise of the strain to about 2.5 % indicating a strong influence of the larger cation on the structure of the material.

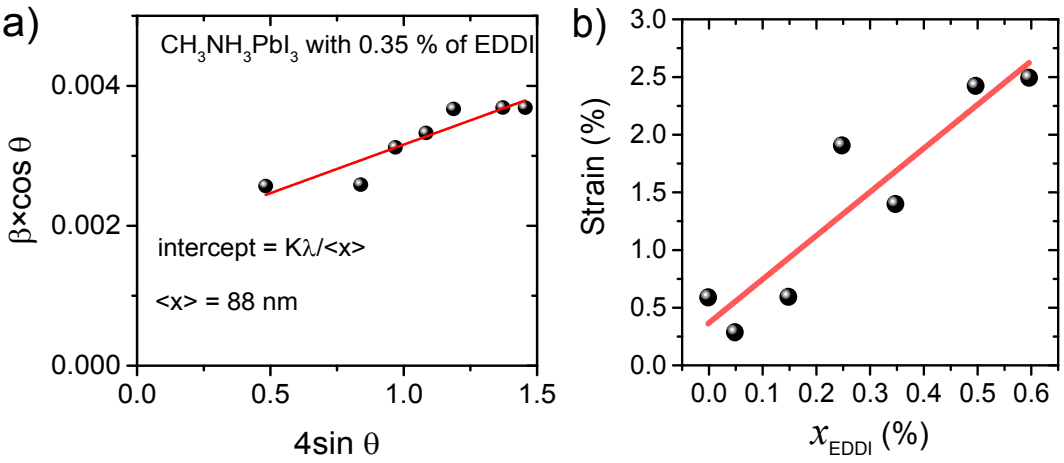

Figure 56. (a) The Williamson-Hall plot of the EDDI/$CH_3NH_3PbI_3$ blend with $x_{(EDDI)}$ = 0.35 %. (b) Strain in the EDDI/$CH_3NH_3PbI_3$ blends as a function of the EDDI molar fraction, $x_{(EDDI)}$. The strain values were calculated from the least-squares fit of the Williamson-Hall plot of the corresponding materials.

The influence of the additive on the microscopic structure of EDDI/$CH_3NH_3PbI_3$ perovskite blends was investigated using scanning electron microscopy (SEM) imaging. In Figure 57, top

view SEM micrographs of specimens with 0 and 0.6 % EDDI are shown. The $CH_3NH_3PbI_3$ perovskite (0 % EDDI) exhibited a homogeneous morphology with an average grain diameter, <x>, of 183 nm. However, when the content of EDDI in EDDI/$CH_3NH_3PbI_3$ blends was increased, the morphology changed drastically. In Figure 57 (e), the grain diameter, <x>, is plotted as a function of the EDDI molar fraction in the perovskite blends. A modest increase of the average grain diameter to 223 nm was observed for samples containing $x_{(EDDI)} < 0.25$ %. However, when the content of EDDI in the films was increased to 0.35 % a pronounced increase of the average grain-size was observed to about 323 nm. A further increase of the EDDI fraction in the perovskite resulted in a monotonous increase of the average grain size. The specimen with $x_{(EDDI)} = 0.6$ % showed the value of <x> ≈ 563 nm. This behavior is a strong indication the influence of the presence of EDDI molecules on the film formation.

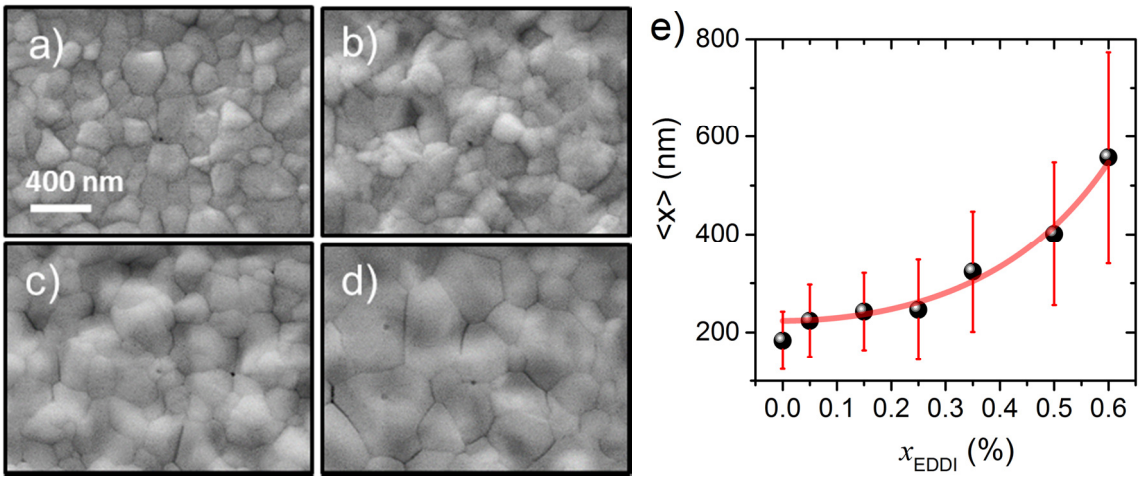

Figure 57. Top view SEM micrographs of the thin films of $CH_3NH_3PbI_3$/EDDI mixed materials, where fraction of EDDI amounted to 0 (a), 0.05 (b), 0.35 (c), and 0.6 % (d). (e) The average grain size as a function of $x_{(EDDI)}$. The error bars represent the standard deviation.

Since the strong influence of EDDI on optical properties and morphology was observed, the dependence of the electrical properties of the EDDI/$CH_3NH_3PbI_3$ blends was investigated using surface photovoltage spectroscopy (SPV). For this purpose samples with different EDDI content were deposited on top of a transparent and conducting indium tin oxide (ITO) substrate. Figure 58 (a) shows the spectral dependence of the photovoltage amplitude of the EDDI/$CH_3NH_3PbI_3$ blends. The photovoltage (PV) amplitude was calculated according to the literature:[128]

$$PV\ amplitude = \sqrt{(x^2 + y^2)} \tag{22}$$

where x is the in-phase and y is the phase-shifted by 90° SPV signals. Interestingly, an increase of the EDDI content resulted in a pronounced reduction of the PV amplitude for photon energies less than 1.55 eV. The specimen containing 0.6 % of EDDI exhibits a PV amplitude that is one order of magnitude lower than that of pure $CH_3NH_3PbI_3$ perovskite. The reduction of the PV amplitude indicates a decrease of the number of defect states in the band gap.[128]

In addition, the increase of the EDDI content led to a change in the PV amplitude for photon energies above 1.6 eV. The addition of 0.05 to 0.15 % of EDDI resulted in a decrease of the PV amplitude. This behavior indicates a reduced charge separation. However, a further increase of the EDDI content to 0.35 % caused a rise of the PV amplitude to the initial value of the pristine material. The specimen with 0.6 % of EDDI exhibits a modest rise of the PV amplitude in comparison to the pristine material. This behavior is indicative of a modest increase of the charge extraction with the increase of the EDDI content.

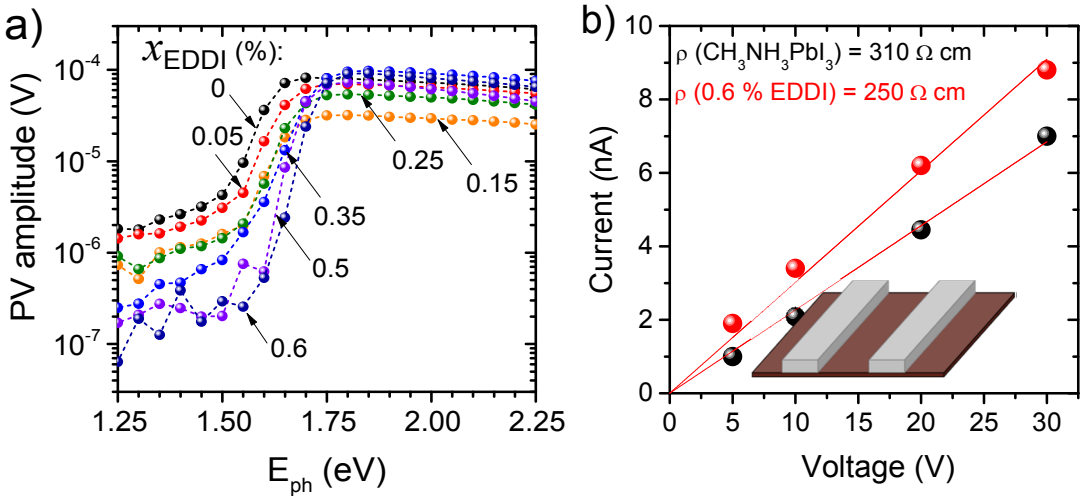

Figure 58. (a) The surface photovoltage amplitude of the thin films containing from 0 to 0.6 % of EDDI as a function of photon energy. (b) The dependence of the current on applied voltage of the specimen with 0.6 % of EDDI and pristine $CH_3NH_3PbI_3$.

To elaborate further on electronic properties of EDDI/$CH_3NH_3PbI_3$ blends, current-voltage characteristics of the thin films were measured. The inset of Figure 58 (b) depicts a schematic representation of the conductance measurements, where different voltage values were applied between two metal contacts deposited on top of a film. The dependence of the current on the applied voltage is plotted in Figure 58 (b) for the pristine $CH_3NH_3PbI_3$ and the EDDI/$CH_3NH_3PbI_3$ blend with 0.6 % of EDDI. The linear fit of the obtained data was used for calculating the resistance values of the material. The resistance, ρ, of the thin film of pristine

$CH_3NH_3PbI_3$ amounted to about 310 Ωcm. Interestingly, the specimen containing 0.6 % of EDDI exhibited a lower value of ρ = 250 Ωcm indicating an improvement of the conductivity of the EDDI/$CH_3NH_3PbI_3$ blend in comparison to $CH_3NH_3PbI_3$.

Consequently, this enhancement in conductivity was tested for use in solar cells and is compared to the standard $CH_3NH_3PbI_3$ solar cells. Figure 59 (a) shows the IV characteristics of two solar cells, where one absorber layer consisted of pristine $CH_3NH_3PbI_3$ and the other – the EDDI/$CH_3NH_3PbI_3$ blend with 0.6 % of EDDI. The inverted architecture solar cells were used comprising of the following layers: ITO/PEDOT:PSS/Perovskite/PCBM/BCP/Ag as depicted in the inset. The measurements were performed in the dark and under AM 1.5 G illumination. The open and closed symbols indicate a scan in the forward and reverse bias direction, respectively. The device with the pristine $CH_3NH_3PbI_3$ perovskite absorber exhibits a short circuit current of J_{sc} = 20.2 mA/cm^2, a fill factor (*FF*) of 62 %, and an open circuit voltage of V_{oc} = 0.82 V. This resulted in a power conversion efficiency of η = 10.3 %. Adding 0.6 % of EDDI in the absorber layer resulted in a drastic decrease of J_{sc} to 11.47 mA/cm^2, while the open circuit voltage and the fill factor increases significantly to V_{oc} = 1.07 V and FF = 71 %. Consequently, the solar cell containing 0.6 % of EDDI reached an efficiency of η = 8.7 %.

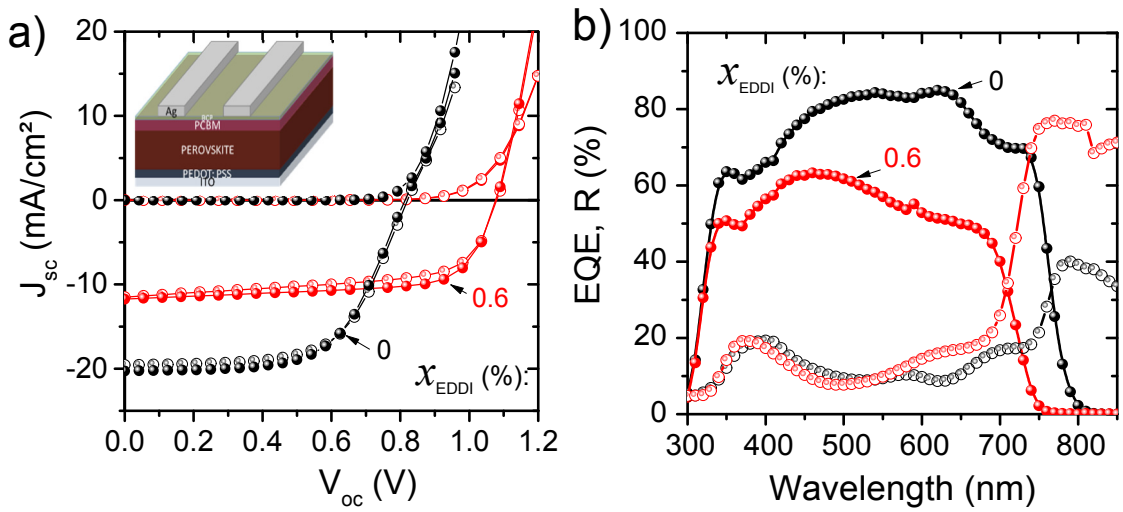

Figure 59. (a) The current-voltage characteristics of the solar cells, where the absorber material consisted of the pristine $CH_3NH_3PbI_3$ (0 %) and $CH_3NH_3PbI_3$ blended with 0.6 % of EDDI. (b) External quantum efficiency and reflectance spectra of the corresponding devices.

Figure 59 (b) depicts the external quantum efficiency (EQE) and the reflectance (R) of the same devices as used for solar cell measurements. The reflectance and EQE spectra exhibit a pronounced shift of the band gap to 1.75 eV of the specimen containing 0.6 % of EDDI. In

addition, the drastic decrease of EQE is correlated with the reduction in J_{sc} of the specimen with the larger band gap. The values of the photovoltaic performance of the solar cells containing different amounts of EDDI are summarized in Table 2.

Table 2. The parameters of the solar cells with 0, 0.05, 0.15, 0.25, 0.35, 0.5, and 0.6 % of EDDI under AM 1.5 G solar illumination.

$x_{(EDDI)}$ (%)	η (%)	J_{SC} (mA/cm²)	V_{OC} (V)	*FF* (%)
0	10.1	20.2	0.81	62
0.05	8.17	17.07	0.85	56
0.15	8.01	15.43	0.86	59
0.25	7.95	14.64	0.90	60
0.35	6.92	13.07	0.95	56
0.5	7.99	11.75	0.98	69
0.6	8.71	11.47	1.07	71

Stabilization of the α-phase of $CsPbI_3$ by addition of ethylenediammonium diiodide (EDDI)

Since the addition of ethylenediammonium diiodide to $CH_3NH_3PbI_3$ led to a strong alteration of the optical and electronic properties, the influence of ethylenediammonium diiodide (EDDI or $C_2H_4(NH_3I)_2$) on the properties of $CsPbI_3$ was studied. Figure 60 shows photographs (a) and SEM images (b) of the surface of layers formed by the one-step spin-coating of $CsPbI_3$ and $CsPbI_3$/EDDI blends with molar fraction of EDDI, $x_{(EDDI)}$ = 0.25, 0.5, and 1 %. The photograph of the sample containing pristine $CsPbI_3$ exhibited a pale yellow color of the δ-phase appearing upon cooling of the film. An addition of 0.25 % of EDDI led to a partial appearance of the α-phase or "black" phase. The area of the black phase was increased when the content of EDDI was increased to 0.5 %. A fully converted to the black phase thin film was obtained by the addition of 1 % of EDDI.

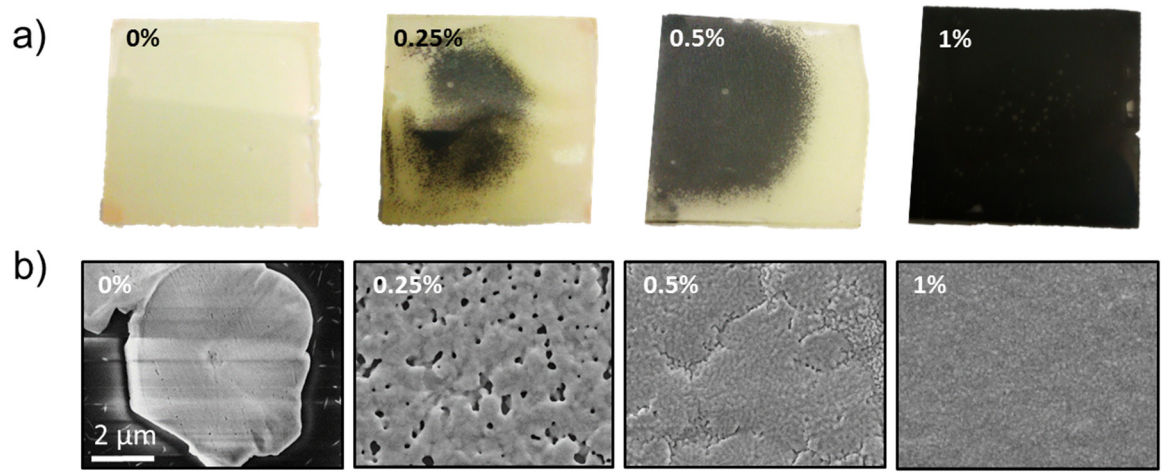

Figure 60. (a) Photographs of the thin films of pristine $CsPbI_3$ (0 %) and $CsPbI_3$ blended $x_{(EDDI)}$ = 0.25, 0.5, and 1 %. (b) Top view SEM micrographs of the corresponding thin films.

The top view SEM micrographs show the microscopic structure of the $CsPbI_3$ and $CsPbI_3$/EDDI in more detail, see Figure 60 (b). The thin film of pristine $CsPbI_3$ exhibited a non-uniform morphology with micrometer-sized islands. The material with 0.25 % of EDDI showed a strong improvement in coverage of the substrate surface but exhibited a great number of holes. Further increase of the content of EDDI up to 1 % resulted in a formation of fully covered and uniform thin films with grain sizes of about 100 nm.

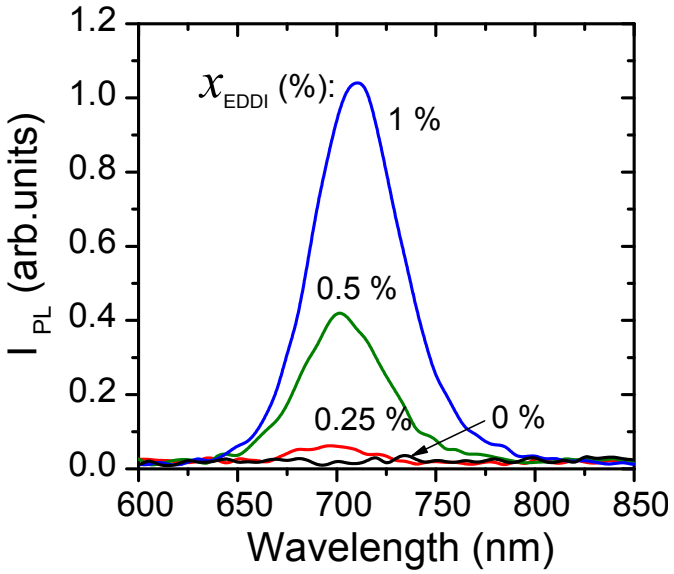

Figure 61. Photoluminescence spectra of thin films of $CsPbI_3$/EDDI blends where molar fraction of EDDI amounted to 0, 0.25, 0.5, and 1 %, respectively.

Since specimens of $CsPbI_3$ containing EDDI exhibited an appearance of the "black phase", the optical properties of the specimens were studied with photoluminescence spectroscopy. Figure 61 shows the PL spectra of $CsPbI_3$ without (0%) and with 0.25, 0.5, and 1 % of EDDI. As expected, pristine $CsPbI_3$ in the δ- phase (0 %) showed no optical response in the range of interest. However, layers containing 0.25 % of EDDI exhibited a weak PL signal at about 700 nm. The intensity of this PL peak was increased when 0.5 % of EDDI was added. The specimen with 1 % of EDDI exhibited a pronounced PL peak with a maximum slightly shifted to 710 nm (1.75 eV) that corresponds to the band gap of pure $CsPbI_3$ in the α-phase.

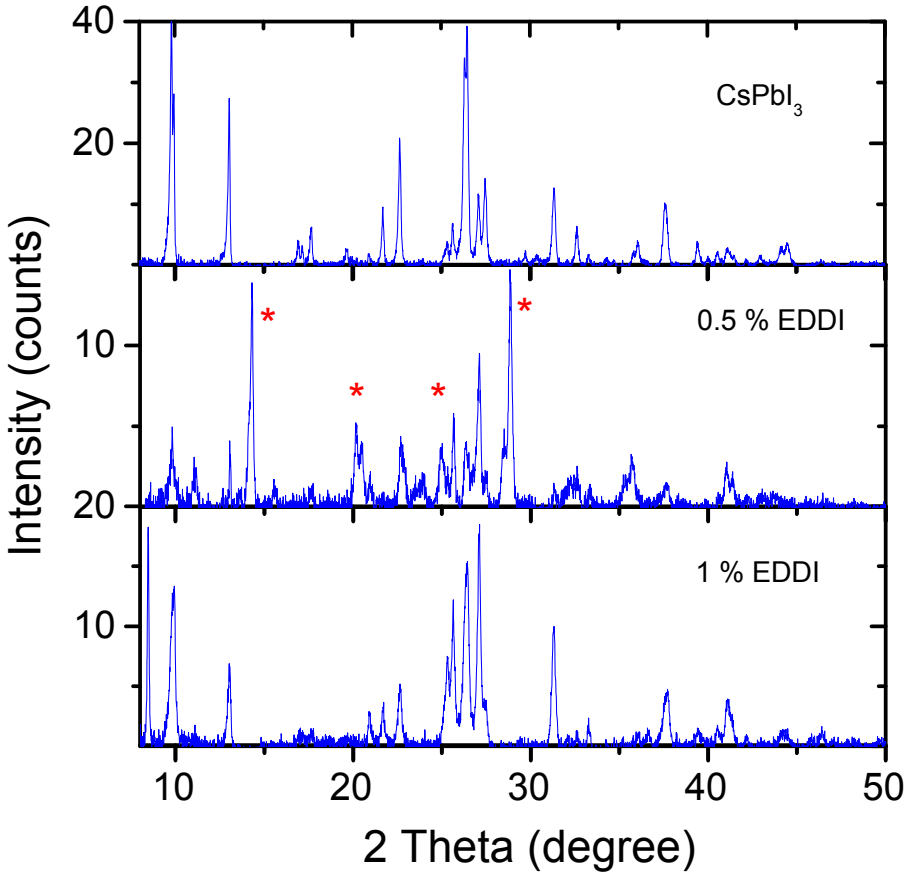

Figure 62. X-ray diffractograms of the pristine $CsPbI_3$ and $CsPbI_3$/EDDI blend containing 0.5 and 1 % of EDDI. Reflexes assigned to the cubic structure of the α-phase are marked by red asterisks.

The structure of the $CsPbI_3$/EDDI blends was studied with X-ray diffraction method (Figure 62). The XRD of pristine $CsPbI_3$ corresponds to the orthorhombic δ-phase which is in good agreement with literature.[83] Addition of 0.5 % of EDDI to $CsPbI_3$ led to a partial phase transition from orthorhombic to the cubic structure as visualized by the appearance of intense reflexes at 14.2 and 27.8°. At the same time, the diffractogram of the 0.5 % specimen showed a splitting of the reflexes. The splitting often occurs as a result of lowering the symmetry or the formation of low dimensional structures. The increase of the content of EDDI to 1 % led to the further splitting of the reflexes and an appearance of the diffraction peak at 8°. This behavior is consistent with the formation of a low dimensional material.

4.2.3. Photostability of hybrid perovskites

In this chapter, the influence of light on hybrid perovskites was investigated by means of *in-situ* FT-IR spectroscopy. Thin films of $CH_3NH_3PbI_3$ were illuminated with UV-LED with a photon energy of hν = 3.4 eV. Figure 63 (a) shows the FT-IR spectra of the as-prepared $CH_3NH_3PbI_3$ thin film (black curve) and after illumination for 410 min in vacuum (red curve). The graph depicts asymmetric and symmetric stretching N-H vibrations of $CH_3NH_3^+$ cation. To elucidate the change of the material induced by light, the spectrum taken after illumination was normalized to the spectrum of the as-prepared specimen. Figure 63 (d) shows a divided spectrum of the material. The signal pointing upwards indicates a decrease of the intensity of the vibrations after illumination in comparison to the as-prepared. Clearly, this observation occurs as a result of a loss of the N - H bonds vibrating at 3150 cm^{-1}.

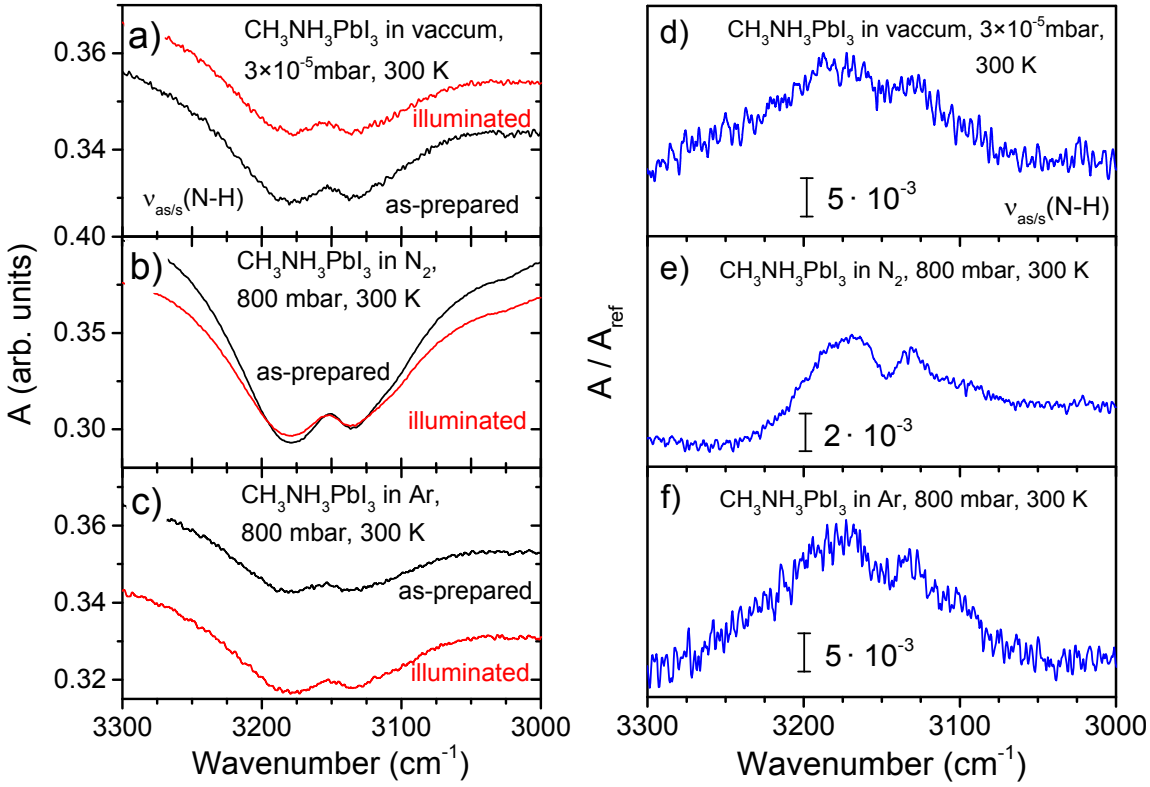

Figure 63. (a) FT-IR spectra of the as-prepared $CH_3NH_3PbI_3$ layer and after illumination with a photon energy of hν = 3.4 eV for 410 min in vacuum. The graph depicts N-H asymmetric and symmetric stretching vibrations. (b) FT-IR spectra of the as-prepared $CH_3NH_3PbI_3$ layer and after illumination with photon energy of hν = 3.4 eV for 120 min in 800 mbar N_2 atmosphere. (c) FT-IR spectra of the as-prepared $CH_3NH_3PbI_3$ layer and after illumination with a photon energy of hν = 3.4 eV for 120 min in 800 mbar Ar atmosphere. (d), (e), and (f) corresponds to FT-IR spectra of the $CH_3NH_3PbI_3$ layer after illumination normalized to as-prepared $CH_3NH_3PbI_3$ layer in vacuum, N_2, and Ar, respectively.

Previous reports have indicated a possible loss of CH_3NH_3I due to the influence of vacuum and out-diffusion of methylammonium from a sample (Chapter 2, page 23). Therefore, for clarity of experiment, it is necessary to separate the influence of the atmosphere and light. Since hybrid perovskites are processed and handled most commonly in a nitrogen atmosphere, similar experiments were conducted in nitrogen and argon. Figure 63 (b, c) shows the FT-IR spectra of the as-prepared and after illumination $CH_3NH_3PbI_3$ thin film in nitrogen and argon atmosphere. The difference spectra of the corresponding films in nitrogen and argon are shown in Figure 63 (e, f) respectively. Remarkably, the appearance of the peaks pointing upwards at about 3150 cm^{-1} indicates the loss of N-H bonds, similarly to the measurements in vacuum. This behavior reveals a common mechanism of the light-induced degradation of $CH_3NH_3PbI_3$ independent on testing conditions.

To obtain a full picture of changes occurring in the material after illumination, the thin films of $CH_3NH_3PbI_3$ were also investigated with FT-IR at low temperatures. Cooling down to cryogenic temperatures leads to an extreme sharpening of the peaks and allows to analyze discrete vibrations, which are usually indistinguishable at room temperature. In addition, low-temperature measurements strongly reduce the probability of out-diffusion of any species from the specimen. Figure 64 (a) shows the FT-IR spectra of as-prepared $CH_3NH_3PbI_3$ thin film and after illumination with $h\nu = 2.7$ eV at 10 K. The graph depicts the range of the CH_x and NH_x vibrations, where change in the vibration intensity was observed. Similarly to the room temperature measurements, the loss of N - H vibrations was observed at 3078, 3122, and 3172 cm^{-1}. In addition, change of the vibration intensity was detected at 1586, 1454, 1451, and 1419 cm^{-1} corresponding to bending vibrations of N-H and C-H bonds. This change of the intensity indicates the loss of the N-H and, possibly C-H bonds, even at low temperatures. As a result, this observation further confirmed the light-induced origin of the decomposition of $CH_3NH_3PbI_3$. In addition, it suggests that the bond dissociation process does not need to overcome any additional temperature barrier.

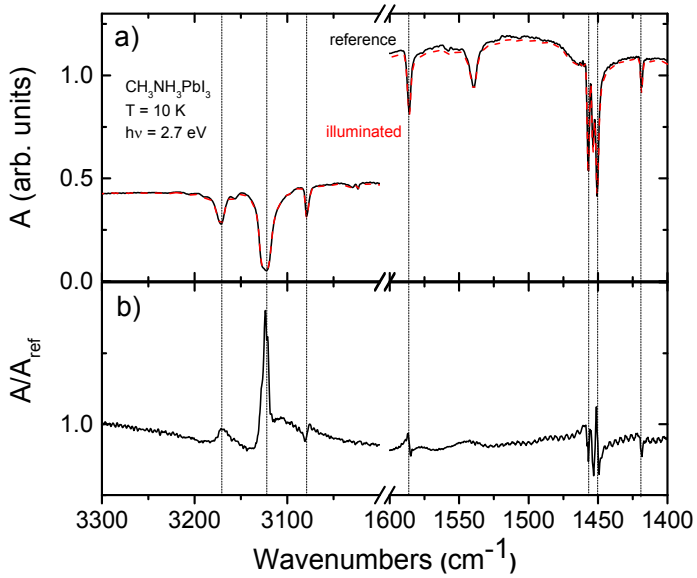

Figure 64. (a) FT-IR spectra of the as-prepared $CH_3NH_3PbI_3$ layer and after illumination with a photon energy of hν = 2.7 eV for 120 min at 10 K. (b) FTIR spectrum of the layer of $CH_3NH_3PbI_3$ after illumination normalized to the as-prepared $CH_3NH_3PbI_3$ layer.

Previous reports have shown a superior stability of formamidinium lead perovskite ($CH(NH_2)_2PbI_3$ or $FAPbI_3$) and mixed cation perovskites, which demonstrate similar to $CH_3NH_3PbI_3$ optical and electronic properties. Therefore, the influence of light on $FAPbI_3$ was investigated, in the similar way as for $CH_3NH_3PbI_3$. The thin film of $FAPbI_3$ was illuminated with UV-LED with a photon energy of hν = 3.4 eV. Figure 65 (a) shows the FT-IR spectra of as-prepared $FAPbI_3$ thin film and after illumination for 270 min in vacuum at room temperature. The graph shows N-H and C-N symmetric stretching vibrations of the formamidinium cation, $CH(NH_2)_2^+$. The spectrum after illumination was normalized to the spectrum of the as-prepared material to indicate the relative change of the vibration intensity. Similarly to methylammonium-based perovskite, a decrease of the intensity of N-H stretching vibrations was observed at about 3400 and 3350 cm^{-1} indicating a loss of N-H bonds (Figure 65b). Additionally, a loss of C-N bonds was observed at 1710 cm^{-1} indicating a complete fractioning of the $CH(NH_2)_2^+$ cation.

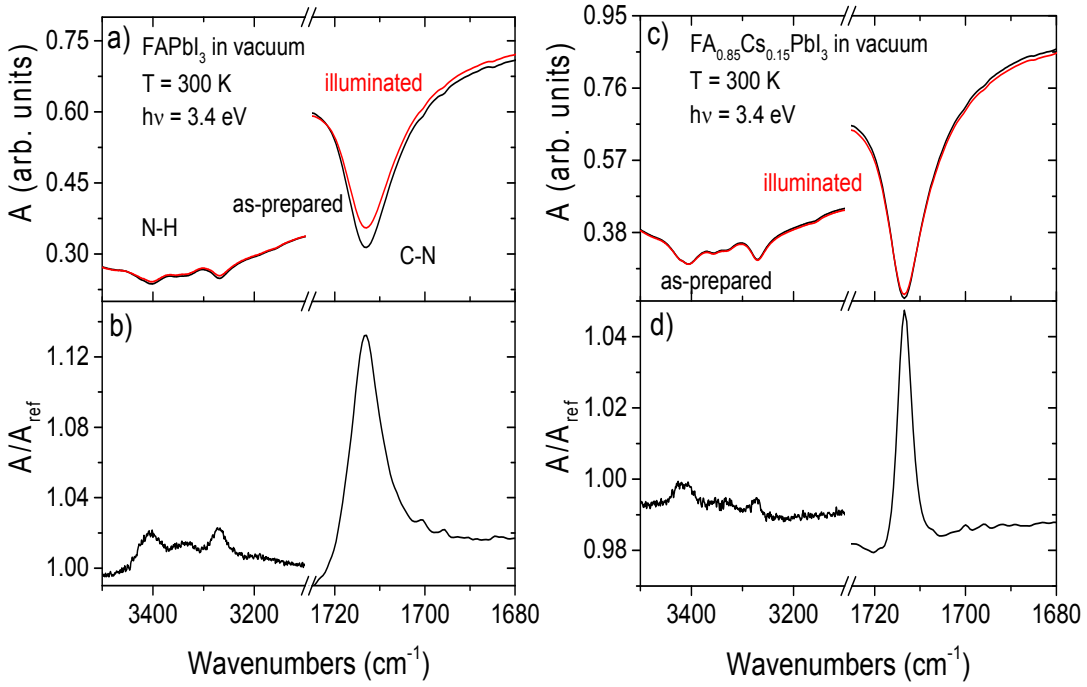

Figure 65. (a) FT-IR spectra of the as-prepared $FAPbI_3$ layer and after illumination with photon energy of hν = 3.4 eV for 270 min in vacuum. The graph depicts N-H asymmetric and symmetric stretching vibrations and C-N. (b) FT-IR spectra of the layer of $FAPbI_3$ after illumination normalized to as-prepared $FAPbI_3$ layer. (c) FT-IR spectra of as-prepared $FA_{0.85}Cs_{0.15}PbI_3$ layer and after illumination for 140 min with hν = 3.4 eV in vacuum. (d) FT-IR spectra of the layer of $FA_{0.85}Cs_{0.15}PbI_3$ after illumination normalized to the as-prepared layer.

Since both most commonly used organic cations exhibited a rather swift decomposition under illumination, the influence of an inorganic cation on the stability of the material was investigated. The mixed cation $FA_{0.85}Cs_{0.15}PbI_3$ perovskite has shown a drastic improvement of the thermal stability, device performance and device stability.[31] Figure 65 (c) shows the FT-IR spectra of as-prepared $FA_{0.85}Cs_{0.15}PbI_3$ thin film and after illumination for 140 min with hν = 3.4 eV in vacuum at room temperature. Intriguingly, the FT-IR spectrum of the material containing Cs did not show any influence on the vibration position in comparison to pure $FAPbI_3$. The normalized spectrum after illumination exhibited a reduction of the vibration intensity of both N-H and C-N bonds similarly to pristine $FAPbI_3$ as presented in Figure 65 (a, b). This behavior demonstrates identical to the pure predecessors the light-induced degradation of the mixed cation perovskites.

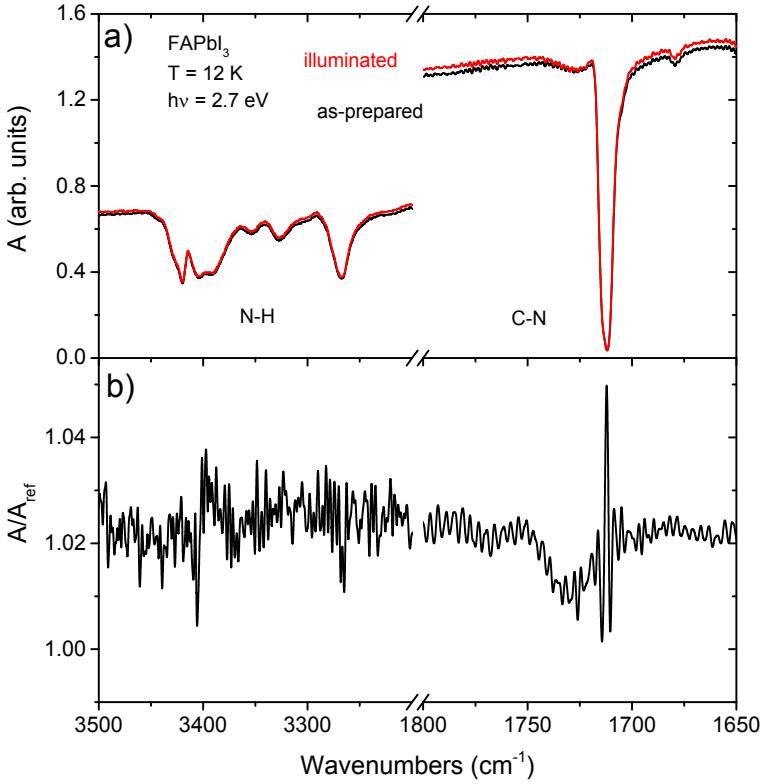

Figure 66. (a) FT-IR spectra of as-prepared $FAPbI_3$ layer and after illumination with photon energy of hν = 2.7 eV for 410 min, T = 12 K. The graph depicts the N-H asymmetric and symmetric stretching vibrations and the C-N stretching vibration. (b) FT-IR spectra of the layer of $FAPbI_3$ after illumination normalized to the spectrum of the as-prepared $FAPbI_3$ layer.

Additionally, the influence of light on $FAPbI_3$ was investigated at low temperature. The FT-IR spectra of the $FAPbI_3$ thin films before and after illumination with hν = 2.7 eV at 12 K are presented in Figure 66 (a). The normalized spectrum is depicted in Figure 66 (b). The pronounced decrease of the C-N and N-H vibrations was observed after illumination. Similarly to the low-temperature $CH_3NH_3PbI_3$ measurements, this behavior indicates an absence of a thermal barrier for the fracture of the organic cation and similar light-induced mechanism of the decomposition process.

To investigate this decomposition process in more detail, $CH_3NH_3PbI_3$ and PbI_2 thin films were studied by means of absorption spectroscopy.

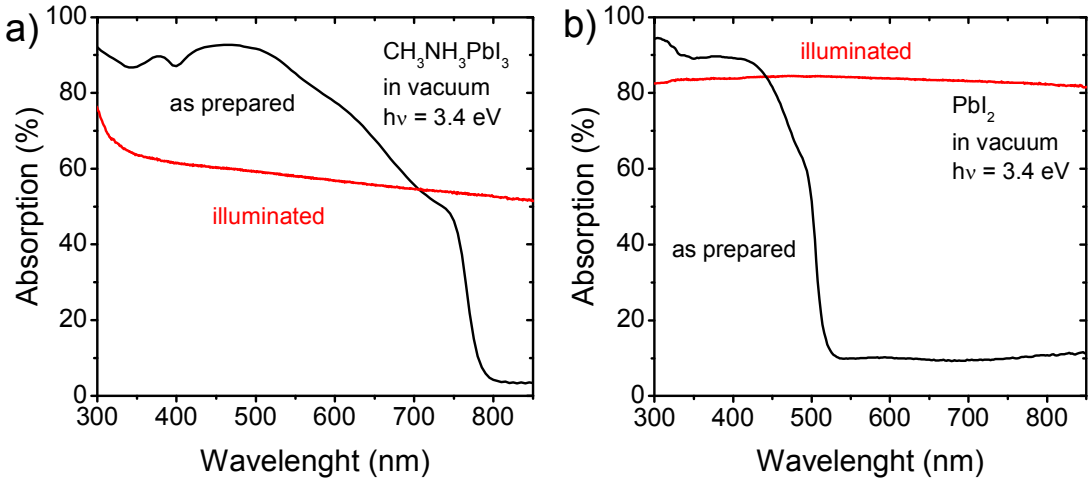

Figure 67. (a) Absorption spectra of as-prepared thin film of $CH_3NH_3PbI_3$ and after illumination in vacuum with hν = 3.4 eV. (b) Absorption spectra of the lead iodide thin film before and after illumination in vacuum with hν = 3.4 eV.

Figure 67 (a) depicts absorption spectra of the thin film of $CH_3NH_3PbI_3$ before and after illumination in vacuum with hν = 3.4 eV. The as-prepared film exhibited an absorption onset at about 780 nm corresponding to the band gap of 1.59 eV, which is similar to that reported in literature.[32] The specimen after 24 h of illumination in vacuum exhibited a black coloring, however, showed no absorption in the visible spectral range. Similarly, thin films of pristine lead iodide were investigated. Figure 67 (b) shows absorption spectra of PbI_2 before and after illumination in vacuum. The absorption onset of the as-prepared layer amounted to about 500 nm, which is in a good agreement with literature.[114] Unexpectedly, the illumination in vacuum for 24 h led to a drastic change of the color of the PbI_2 layer from bright yellow to black. In addition, the film showed an extremely low transmission and an absence of absorption features in the visible range similarly to what observed in $CH_3NH_3PbI_3$ after illumination (Figure 67a).

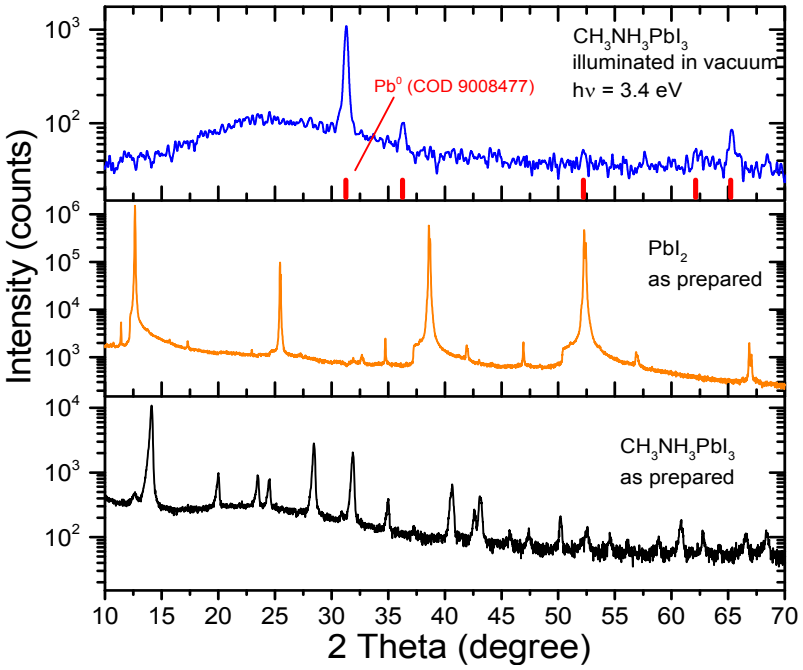

Figure 68. X-ray diffractograms of as-prepared $CH_3NH_3PbI_3$ and as-prepared thin film of PbI_2 in comparison to the X-ray diffractogram of the illuminated $CH_3NH_3PbI_3$ in vacuum with hν = 3.4 eV. The calculated reference data corresponds to Pb^0 according to literature. [129]

The thin film of $CH_3NH_3PbI_3$ after 24 h of illumination with hν = 3.4 eV in vacuum was investigated with X-ray diffraction method. Figure 68 shows x-ray diffractograms of the illuminated specimen in comparison to the as-prepared thin films of $CH_3NH_3PbI_3$ and pure PbI_2. The diffractogram of the degraded specimen exhibited disappearance of the reflexes corresponding to the perovskite phase. Moreover, the XRD patterns of the illuminated specimen were inconsistent with reflexes of PbI_2. Further analysis of the diffractogram revealed a strong match of the XRD pattern of the illuminated material with Pb^0. The reference data for x-ray diffraction patterns of Pb^0 were taken from literature.[129] This observation indicates further dissociation of PbI_2 to Pb^0 under prolonged illumination.

5. Discussion

This chapter provides the discussion of the result obtained within this thesis. It contains a brief review of the most relevant literature required for support and understanding of the key findings. Moreover, this chapter includes necessary models and visual aids for better perception of the results.

Solvation and complexation of perovskite precursors

The properties of hybrid perovskites depend on many parameters including solvent choice, temperature and time of annealing. However, it is conceivable that the properties of the resulting material might be already determined in the solution. Commonly, aprotic polar solvents are used for the preparation of the precursor solution. Among others, dimethyl sulfoxide (DMSO), dimethylformamide (DMF), gamma-butyrolactone (GBL), N-methyl-2-pyrrolidone (NMP) and their mixtures are reported most frequently. Despite the limited number of solvents appropriate for the task, the role of the medium is not clear. Several reports addressed an issue of an interaction of the material with solvent molecules leading to the formation of complex structures of metal halides and solvent. The report by N. J. Jeon and N. Ahn indicated the occurrence of particularly strong complexes of lead iodide with DMSO.[111,130] Both studies suggested the use of such complexes as an intermediate phase for the preparation of perovskites. On the other hand, studies performed by J. S. Manser and R. J. Stewart indicate the formation of not only complexes of lead iodide with solvent but also the formation of polyiodide plumbate complexes.[118,131] Moreover, the study by S. J. Yoon claimed that the chemistry of such polyiodide plumbates dictates chemistry of hybrid perovskites.[119] According to this study, the lead iodide molecules form complexes with solvent, where each PbI_2 molecule is surrounded by 4 additional solvent molecules following the coordination number of 6. In presence of another source of iodine ions, such as CH_3NH_3I or KI, the solvent molecules are exchanged by I^-. The process occurs stepwise and lead iodide forms several complexes with a different stoichiometry: PbI_2S_4, $PbI_3^{1-}S_3$, $PbI_4^{2-}S_2$, where S corresponds to a solvent (Figure 69).

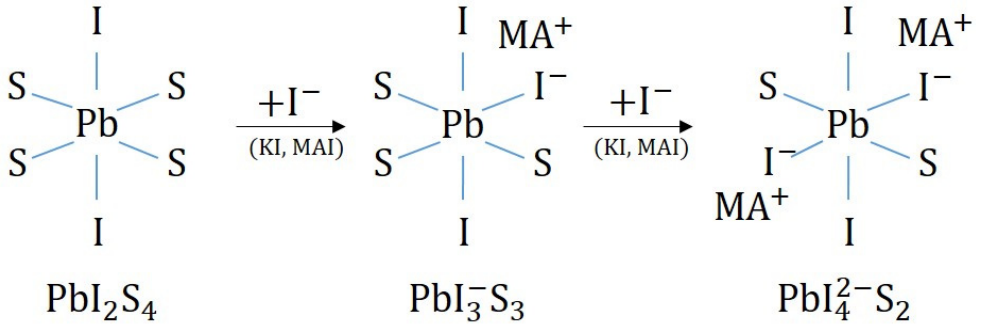

Figure 69. Different stages of the interaction between PbI_2 and a generic solvent (S) and formation of polyiodide plumbate complexes.

These complexes form a colloidal solution which is an intermediate phase for the formation of solid perovskite material. The same species were reported simultaneously by

S. Rahimnejad.[132] The work by Y. Guo et al. reported that a prerequisite for the formation of these species is the formation of polyiodide plumbate chain-like complexes of $(PbI_4S_2)_n$ (Figure 70).[120] The data presented in this thesis clearly indicates that observed species of polyiodide plumbates are present already in the solution of lead iodide (Figure 31, Chapter 4.1). Therefore, the previously reported absorption bands should correspond to a formation of polymeric lead iodide chains. Nevertheless, the PL study showed that the optical properties of the solution of PbI_2 and $CH_3NH_3PbI_3$ are similar. Moreover, the appearance of the photoluminescence peak at 760 nm in PbI_2 solution suggests a common origin of the excited states in polyiodide plumbates and hybrid perovskites. The position of the emission peak of the PbI_2 solution was independent of the solvent and presence of CH_3NH_3I. Thus, it is plausible that the solvent or the organic cation does not participate in the formation of the excited state in perovskite. This assumption is in good agreement with the band structure of hybrid perovskites, where valence and conduction bands are formed by the inorganic components (Chapter 2.2.2, Figure 4).

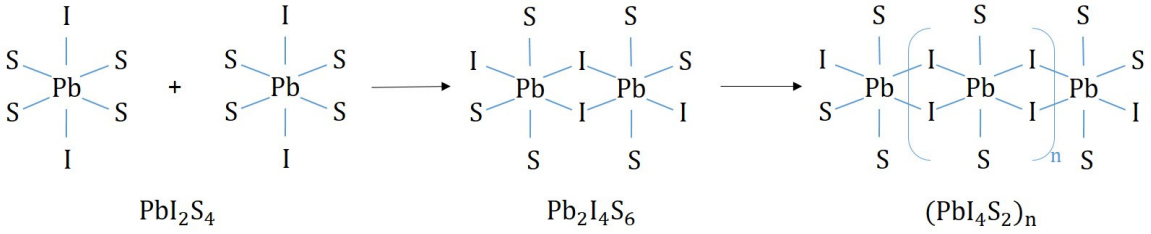

Figure 70. Schematic representation of the formation of polyiodide plumbate chains.

On the other hand, the presented data clearly indicated an influence of solvent on the position of the emission peak of the formed perovskite material and on the intensity of the emission peak of the precursor solution (Figure 30, Figure 32). Therefore, it is conceivable that the solvent molecules form a solvate shell and act as a stabilizer for the polyiodide plumbate clusters. Then, the solvent molecule exchanges for the iodide ions donated by methylammonium iodide. This exchange leads to the formation of oriented perovskite precursor clusters, which then form the bulk of the material during drying. However, the strong interaction of the solvent molecules with polyiodide plumbates suggests that the solvent molecules can reside within the material even after annealing without exchange for CH_3NH_3I. This leads to the formation of iodine vacancies or to the presence of solvent impurities, which both can then act as point defects. As a result, emission from these defects results in broadening and shift of the emission of perovskite thin films.

Stability of hybrid perovskites

Thermal stability: Influence of temperature on properties of $CH_3NH_3PbI_3$

The influence of temperature on properties of hybrid perovskites was reported vastly through the literature. Among different effects of the thermal annealing, it is possible to distinguish two types resulting in decomposition or changes in morphology.[53,133] Despite numerous reports showing data on thermal stability, the precise decomposition temperature and its origin are unknown. Reported values for the degradation temperature of methylammonium lead iodide are ranging from 60 °C to almost 300 °C.[45,53,133–135] Typically, degradation occurs in a conjunction with losses of CH_3NH_3I and, hence, non-stoichiometric composition. Therefore, the resulting material exhibits an excess of PbI_2, which is an indicator for the degraded perovskite. The work by Z. Song et al. showed a rate dependent study of the degradation of methylammonium lead iodide at different temperatures.[123] Specifically, authors find that the loss of the CH_3NH_3I material starts at about 150 °C with a loss rate of 0.002 %/min. The loss at this temperature occurs due to the phase transition of CH_3NH_3I to the ionic plastic phase.[136] This phase transition is followed by the evaporation of CH_3NH_3I at 190 °C leading to a vast decomposition of the perovskite material. This finding was further confirmed in this thesis indicating the decomposition of the material at $T > 190$ °C. However, it was shown that the material can be operated in a broad range of temperatures $T < 190$ °C without decomposition (Figure 38, Chapter 4.2.1).

Interestingly, the material treated at temperatures 190 °C $> T_s >$ 150 °C undergoes drastic changes of the microscopic structure and exhibits an improvement of the optical and electronic properties. Such thermally activated change in morphology is often observed in other semiconducting materials like Si and Ge and ceramics, e.g. $CaTiO_3$.[137,138] The change of properties of materials occurred due to secondary grain growth at elevated temperatures. Secondary grain growth is an activated process of a grain growth. In contrast to normal grain growth, secondary grain growth has two stages.[139] First stage can be presented as an activation of the growth of certain energetically favorable grains, i.e. abnormal grains (Figure 71a, b). The increase of the thermal energy induces the growth of all grains, but the abnormal grains are growing at a larger rate. The signature of such growth mechanism is a bimodal grain size distribution which can be observed due to different growth kinetics (Figure 71b). The growth occurs as a result of the merging of smaller grains with abnormal ones and the redistribution of the material within a formed abnormal grain. The growth continues until all small grains are

annihilated and abnormal grains are impinged. As a result, the material after growth shows an increased average grain size (Figure 71c).

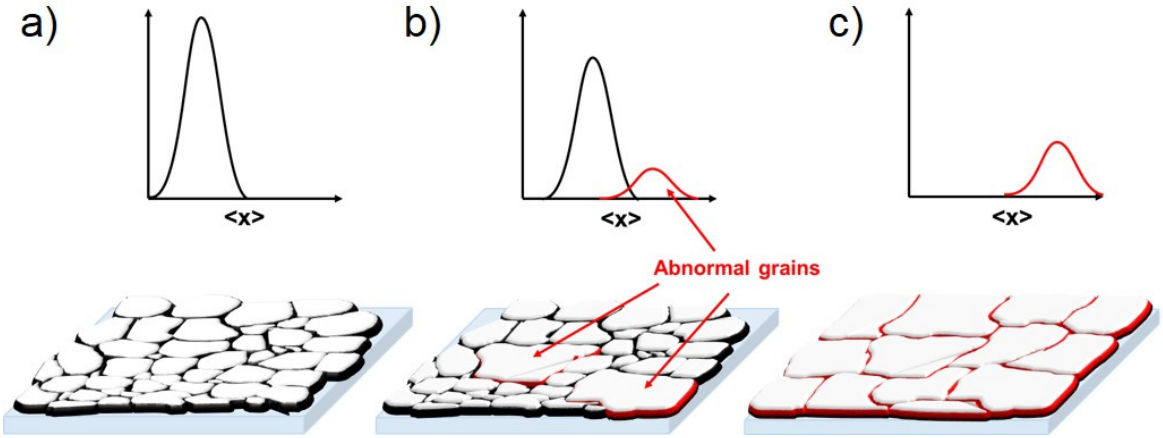

Figure 71. Schematic representation of secondary grain growth: a) initial thin film, b) formation of abnormal grains, c) resulting thin film, where all normal grains are annihilated.

The growth of the abnormal grains is induced by the minimization of the surface energy or the energy of the grain boundary.[140] In the bulk material, the growth of abnormal grains is driven by the energy of the grain boundaries. The high energy of the grain boundary occurs due to the difference in energy of atoms which reside at the opposite sides of the boundary. As a result, the growth leads to a minimization of the boundary area, i.e. boundary energy. In thin films, the growth is driven by the surface energy which shows an inverse dependence on the film thickness.[141]

For many materials, the secondary grain growth shows an activated behavior which is related to the activation energy of self-diffusion. Thus, secondary grain growth can be depicted as a migration of the grain boundary induced by the diffusion of species at an applied external force. The activation energy of the growth, thus, is related to the activation energy of the diffusion of the species. For example, silicon exhibits an activation energy of secondary grain growth in the same range as the activation energy of the self-diffusion of about 4.1 – 5.1 eV.[142] Moreover, many reports have shown that the activation energy of the growth depends strongly on the composition of a material. The presence of dopants and /or impurities results in a dramatic reduction of the self-diffusion energy and, therefore, a reduction of the activation energy of secondary grain growth.[143,144]

In hybrid perovskites, the activation energy of secondary grain growth was calculated according to the Arrhenius law (Figure 42). The activation energy of grain growth in

$CH_3NH_3PbI_3$ amounted to 0.16 eV. This small value of the activation energy indicates that the barrier for the self-diffusion of the species in $CH_3NH_3PbI_3$ is rather low and is consistent with the low decomposition temperature.

Compositional stability of hybrid perovskites: Phase segregation in mixed halide $CsPb(I_{1-x}Br_x)_3$ perovskite

Hybrid perovskites have demonstrated a remarkable dependence of a band gap on a composition of a material. Methylammonium lead halide perovskites with different halide ions, e.g. I, Br, and Cl exhibited values of the band gap amounted to 1.55, 2.3, and 3.1 eV, respectively. Interestingly, mixing different halides within one material leads to a material with intermediate values of the band gap (Figure 11, Chapter 2). The values of the band gap can be estimated according to Vegard's law that is often used for the prediction of the properties of alloyed materials (see Page 19). For example, increasing the amount of Br $0 < x < 1$ in $CH_3NH_3Pb(I_{1-x}Br_x)_3$ allows tuning the band gap from 1.55 to 2.3 eV. However, the materials containing high amount of Br exhibited a pronounced phase-instability under illumination. Specifically, thin films of $CH_3NH_3Pb(I_{1-x}Br_x)_3$ where $0.3 < x < 1$ showed an appearance of new low energy phases at about 1.7 eV under illumination.[74,75] The new phase occurred as a result of the photo-induced phase segregation of the mixed material into iodide-rich and bromide-rich phases (see page 19, Chapter 2.4.2). Numerous reports have indicated that the light-induced origin of the process is related to the migration of the ions in hybrid perovskites.[145,146] Interestingly, the process exhibited a reversible behavior and the material can be cycled between segregated and mixed phases by illumination of the material and recovery in the dark.[74]

Intriguingly, for many mixed perovskites the energy of the new phase, as well as the beginning of the miscibility gap depends on the size of A-site cation and lattice parameters of the material. For example, $CH(NH_2)_2Pb(I_{1-x}Br_x)_3$ exhibited a development of the low energy phase at about 1.5 eV, while the band gap of $CH_3NH_3Pb(I_{1-x}Br_x)_3$ can be tuned up to 1.7 eV.[74,82] This observation indicates that the segregation takes place earlier in formamidinium-based perovskites than in methylammonium-based materials. This behavior is possibly related to a stronger mismatch between larger formamidinium cation and the size of cuboctahedral cavity. Since the size of the cavity is determined by the length of Pb-X bonds, the substitution of I with Br leads to a shortening of this distance. This reduction of the Pb-X bond length results in the increase of the incompatibility of the cavity with the size of the cation. Therefore, numerous reports have demonstrated a successful band-gap tuning in $CsPb(I_{1-x}Br_x)_3$ up to 1.9 eV due to the smaller ionic radius of Cs.[83,126]

In this thesis, photo-induced phase segregation and the miscibility gap in $CsPb(I_{1-x}Br_x)_3$ have been investigated. Importantly, the specimens of $CsPb(I_{1-x}Br_x)_3$ were prepared by two

procedures which allows to analyze kinetic and thermodynamic phase stability independently. The two-step procedure is based on the intercalation process, which allows ions to reside at the energetically favorable positions during growth. While the one-step process is based on the quenching of the mixed anion perovskite phase resulting in a statistical distribution of the ions within the material. First, specimens prepared by the one-step spin-coating procedure exhibited an almost linear dependence of the absorption onset on the content of Br. However, the PL spectra of the corresponding specimens revealed a development of the low energy peak upon illumination. The peak exhibited the band gap value of 1.8 eV in contrast to what has been previously reported in literature.[83] Interestingly, the main PL peak continued to follow a linear trend with the increase of the content of Br, as well as the second peak (Figure 48). The observed discrepancy of 0.15 eV between two emission peaks is an indicator for the formation of iodide-rich phase and bromide-rich phase. The PL intensity of the second peak increased upon continuous illumination and dropped to the initial value upon recovery in the dark. This behavior further confirmed the photo-induced origin of the segregation phenomenon, similar to that reported for $CH_3NH_3Pb(I_{1-x}Br_x)_3$.

The samples prepared by the two-step procedure, on the other hand, demonstrate a fundamental irreversible miscibility gap in $CsPb(I_{1-x}Br_x)_3$ mixed perovskites. The specimens where $x > 0.3$ exhibited the presence of two phases in both absorption and PL measurements (Figure 50). The segregation is irreversible and appeared independently on illumination. Most importantly, the PL peak position of the iodide-rich phase saturated at about 1.8 eV corresponding to the composition of $CsPb(I_{0.9}Br_{0.1})_3$, while the position of the PL peak of the bromide-rich phase was no longer following any trend. This behavior clearly indicates a thermodynamic instability of the mixed halide perovskites with high Br content, where $x = 0.3$ is a threshold for the formation of stable mixed halide $CsPb(I_{1-x}Br_x)_3$ materials.

Influence of ethylenediammonium diiodide (EDDI) on $CH_3NH_3PbI_3$

An influence of the size of the cation on the stability of mixed perovskites was investigated by an addition of ethylenediammonium diiodide (EDDI). The addition of EDDI to $CH_3NH_3PbI_3$ led to the drastic change of the optical properties of the mixed $CH_3NH_3PbI_3$/EDDI materials (Figure 52). An increase of the band gap was observed with an increase of the EDDI content in the mixed material. Most importantly, the change of the band gap appeared irreversible and no segregation of the mixed phase was detected. The increase of the band gap is an important phenomenon in hybrid perovskites. Stable tuning of the band gap in a broad range has high strategic importance due to numerous possible applications such as tandem devices and light emitting diodes.[15,17,147–149]

As shown in Chapter 2 (Figure 11), the increase of the band gap occurs as a result of the blending of different halides in the mixed perovskite material. A similar process can be observed in conventional semiconductors. For example, the band gap of III – V semiconducting materials often can be tailored by compositional changes. Pristine gallium nitride (GaN) has the band gap of 3.4 eV.[150] Increase of the bond length between the components by a substitution of N with phosphorous or arsenic led to a decrease of the band gap to 2.26 eV for GaP and 1.424 eV for GaAs.[151,152] Therefore, as a general trend the value of the band gap is inversely proportional to the distance between components in the material i.e. the lattice parameters.[153,154] The trend then suggests that addition of EDDI should result in a decrease of the pseudocubic lattice parameters. However, the experimentally determined lattice parameters indicate the opposite. The increase of the EDDI content led to the increase of the band gap of the $CH_3NH_3PbI_3$/EDDI blends and, at the same time, an increase of the lattice parameters. Therefore, it is likely that the band gap tuning in $CH_3NH_3PbI_3$/EDDI blends is induced by a fundamentally different mechanism.

The inclusion of a large cation in the lattice of $CH_3NH_3PbI_3$ resulted in the presence of a strain similarly to other mixed materials. However, in this case, molecules of EDDI act as a local distortion in the material. This distortion can indirectly influence the lattice parameters and, thus, the band gap of the materials. A similar influence of strain on the band gap was demonstrated in nanowires of crystalline silicon (Si) and gallium arsenide (GaAs).[155,156] Inducing tensile or compressive strain, the band gap in these materials can be tuned over 0.3 eV range.

Stabilization of α-phase of $CsPbI_3$ by addition of ethylenediammonium diiodide (EDDI)

The crystalline lattice of the material determines both the stability and the optical and electronic properties of hybrid perovskites. A substitution of the A-site cation for cesium allows to obtain a fully inorganic perovskite free of the drawbacks related to organic part of the material. However, it has been demonstrated that a mismatch of the size of the A - site cation and inorganic metal-halide network results in the intrinsic instability of $CsPbI_3$.[157] The cubic α- phase of $CsPbI_3$ has a band gap value of 1.75 eV and demonstrated optical and electronic properties that are comparable to $CH_3NH_3PbI_3$. At room temperature, $CsPbI_3$ undergoes a phase transition to an orthorhombic δ-phase, which does not exhibit semiconductor properties.[45] Several reports have demonstrated usage of additives such as hydroiodic acid (HI) and partial substitution with Br to stabilize the photoactive α- phase. The addition of Br leads to the decrease of the formation energy due to the better match of the ionic radius of Cs and size of the cuboctahedral cavity.[158] Thin films containing about 20 % of Br, for example, exhibited a modest stability under ambient conditions. Nevertheless, the addition of a larger amount of Br results in the formation of unstable mixed phases (see Chapter 4.2.3). The work by G. Eperon et al. reported on usage of HI which allows to stabilize the black α-phase of $CsPbI_3$.[56] The addition of HI to the precursor solution of perovskite resulted in the conversion of the material to the photoactive phase at 100 °C. However, usage of aqueous solution of HI resulted in a low stability of the films.

Another approach for stabilization of the α-phase was realized by the formation of $CsPbX_3$ nanocrystallites (Figure 72a). An improved stability of $CsPbI_3$ nanocrystals and layers was reported vastly through the literature.[159,160] In addition, the formation of low dimensional materials by an addition of long-chain alkyl derivatives has been reported previously for stabilization of $CH_3NH_3PbI_3$.[63,161] On the one hand, the addition of molecules led to the formation of a protective coating around perovskite crystallites. This coating often consists of hydrophobic molecules which allow to enhance the stability towards water and oxygen and passivate the surface of crystallites, thereby, stabilizing the perovskite phase. On the other hand, this protective shell acts as an insulation layer that drastically reduces the electronic properties of the materials. As a result, devices based on such 2D materials often suffer from a reduced photocurrent due to the poor transfer and extraction of charge carriers.[66,67]

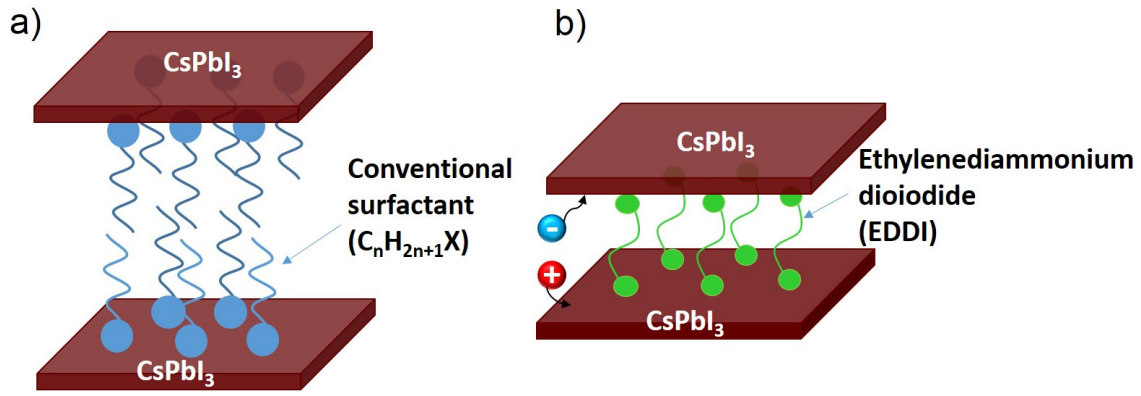

Figure 72. a) Schematic representation of the 2D $CsPbI_3$ obtained by a conventional method. b) 2D $CsPbI_3$ formed by the addition of ethylenediammonium cation.

This thesis, therefore, presents on a new route to stabilize the photoactive α-phase of $CsPbI_3$ by an addition of ethylenediammonium diiodide (EDDI) as shown in Figure 72 (b). Obviously, EDDI is much larger than Cs, thus, the addition of EDDI leads to the formation of a 2D material. However, EDDI is much shorter than typical surfactants used for this purpose, and, therefore, it does not alter the properties of the material. Interestingly, the formation of layered perovskite led to the strong increase of the photoluminescence intensity with the same peak position as pristine $CsPbI_3$ (Figure 61). The unique bifunctional nature of ethylenediammonium cation allows to interlink the layers of $CsPbI_3$ (Figure 72b). Therefore, usage of such a short linker allows to enhance the stability of Cs-based perovskites while maintaining an effective charge carrier transfer.

Photostability: Light-induced degradation of hybrid perovskites

The influence of light on hybrid perovskites was studied with *in-situ* Fourier-transform infrared spectroscopy. The measurements allowed to monitor the change in the IR absorption of the materials under illumination. Remarkably, the common behavior was observed under illumination in vacuum, nitrogen, and argon atmosphere. The degradation of the material occurred due to the loss N-H bonds of the organic cation. The experimental results have indicated that the loss of N-H occurred solely due to illumination and did not depend on used atmosphere or temperature. Thus, the degradation process can be described according to the reaction (23):

$$2CH_3NH_3PbI_{3(s)} + 2e^- \rightarrow CH_3NH_{2(g)}\uparrow + H_{2(g)}\uparrow + I_{2(g)}\uparrow + 2PbI_{2(s)}. \quad (23)$$

$$PbI_{2(s)} \rightarrow Pb_{(s)} + I_{2(g)}\uparrow \quad (24)$$

Since the reaction leads to the formation of two highly volatile products, only the formation of lead iodide is typically observed (Equation 23). Then, light-induced decomposition of lead iodide to metallic lead commences under prolonged illumination (Equation 24, Figure 14, Figure 15, Figure 68).

Typically, the fracture of a bond between atoms occurs as a result of the transfer of an electron to an antibonding orbital. According to density functional theory calculations, the orbitals corresponding to the organic cation are allocated deeply in the valence and conduction bands of $CH_3NH_3PbI_3$ (Figure 73a).[162] Since the degradation occurs primarily at N-H bond (Figure 63), only the molecular orbitals of NH_3 group were considered. According to molecular orbital theory, the NH_3 group poses *C3v* symmetry with a_1, a_2, and e orbitals, where a_1 and e orbitals correspond to N-H bonds. Therefore, the fragmentation of N-H bond occurs once an electron is placed in the antibonding orbitals a_1* and e*. Often, the energy needed for such a transition exceeds the photon energy used in this study. For example, the value of the photo-dissociation energy of the first N-H bond in NH_3 amounts to about 6.4 eV.[163,164] However, the bond dissociation energy should be lower for NH_3^+ cation and might be similar to $CH_3NH_3^+$ in hybrid perovskite. In addition, a dissociation energy of about 2.5 eV/bond was reported for Pb-I, which is in a good agreement with experimental results.[77]

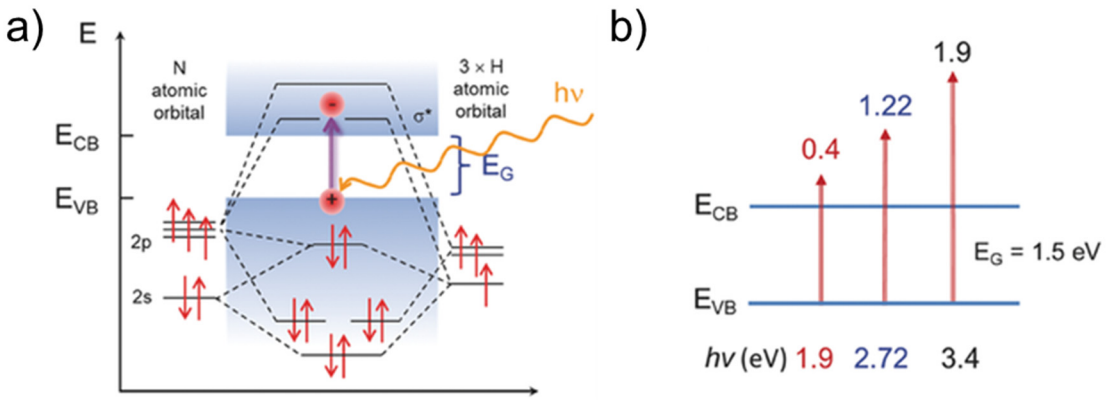

Figure 73. (a) Schematic depiction of the molecular orbitals of ammonia with respect to the conduction, E_{CB}, and valence bands, E_{VB}, of the perovskite. E_G denotes the band gap of the sample. (b) The excitation energies used for the degradation experiments with respect to the band gap of $CH_3NH_3PbI_3$. While all excitation energies are larger than the band gap light-induced degradation is observed only for $h\nu \geq 2.72$ eV. Reproduced with permission from Ref.[165] Copyright 2017, Wiley.

In collaboration with N. Nickel, the influence of the photon energy on the light-induced degradation of hybrid perovskite was studied.[165] The stability of $CH_3NH_3PbI_3$ was investigated with gas effusion method using light emitting diodes with $h\nu = 1.9$, 2.72, and 3.4 eV. Since the excitation occurs from the top of the valence band, the energy needed to excite an electron into the lowest antibonding orbital is reduced. The study revealed that photon energy $h\nu \geq 2.72$ eV is sufficient for decomposition of N-H bond in $CH_3NH_3PbI_3$ (Figure 73b). Moreover, the same photon energy can be used for the photo-dissociation of lead iodide.

Similarly, the light-induced degradation occurs in formamidinium (FA) based perovskites. The data shown in Figure 65a clearly indicated a similar mechanism of the degradation through the dissociation of N-H bonds of organic cation. Interestingly, most of the hybrid perovskites used as absorbers in high-efficiency devices mostly consist of formamidinium and to a lower extent methylammonium, cesium, and rubidium.[166,167] The addition of inorganic cation, Cs, to formamidinium lead iodide ($FA_{0.85}Cs_{0.15}PbI_3$) did not lead to a significant improvement of the stability towards the light (Figure 65b). The degradation process took place already after 100 min under illumination with UV light. Therefore, it is possible to assume that light-induced degradation should occur in other mixed perovskites containing organic cations with weakly bound atoms. Consequently, such light-induced processes need to be taken into account for estimation of the lifetime of the perovskite-based devices and more importantly for a design of new materials.

Conclusions & Outlook

Solvation and complexation of perovskite precursors

The formation of $CH_3NH_3PbI_3$ in solution was studied. A strong interaction between precursors and precursor and solvent molecules was observed. These interactions resulted in the formation of complexes of different structure. Importantly, the formation of polyiodide plumbate complexes, $(PbI_4S_2)_n$, was detected in the solution, where S corresponds to the generic solvent. The formation of polyiodide plumbates was observed independently of the presence of CH_3NH_3I or the solvent used. Similarly to $CH_3NH_3PbI_3$ thin film, the $(PbI_4S_2)_n$ clusters exhibited a photoluminescence peak at about 760 nm. This finding indicates a strong link between emissive properties of PbI_2 complexes in solution and $CH_3NH_3PbI_3$ thin films.

Thermal stability of hybrid perovskites

To investigate the thermal stability, the influence of temperature on the optoelectronic properties of $CH_3NH_3PbI_3$ was studied. The thin films of $CH_3NH_3PbI_3$ were subjected to post-annealing at temperatures ranging from 22 to 250 °C. The swift thermal degradation of $CH_3NH_3PbI_3$ was observed at temperatures above 190 °C. However, at temperatures below 190 °C, $CH_3NH_3PbI_3$ exhibited a thermally activated secondary grain growth with the activation energy of 0.16 eV.

The secondary grain growth below the decomposition temperature was used for an improvement of the morphology of $CH_3NH_3PbI_3$ thin films. By adjusting the temperature and time of the post-annealing process, the grain size of $CH_3NH_3PbI_3$ layers was altered in a range from 150 to 1000 nm. The increase of the grain size led to a drastic enhancement of the optical and electrical properties of the layers. The thin films with 1 μm grain size exhibited a strong increase of the PL intensity by 80 % due to a reduction of the defect density. Moreover, a linear dependence of the diffusion length on the grain size was observed. The diffusion length of the thin films with the average grain size of ≈1050 nm amounted to about 900 nm. In addition, the post-annealed layers were used as the absorber material in solar cells. A vast improvement of the photovoltaic performance to $\eta = 15$ % was demonstrated in solar cell based on $CH_3NH_3PbI_3$ layers with 1 μm grain size.

Compositional stability of hybrid perovskites

Two different mechanisms of compositional instability were investigated within this study. First, the compositional stability of mixed halide $CsPb(I_{1-x}Br_x)_3$ was studied. The phase segregation was observed in specimens with the content of bromide $x > 0.3$. Similarly to $CH_3NH_3Pb(I_{1-x}Br_x)_3$, the segregation of $CsPb(I_{1-x}Br_x)_3$ was triggered by illumination and showed a reversible character. However, the fundamental miscibility gap in $CsPb(I_{1-x}Br_x)_3$ was demonstrated. The specimens containing more than $x = 0.3$ of Br did not follow the Vegard's law and exhibited the formation of iodide- and bromide-rich phases. The iodide-rich phase exhibited a constant value of the band gap of about 1.8 eV independent on the added amount of Br. Therefore, $x = 0.3$ of Br represents a threshold composition for the formation of thermodynamically stable mixed perovskites.

To overcome the phase segregation, a new approach for band gap engineering was developed. The band gap of $CH_3NH_3PbI_3$ perovskite was altered by the addition of a larger cation, ethylenediammonium diiodide (EDDI). The formation of the $CH_3NH_3PbI_3$/EDDI blends led to the drastic change of the optical properties of the materials. A linear dependence of the optical band gap on EDDI molar fraction was observed. The addition of 0.6 % of EDDI allowed to increase the band gap of the $CH_3NH_3PbI_3$/EDDI blend from 1.6 to 1.8 eV. Importantly, the increase of the band gap was irreversible and no phase segregation was detected. In contrast to other semiconductors, the increase of the band gap of the mixed materials was accompanied by the increase of the lattice parameters. This behavior is unconventional and indicates a fundamentally different approach for the band gap engineering. Thus, the changes in optical properties of the blends were attributed to the presence of strain induced by the large cation.

Similarly, the α–phase of $CsPbI_3$ was stabilized through the formation of $CsPbI_3$/EDDI blends. The addition of already 0.25 % of EDDI led to an appearance of a photoluminescence peak at about 710 nm corresponding to the α–phase of $CsPbI_3$. Interestingly, the addition of EDDI did not lead to the shift of the PL peak position. According to the XRD measurements, the stabilization of the α–phase occurs through the formation of a 2D material. Using the unique bifunctional nature of ethylenediammonium cation allows to interlink the layers of $CsPbI_3$. Therefore, the stability of Cs-based perovskites was enhanced while maintaining the properties of the pristine material in the α–phase.

Photo-stability of hybrid perovskite

The photo-stability of hybrid perovskites was studied with *in-situ* Fourier-transform infrared spectroscopy. A common mechanism of the photo-induced degradation of hybrid perovskites was revealed. The specimens illuminated with $h\nu \geq 2.72$ eV exhibited a strong decrease in the intensity of the N-H stretching vibrations. This behavior indicated a dissociation of N-H bonds of the organic cation, $CH_3NH_3^+$. The process occurred independently on the used atmosphere and temperature indicating the solely photo-induced origin of the dissociation. The dissociation reaction led to the formation of volatile products such as CH_3NH_2 and H_2 and remaining PbI_2. Remarkably, the specimens subjected to prolonged illumination exhibited the formation of Pb^0 indicating a further photolysis of PbI_2 under the same conditions.

Similarly, the photo-induced dissociation of the N-H bonds was demonstrated in $CH(NH_2)_2PbI_3$ ($FAPbI_3$) perovskite. In addition, an influence of the inorganic cation on the stability of mixed perovskites was investigated. Interestingly, the mixed cation $Cs_{15}FA_{85}PbI_3$ perovskite exhibited the same mechanism of the photo-induced dissociation as pure $FAPbI_3$.

Outlook

Among different degradation pathways studied in this work, the photo-induced degradation appeared to be particularly important when considering the future applicability of the material. As shown in this work, the usage of methylammonium- and formamidinium-based perovskites in photovoltaic devices would limit their long-term stability. However, the photostability of more complex mixtures of hybrid perovskites comprising methylammonium, formamidinium, cesium, and rubidium and all-inorganic perovskite is still unknown. Therefore, as a next step, stability studies on these systems are required for a better understanding of the degradation processes of hybrid perovskites. The identification of these processes is a necessary step for the rational design of new stable materials. In addition, the results and techniques used in this thesis build the foundation for in-situ degradation measurements of perovskite solar cell during operation. These measurements would provide additional insights into the degradation of perovskite devices required for a design of high-efficient long-term stable solar cells.

References

(1) International Energy Agency. Renewables 2017 https://www.iea.org/publications/renewables2017/#section-6 (accessed Jan 16, 2018).

(2) National Renewable Energy Laboratory (NREL). NREL efficiency chart https://www.nrel.gov/pv/ (accessed Dec 18, 2017).

(3) Ye, F.; Tang, W.; Xie, F.; Yin, M.; He, J.; Wang, Y.; Chen, H.; Qiang, Y.; Yang, X.; Han, L. *Adv. Mater.* **2017**, *29* (35), 1701440.

(4) Hu, X.; Huang, Z.; Zhou, X.; Li, P.; Wang, Y.; Huang, Z.; Su, M.; Ren, W.; Li, F.; Li, M.; Chen, Y.; Song, Y. *Adv. Mater.* **2017**, *29* (42), 1703236.

(5) Song, Z.; McElvany, C. L.; Phillips, A. B.; Celik, I.; Krantz, P. W.; Watthage, S. C.; Liyanage, G. K.; Apul, D.; Heben, M. J. *Energy Environ. Sci.* **2017**, *10* (6), 1297–1305.

(6) Li, Y.; Yan, W.; Li, Y.; Wang, S.; Wang, W.; Bian, Z.; Xiao, L.; Gong, Q.; Wang, S.; Wang, W.; Bian, Z.; Xiao, L.; Gong, Q.; Wang, S.; Wang, W.; Bian, Z.; Xiao, L. *Sci. Rep.* **2015**, *5*, 14485.

(7) Dittrich, T.; Lang, F.; Shargaieva, O.; Rappich, J.; Nickel, N. H.; Unger, E.; Rech, B. *Appl. Phys. Lett.* **2016**, *109* (7), 073901.

(8) Stranks, S. D.; Eperon, G. E.; Grancini, G.; Menelaou, C.; Alcocer, M. J. P.; Leijtens, T.; Herz, L. M.; Petrozza, A.; Snaith, H. J. *Science* **2013**, *342* (6156), 341–344.

(9) Motta, C.; El-Mellouhi, F.; Sanvito, S. *Sci. Rep.* **2015**, *5*, 12746.

(10) Kang, J.; Wang, L.-W. *J. Phys. Chem. Lett.* **2017**, *8*, 489–493.

(11) Reid, O. G.; Yang, M.; Kopidakis, N.; Zhu, K.; Rumbles, G. *ACS Energy Lett.* **2016**, *1*, 561–565.

(12) Herz, L. M. *ACS Energy Lett.* **2017**, *2*, 1539–1548.

(13) Bush, K. A.; Palmstrom, A. F.; Yu, Z. J.; Boccard, M.; Cheacharoen, R.; Mailoa, J. P.; Mcmeekin, D. P.; Hoye, R. L. Z.; Bailie, C. D.; Leijtens, T.; Peters, I. M.; Minichetti, M. C.; Rolston, N.; Prasanna, R.; Sofia, S.; Harwood, D.; Ma, W.; Moghadam, F.; Snaith, H. J.; Buonassisi, T.; Holman, Z. C.; Bent, S. F.; Mcgehee, M. D. *Nat. Energy*

2017, *2* (4), 17009.

(14) Todorov, T.; Gershon, T.; Gunawan, O.; Lee, Y. S.; Sturdevant, C.; Chang, L.-Y.; Guha, S. *Adv. Energy Mater.* **2015**, *5* (23), 1500799.

(15) Jäger, K.; Korte, L.; Rech, B.; Albrecht, S. *Opt. Express* **2017**, *25* (12), A476.

(16) Shi, Z.; Li, X.; Shan, C. In *Quantum-dot Based Light-emitting Diodes*; InTech, 2017.

(17) Zhao, X.; Zhang, B.; Zhao, R.; Yao, B.; Liu, X.; Liu, J.; Xie, Z. *J. Phys. Chem. Lett.* **2016**, *7*, 4259–4266.

(18) Chiba, T.; Hoshi, K.; Pu, Y.-J.; Takeda, Y.; Hayashi, Y.; Ohisa, S.; Kawata, S.; Kido, J. *ACS Appl. Mater. Interfaces* **2017**, *9* (21), 18054–18060.

(19) Zhang, L.; Yang, X.; Jiang, Q.; Wang, P.; Yin, Z.; Zhang, X.; Tan, H.; Yang, Y.; Wei, M.; Sutherland, B. R.; Sargent, E. H.; You, J. *Nat. Commun.* **2017**, *8*, 15640.

(20) Nazarenko, O.; Yakunin, S.; Morad, V.; Cherniukh, I.; Kovalenko, M. V. *NPG Asia Mater.* **2017**, *9*, e373.

(21) Kim, Y. C.; Kim, K. H.; Son, D.-Y.; Jeong, D.-N.; Seo, J.-Y.; Suk Choi, Y.; Taek Han, I.; Yoon Lee, S.; Park, N.-G. *Nature* **2017**, *550*, 87–91.

(22) Rooksby H. P. *Nature* **1945**, *155* (3938), 484–484.

(23) Megaw Helen D. *Nature* **1945**, *155* (3938), 484–485.

(24) Lora Da Silva, E.; Skelton, J. M.; Parker, S. C.; Walsh, A. *Phys. Rev. B* **2015**, *91*, 144107.

(25) Goldschmidt, V. M. *Naturwissenschaften* **1926**, *14* (21), 477–485.

(26) Travis, W.; Glover, E. N. K.; Bronstein, H.; Scanlon, D. O.; Palgrave, R. G. *Chem. Sci.* **2016**, *7* (7), 4548–4556.

(27) Kieslich, G.; Sun, S.; Cheetham, T. *Chem. Sci.* **2015**, *6* (6), 3430–3433.

(28) El-Mellouhi, F.; Bentria, E. T.; Rashkeev, S. N.; Kais, S.; Alharbi, F. H. *Sci. Rep.* **2016**, *6* (1), 30305.

(29) Li, W.; Wang, Z.; Deschler, F.; Gao, S.; Friend, R. H.; Cheetham, A. K. *Nat. Rev. Mater.* **2017**, *2*, 16099.

(30) Filip, M. R.; Eperon, G. E.; Snaith, H. J.; Giustino, F. *Nat. Commun.* **2014**, *5*, 5757.

(31) Li, Z.; Yang, M.; Park, J.-S.; Wei, S.-H.; Berry, J. J.; Zhu, K. *Chem. Mater.* **2015**, *28*, 284–292.

(32) Kojima, A.; Teshima, K.; Shirai, Y.; Miyasaka, T. *J. Am. Chem. Soc.* **2009**, *131* (17), 6050–6051.

(33) Quarti, C.; Mosconi, E.; Ball, J. M.; D'Innocenzo, V.; Tao, C.; Pathak, S.; Snaith, H. J.; Petrozza, A.; De Angelis, F. *Energy Environ. Sci.* **2016**, *9*, 155–163.

(34) Lee, J.-H.; Bristowe, N. C.; Lee, J. H.; Lee, S.-H.; Bristowe, P. D.; Cheetham, A. K.; Jang, H. M. *Chem. Mater.* **2016**, *28*, 4259–4266.

(35) Even, J.; Pedesseau, L.; Katan, C. *J. Phys. Chem. C* **2014**, *118* (22), 11566–11572.

(36) Saidaminov, M. I.; Abdelhady, A. L.; Murali, B.; Alarousu, E.; Burlakov, V. M.; Peng, W.; Dursun, I.; Wang, L.; He, Y.; Maculan, G.; Goriely, A.; Wu, T.; Mohammed, O. F.; Bakr, O. M. *Nat. Commun.* **2015**, *6*, 7586.

(37) De Wolf, S.; Holovsky, J.; Moon, S. J.; Löper, P.; Niesen, B.; Ledinsky, M.; Haug, F. J.; Yum, J. H.; Ballif, C. *J. Phys. Chem. Lett.* **2014**, *5* (6), 1035–1039.

(38) Yin, W. J.; Shi, T.; Yan, Y. *Adv. Mater.* **2014**, *26* (27), 4653–4658.

(39) Correa-Baena, J.-P.; Anaya, M.; Lozano, G.; Tress, W.; Domanski, K.; Saliba, M.; Matsui, T.; Jacobsson, T. J.; Calvo, M. E.; Abate, A.; Grätzel, M.; Míguez, H.; Hagfeldt, A. *Adv. Mater.* **2016**, *28* (25), 5031–5037.

(40) Yang, W. S.; Park, B.-W.; Jung, E. H.; Jeon, N. J.; Kim, Y. C.; Lee, D. U.; Shin, S. S.; Seo, J.; Kim, E. K.; Noh, J. H.; Seok, S. Il. *Science* **2017**, *356*, 1376–1379.

(41) Sutter-Fella, C. M.; Miller, D. W.; Ngo, Q. P.; Roe, E. T.; Toma, F. M.; Sharp, I. D.; Lonergan, M. C.; Javey, A. *ACS Energy Lett.* **2017**, *2* (3), 709–715.

(42) Zhang, W.; Pathak, S.; Sakai, N.; Stergiopoulos, T.; Nayak, P. K.; Noel, N. K.; Haghighirad, A. A.; Burlakov, V. M.; DeQuilettes, D. W.; Sadhanala, A.; Li, W.; Wang, L.; Ginger, D. S.; Friend, R. H.; Snaith, H. J. *Nat. Commun.* **2015**, *6*, 10030.

(43) Pathak, S.; Sepe, A.; Sadhanala, A.; Deschler, F.; Haghighirad, A.; Sakai, N.; Goedel, K. C.; Stranks, S. D.; Noel, N.; Price, M.; Hu, S.; Hawkins, N. a; Friend, R. H.; Steiner, U.; Snaith, H. J. *ACS Nano* **2015**, *9* (3), 2311–2320.

(44) Grancini, G.; D'Innocenzo, V.; Dohner, E. R.; Martino, N.; Srimath Kandada, A. R.;

Mosconi, E.; De Angelis, F.; Karunadasa, H. I.; Hoke, E. T.; Petrozza, A. *Chem. Sci.* **2015**, *6* (12), 7305–7310.

(45) Stoumpos, C. C.; Malliakas, C. D.; Kanatzidis, M. G. *Inorg. Chem.* **2013**, *52*, 9019–9038.

(46) Yamada, Y.; Nakamura, T.; Endo, M.; Wakamiya, A.; Kanemitsu, Y. *J. Am. Chem. Soc.* **2014**, *136* (33), 11610–11613.

(47) D'Innocenzo, V.; Srimath Kandada, A. R.; De Bastiani, M.; Gandini, M.; Petrozza, A. *J. Am. Chem. Soc.* **2014**, *136* (51), 17730–17733.

(48) Adhyaksa, G. W. P.; Veldhuizen, L. W.; Kuang, Y.; Brittman, S.; Schropp, R. E. I.; Garnett, E. C. *Chem. Mater.* **2016**, *28* (15), 5259–5263.

(49) Shargaieva, O.; Lang, F.; Rappich, J.; Dittrich, T.; Klaus, M.; Meixner, M.; Genzel, C.; Nickel, N. H. *ACS Appl. Mater. Interfaces* **2017**, *9* (44), 38428–38435.

(50) Dong, Q.; Fang, Y.; Shao, Y.; Mulligan, P.; Qiu, J.; Cao, L.; Huang, J. *Science* **2015**, *347* (6225), 967–970.

(51) Shockley, W.; Queisser, H. J. *J. Appl. Phys.* **1961**, *32* (3), 510–519.

(52) De Vos, A. *J. Phys. D. Appl. Phys.* **1980**, *13*, 839–846.

(53) Dualeh, A.; Tétreault, N.; Moehl, T.; Gao, P.; Nazeeruddin, M. K.; Grätzel, M. *Adv. Funct. Mater.* **2014**, *24* (21), 3250–3258.

(54) Jeon, N. J.; Noh, J. H.; Yang, W. S.; Kim, Y. C.; Ryu, S.; Seo, J.; Seok, S. Il. *Nature* **2015**, *517* (7535), 476–480.

(55) Lee, J.-W.; Seol, D.-J.; Cho, A.-N.; Park, N.-G. *Adv. Mater.* **2014**, *26* (29), 4991–4998.

(56) Eperon, G. E.; Paternò, G. M.; Sutton, R. J.; Zampetti, A.; Haghighirad, A. A.; Cacialli, F.; Snaith, H. J. *J. Mater. Chem. A* **2015**, *3* (39), 19688–19695.

(57) Niu, G.; Li, W.; Li, J.; Liang, X.; Wang, L. *RSC Adv.* **2017**, *7* (28), 17473–17479.

(58) Leguy, A. M. A.; Hu, Y.; Campoy-Quiles, M.; Alonso, M. I.; Weber, O. J.; Azarhoosh, P.; van Schilfgaarde, M.; Weller, M. T.; Bein, T.; Nelson, J.; Docampo, P.; Barnes, P. R. F. *Chem. Mater.* **2015**, *27* (9), 3397–3407.

(59) Kim, G.-W.; Kang, G.; Malekshahi Byranvand, M.; Lee, G.-Y.; Park, T. *ACS Appl.*

Mater. Interfaces **2017**, *9* (33), 27720–27726.

(60) Hwang, I.; Jeong, I.; Lee, J.; Ko, M. J.; Yong, K. *ACS Appl. Mater. Interfaces* **2015**, *7* (31), 17330–17336.

(61) Kim, G.-H.; Jang, H.; Yoon, Y. J.; Jeong, J.; Park, S. Y.; Walker, B.; Jeon, I.-Y.; Jo, Y.; Yoon, H.; Kim, M.; Baek, J.-B.; Kim, D. S.; Kim, J. Y. *Nano Lett.* **2017**, *17* (10), 6385–6390.

(62) Yoo, J. S.; Han, G. S.; Lee, S.; Kim, M. C.; Choi, M.; Jung, H. S.; Lee, J.-K. *Nano Res.* **2017**, *10* (11), 3885–3895.

(63) Smith, I. C.; Hoke, E. T.; Solis-Ibarra, D.; McGehee, M. D.; Karunadasa, H. I. *Angew. Chemie - Int. Ed.* **2014**, *53* (42), 11232–11235.

(64) Mitzi, D. B.; Wang, S.; Feild, C. A.; Chess, C. A.; Guloy, A. M. *Science* **1995**, *267* (5203), 1473–1476.

(65) Wang, Z.; Lin, Q.; Chmiel, F. P.; Sakai, N.; Herz, L. M.; Snaith, H. J. *Nat. Energy* **2017**, *2*, 17135.

(66) Jia, G.; Shi, Z.-J.; Xia, Y.-D.; Wei, Q.; Chen, Y.-H.; Xing, G.-C.; Huang, W. *Opt. Express* **2018**, *26* (2), 66–74.

(67) Chen, Y.; Sun, Y.; Peng, J.; Zhang, W.; Su, X.; Zheng, K.; Pullerits, T.; Liang, Z. *Adv. Energy Mater.* **2017**, *7* (18), 1700162.

(68) Zhang, X.; Ren, X.; Liu, B.; Munir, R.; Zhu, X.; Yang, D.; Li, J.; Liu, Y.; Smilgies, D.-M.; Li, R.; Yang, Z.; Niu, T.; Wang, X.; Amassian, A.; Zhao, K.; Liu, S. *Energy Environ. Sci.* **2017**, *10* (10), 2095–2102.

(69) Grancini, G.; Roldán-Carmona, C.; Zimmermann, I.; Mosconi, E.; Lee, X.; Martineau, D.; Narbey, S.; Oswald, F.; De Angelis, F.; Graetzel, M.; Nazeeruddin, M. K. *Nat. Commun.* **2017**, *8*, 15684.

(70) Noh, J. H.; Im, S. H.; Heo, J. H.; Mandal, T. N.; Seok, S. Il. *Nano Lett.* **2013**, *13* (4), 1764–1769.

(71) Vegard, L. *Zeitschrift für Phys.* **1921**, *5* (1), 17–26.

(72) Park, B.; Philippe, B.; Jain, S. M.; Zhang, X.; Edvinsson, T.; Rensmo, H.; Zietz, B.; Boschloo, G. *J. Mater. Chem. A* **2015**, *3* (43), 21760–21771.

(73) Fedeli, P.; Gazza, F.; Calestani, D.; Ferro, P.; Besagni, T.; Zappettini, A.; Calestani, G.; Marchi, E.; Ceroni, P.; Mosca, R. *J. Phys. Chem. C* **2015**, *119* (37), 21304–21313.

(74) Hoke, E. T.; Slotcavage, D. J.; Dohner, E. R.; Bowring, A. R.; Karunadasa, H. I.; McGehee, M. D. *Chem. Sci.* **2015**, *6* (1), 613–617.

(75) Slotcavage, D. J.; Karunadasa, H. I.; Mcgehee, M. D. *ACS Energy Lett.* **2016**, *1* (6), 1199–1205.

(76) Kuku, T. A.; Salau, A. M. *Solid State Ionics* **1987**, *25* (1), 1–7.

(77) Albrecht, M. G.; Green, M. *Phys. Chem. Solids* **1977**, *38*, 297–306.

(78) Eames, C.; Frost, J. M.; Barnes, P. R. F.; O 'regan, B. C.; Walsh, A.; Islam, M. S. *Nat. Commun.* **2015**, *6*, 7497.

(79) Brennan, M. C.; Draguta, S.; Kamat, P. V.; Kuno, M. *ACS Energy Lett.* **2018**, *3* (1), 204–213.

(80) Azpiroz, J. M.; Mosconi, E.; Bisquert, J.; De Angelis, F. *Energy Environ. Sci.* **2015**, *8* (7), 2118–2127.

(81) Bischak, C. G.; Hetherington, C. L.; Wu, H.; Aloni, S.; Frank Ogletree, D.; Limmer, D. T.; Ginsberg, N. S. *Nano Lett.* **2017**, *17* (2), 1028–1033.

(82) Jacobsson, J. T.; Correa-Baena, J.-P.; Pazoki, M.; Saliba, M.; Schenk, K.; Grätzel, M.; Hagfeldt, A. *Energy Environ. Sci.* **2016**, *9* (5), 1706–1724.

(83) Beal, R. E.; Slotcavage, D. J.; Leijtens, T.; Bowring, A. R.; Belisle, R. A.; Nguyen, W. H.; Burkhard, G. F.; Hoke, E. T.; McGehee, M. D. *J. Phys. Chem. Lett.* **2016**, *7* (5), 746–751.

(84) Colella, S.; Mosconi, E.; Pellegrino, G.; Alberti, A.; Guerra, V. L. P.; Masi, S.; Listorti, A.; Rizzo, A.; Condorelli, G. G.; De Angelis, F.; Gigli, G. *J. Phys. Chem. Lett.* **2014**, *5*, 3532–3538.

(85) Han, Y.; Meyer, S.; Dkhissi, Y.; Weber, K.; Pringle, J. M.; Bach, U.; Spiccia, L.; Cheng, Y.-B. *J. Mater. Chem. A* **2015**, *3* (15), 8139–8147.

(86) Guarnera, S.; Abate, A.; Zhang, W.; Foster, J. M.; Richardson, G.; Petrozza, A.; Snaith, H. J. *J. Phys. Chem. Lett.* **2015**, *6* (3), 432–437.

(87) Leijtens, T.; Eperon, G. E.; Pathak, S.; Abate, A.; Lee, M. M.; Snaith, H. J. *Nat.*

Commun. **2013**, *4*, 2885.

(88) Jørgensen, M.; Norrman, K.; Krebs, F. C. *Sol. Energy Mater. Sol. Cells* **2008**, *92*, 686–714.

(89) Sun, Y.; Fang, X.; Ma, Z.; Xu, L.; Lu, Y.; Yu, Q.; Yuan, N.; Ding, J. *J. Mater. Chem. C* **2017**, *5* (34), 8682–8687.

(90) Habisreutinger, S. N.; Leijtens, T.; Eperon, G. E.; Stranks, S. D.; Nicholas, R. J.; Snaith, H. J. *Nano Lett.* **2014**, *14* (10), 5561–5568.

(91) Liu, J.; Wu, Y.; Qin, C.; Yang, X.; Yasuda, T.; Islam, A.; Zhang, K.; Peng, W.; Chen, W.; Han, L. *Energy Environ. Sci.* **2014**, *7* (9), 2963–2967.

(92) Guarnera, S.; Abate, A.; Zhang, W.; Foster, J. M.; Richardson, G.; Petrozza, A.; Snaith, H. J. *J. Phys. Chem. Lett.* **2015**, *6*, 432–437.

(93) Luo, Q.; Zhang, Y.; Liu, C.; Li, J.; Wang, N.; Lin, H. *J. Mater. Chem. A* **2015**, *3* (31), 15996–16004.

(94) You, J.; Meng, L.; Song, T.-B.; Guo, T.-F.; Yang, Y. (Michael); Chang, W.-H.; Hong, Z.; Chen, H.; Zhou, H.; Chen, Q.; Liu, Y.; De Marco, N.; Yang, Y. *Nat. Nanotechnol.* **2015**, *11* (1), 75–81.

(95) Ginting, R. T.; Jeon, M.-K.; Lee, K.-J.; Jin, W.-Y.; Kim, T.-W.; Kang, J.-W. *J. Mater. Chem. A* **2017**, *5* (9), 4527–4534.

(96) Joshi, P. H.; Zhang, L.; Hossain, I. M.; Abbas, H. A.; Kottokkaran, R.; Nehra, S. P.; Dhaka, M.; Noack, M.; Dalal, V. L. *AIP Adv.* **2016**, *6* (11), 115114.

(97) Nie, W.; Blancon, J.-C.; Neukirch, A. J.; Appavoo, K.; Tsai, H.; Chhowalla, M.; Alam, M. A.; Sfeir, M. Y.; Katan, C.; Even, J.; Tretiak, S.; Crochet, J. J.; Gupta, G.; Mohite, A. D. *Nat. Commun.* **2016**, *7*, 11574.

(98) Lee, S.-W.; Kim, S.; Bae, S.; Cho, K.; Chung, T.; Mundt, L. E.; Lee, S.; Park, S.; Park, H.; Schubert, M. C.; Glunz, S. W.; Ko, Y.; Jun, Y.; Kang, Y.; Lee, H.-S.; Kim, D. *Sci. Rep.* **2016**, *6*, 38150.

(99) Zu, F.-S.; Amsalem, P.; Salzmann, I.; Wang, R.-B.; Ralaiarisoa, M.; Kowarik, S.; Duhm, S.; Koch, N. *Adv. Opt. Mater.* **2017**, *5* (9), 1700139.

(100) Tang, X.; Brandl, M.; May, B.; Levchuk, I.; Hou, Y.; Richter, M.; Chen, H.; Chen, S.;

Kahmann, S.; Osvet, A.; Maier, F.; Steinrück, H.-P.; Hock, R.; Matt, G. J.; Brabec, C. J. *J. Mater. Chem. A* **2016**, *4* (41), 15896–15903.

(101) Dawood R.I.; Forty A.J.; Tubbs M.R. In *Proceedings of the Royal Society of London*; The Royal Society, 1965; Vol. 284, pp 1–21.

(102) Tubbs, M. R.; Forty, A. J. *Br. J. Appl. Phys.* **1964**, *15*, 1553–1558.

(103) Bragg, W. H.; Bragg, W. L. *Proc. R. Soc. London A Math. Phys. Eng. Sci.* **1913**, *88* (605), 428–438.

(104) Warren, B. E. *X-ray Diffraction*; Dover Publication: New York, 1990.

(105) Patterson, A. L. *Phys. Rev.* **1939**, *56* (10), 978–982.

(106) Williamson, G. K.; Hall, W. H. *Acta Metall.* **1953**, *1* (1), 22–31.

(107) Kronik, L.; Shapira, Y. *Surf. Sci. Rep.* **1999**, *37* (1–5), 1–206.

(108) Goodman, A. M. *J. Appl. Phys.* **1961**, *32* (12), 2550–2552.

(109) Hollas, J. M. *Modern spectroscopy*; Wiley, 2004.

(110) Würfel, P. *Physics of solar cells : from basic principles to advanced concepts*; Wiley-VCH, 2009.

(111) Jeon, N. J.; Noh, J. H.; Kim, Y. C.; Yang, W. S.; Ryu, S.; Seok, S. Il. *Nat. Mater.* **2014**, *13* (9), 897–903.

(112) Pérez-Osorio, M. A.; Milot, R. L.; Filip, M. R.; Patel, J. B.; Herz, L. M.; Johnston, M. B.; Giustino, F. *J. Phys. Chem. C* **2015**, *119* (46), 25703–25718.

(113) Stamplecoskie, K. G.; Manser, J. S.; Kamat, P. V. *Energy Environ. Sci.* **2015**, *8* (1), 208–215.

(114) Ahuja, R.; Arwin, H.; Ferreira Da Silva, A.; Persson, C.; Osorio-Guillén, J. M.; Souza De Almeida, J.; Araujo, C. M.; Veje, E.; Veissid, N.; An, C. Y.; Pepe, I.; Johansson, B. *J. Appl. Phys.* **2002**, *92* (12), 7219–7224.

(115) Nie, W.; Tsai, H.; Asadpour, R.; Blancon, J.; Neukirch, A. J.; Gupta, G.; Crochet, J. J.; Chhowalla, M.; Tretiak, S.; Alam, M. A.; Wang, H.; Mohite, A. D. *Science* **2015**, *347* (6221), 522–525.

(116) Weber, D. *Z. Naturforsch.* **1978**, *33*, 1443–1445.

(117) Noel, N. K.; Habisreutinger, S. N.; Wenger, B.; Klug, M. T.; Hörantner, M. T.; Johnston, M. B.; Nicholas, R. J.; Moore, D. T.; Snaith, H. J. *Energy Environ. Sci.* **2017**, *10* (1), 145–152.

(118) Manser, J. S.; Saidaminov, M. I.; Christians, J. A.; Bakr, O. M.; Kamat, P. V. *Acc. Chem. Res.* **2016**, *49*, 330–338.

(119) Joon Yoon, S.; Stamplecoskie, K. G.; Kamat, P. V. *J. Phys. Chem. Lett.* **2016**, *7*, 1368–1373.

(120) Guo, Y.; Shoyama, K.; Sato, W.; Matsuo, Y.; Inoue, K.; Harano, K.; Liu, C.; Tanaka, H.; Nakamura, E. *J. Am. Chem. Soc.* **2015**, *137*, 15907–15914.

(121) National Institute of Standards and Technology. Evaluated Infrared Spectra http://webbook.nist.gov/chemistry/coblentz/ (accessed Jan 21, 2018).

(122) Condeles, J. F.; Ando, R. A.; Mulato, M. *J. Mater. Sci.* **2008**, *43* (2), 525–529.

(123) Song, Z.; Watthage, S. C.; Phillips, A. B.; Tompkins, B. L.; Ellingson, R. J.; Heben, M. J. *Chem. Mater.* **2015**, *27* (13), 4612–4619.

(124) Baikie, T.; Fang, Y.; Kadro, J. M.; Schreyer, M.; Wei, F.; Mhaisalkar, S. G.; Gratzel, M.; White, T. J. *J. Mater. Chem. A* **2013**, *1* (18), 5628–5641.

(125) Im, J.-H.; Lee, C.-R.; Lee, J.-W.; Park, S.-W.; Park, N.-G. *Nanoscale* **2011**, *3*, 4088–4093.

(126) Sutton, R. J.; Eperon, G. E.; Miranda, L.; Parrott, E. S.; Kamino, B. A.; Patel, J. B.; Hörantner, M. T.; Johnston, M. B.; Haghighirad, A. A.; Moore, D. T.; Snaith, H. J. *Adv. Energy Mater.* **2016**, *6* (8), 1502458.

(127) McKinnon, N. K.; Reeves, D. C.; Akabas, M. H. *J. Gen. Physiol.* **2011**, *138* (4), 453–466.

(128) Supasai, T.; Rujisamphan, N.; Ullrich, K.; Chemseddine, A.; Dittrich, T. *Appl. Phys. Lett.* **2013**, *103* (18), 183906.

(129) Wyckoff, R. W. G. *Crystal Structures*, 2nd ed.; Wiley, 1963.

(130) Ahn, N.; Son, D. Y.; Jang, I. H.; Kang, S. M.; Choi, M.; Park, N. G. *J. Am. Chem. Soc.* **2015**, *137* (27), 8696–8699.

(131) Stewart, R. J.; Grieco, C.; Larsen, A. V.; Doucette, G. S.; Asbury, J. B. *J. Phys. Chem.*

C **2016**, *120*, 12392–12402.

(132) Rahimnejad, S.; Kovalenko, A.; Forøs, S.; Aranda, C.; Guerrero, A. *ChemPhysChem* **2016**, *17*, 2795–2798.

(133) Kim, N.-K.; Min, Y. H.; Noh, S.; Cho, E.; Jeong, G.; Joo, M.; Ahn, S.-W.; Lee, J. S.; Kim, S.; Ihm, K.; Ahn, H.; Kang, Y.; Lee, H.-S.; Kim, D. *Sci. Rep.* **2017**, *7*, 4645.

(134) Brunetti, B.; Cavallo, C.; Ciccioli, A.; Gigli, G.; Latini, A. *Sci. Rep.* **2016**, *6*, 31896.

(135) Dualeh, A.; Gao, P.; Seok, S. Il; Nazeeruddin, M. K.; Grätzel, M. *Chem. Mater.* **2014**, *26*, 6160–6164.

(136) Ishida, H.; Ikeda, R.; Nakamura, D. *Phys. status solidi* **1982**, *70* (2), 151–154.

(137) Padture, N. P.; Lawn, B. R. *J. Am. Ceram. Soc.* **1994**, *77* (10), 2518–2522.

(138) Rečnik, A.; Čeh, M.; Kolar, D. *J. Eur. Ceram. Soc.* **2001**, *21* (10), 2117–2121.

(139) Thompson, C. V. *J. Appl. Phys.* **1985**, *58* (2), 763.

(140) Yonehara, T.; Smith, H. I.; Thompson, C. V.; Palmer, J. E. *Appl. Phys. Lett.* **1984**, *45* (6), 631–633.

(141) Thompson, C. V.; Smith, H. I. *Appl. Phys. Lett.* **1984**, *44* (6), 603–605.

(142) Nakhodkin, N. G.; Rodionova, T. V. *J. Cryst. Growth* **1997**, *171*, 50–55.

(143) Wada, Y.; Nishimatsu, S. *J. Electrochem. Soc.* **1978**, *125* (9), 1499.

(144) Kim, H.-J.; Thompson, C. V. *J. Appl. Phys.* **1990**, *67* (2), 757–767.

(145) Brivio, F.; Caetano, C.; Walsh, A. *J. Phys. Chem. Lett.* **2016**, *7*, 1083–1087.

(146) Yoon, S. J.; Draguta, S.; Manser, J. S.; Sharia, O.; Schneider, W. F.; Kuno, M.; Kamat, P. V. *ACS Energy Lett.* **2016**, *1*, 290–296.

(147) Albrecht, S.; Saliba, M.; Correa-Baena, J.-P.; Jäger, K.; Korte, L.; Hagfeldt, A.; Grätzel, M.; Rech, B. *J. Opt.* **2016**, *18* (6), 064012.

(148) McMeekin, D. P.; Sadoughi, G.; Rehman, W.; Eperon, G. E.; Saliba, M.; Horantner, M. T.; Haghighirad, A.; Sakai, N.; Korte, L.; Rech, B.; Johnston, M. B.; Herz, L. M.; Snaith, H. J. *Science* **2016**, *351* (6269), 151–155.

(149) Veldhuis, S. A.; Boix, P. P.; Yantara, N.; Li, M.; Sum, T. C.; Mathews, N.;

Mhaisalkar, S. G. *Adv. Mater.* **2016**, *28*, 6804–6834.

(150) Roy, R. K.; Bhattacharyya, S. R.; Bandyopadhayay, S.; Pal, A. K. *Thin Solid Films* **2006**, *500* (1–2), 144–151.

(151) Akinlami, J. O.; Ashamu, A. O. *J. Semicond.* **2013**, *34* (3), 032002.

(152) Aspnes, D. E.; Studna, A. A. *Phys. Rev. B* **1983**, *27* (2), 985–1009.

(153) Dalven, R. *Phys. Rev. B* **1973**, *8* (12), 6033–6034.

(154) Dittrich, T. *Materials Concepts for Solar Cells*; Imperial College Press, 2014.

(155) Cai, J.; Ishikawa, Y.; Wada, K. *Opt. Express* **2013**, *21* (6), 7162–7170.

(156) Liao, Z.-M.; Wu, H.-C.; Fu, Q.; Fu, X.; Zhu, X.; Xu, J.; Shvets, I. V; Zhang, Z.; Guo, W.; Leprince-Wang, Y.; Zhao, Q.; Wu, X.; Yu, D.-P. *Sci. Rep.* **2012**, *2*, 452.

(157) Møller, C. K. *Mat. Fys. Medd . Dan . Vid . Selsk* **1959**, *32* (2), 1–27.

(158) Yin, W.-J.; Yan, Y.; Wei, S.-H. *J. Phys. Chem. Lett.* **2014**, *5*, 3625–3631.

(159) Wu, L.; Zhong, Q.; Yang, D.; Chen, M.; Hu, H.; Pan, Q.; Liu, H.; Cao, M.; Xu, Y.; Sun, B.; Zhang, Q. *Langmuir* **2017**, *33*, 12689–12696.

(160) Gomez, L.; de Weerd, C.; Hueso, J. L.; Gregorkiewicz, T. *Nanoscale* **2017**, *9* (2), 631–636.

(161) Stoumpos, C. C.; Cao, D. H.; Clark, D. J.; Young, J.; Rondinelli, J. M.; Jang, J. I.; Hupp, J. T.; Kanatzidis, M. G. *Chem. Mater.* **2016**, *28* (8), 2852–2867.

(162) Wang, Y.; Gould, T.; Dobson, J. F.; Zhang, H.; Yang, H.; Yao, X.; Zhao, H. *Phys. Chem. Chem. Phys.* **2014**, *16*, 1424–1429.

(163) Biesner, J.; Schnieder, L.; Schmeer, J.; Ahlers, G.; Xie, X.; Welge, K. H.; Ashfold, M. N. R.; Dixon, R. N. *J. Chem. Phys.* **1988**, *88* (6), 3607–3616.

(164) Woodbridge, E. L.; Ashfold, M. N. R.; Leone, S. R. *J. Chem. Phys.* **1991**, *94* (6), 4195–4204.

(165) Nickel, N. H.; Lang, F.; Brus, V. V.; Shargaieva, O.; Rappich, J. *Adv. Electron. Mater.* **2017**, *3* (12), 1700158.

(166) Saliba, M.; Matsui, T.; Seo, J.-Y.; Domanski, K.; Correa-Baena, J.-P.; Nazeeruddin, M. K.; Zakeeruddin, S. M.; Tress, W.; Abate, A.; Hagfeldt, A.; Gräzel, M. *Energy*

Environ. Sci. **2016**, *9* (6), 1989–1997.

(167) Saliba, M.; Matsui, T.; Domanski, K.; Seo, J.-Y.; Ummadisingu, A.; Zakeeruddin, S. M.; Correa-Baena, J.-P.; Tress, W. R.; Abate, A.; Hagfeldt, A.; Grätzel, M. *Science* **2016**, *354* (6309), 206–209.

Publications

Peer-reviewed journal articles

(1) Shargaieva, O.; Lang, F.; Rappich, J.; Dittrich, T.; Klaus, M.; Meixner, M.; Genzel, C.; Nickel, N. H. The Influence of the Grain Size on the Properties of $CH_3NH_3PbI_3$ Thin Films. *ACS Appl. Mater. Interfaces* **2017**, 9 (44), 38428–38435.

(2) Nickel, N. H.; Lang, F.; Brus, V. V.; Shargaieva, O.; Rappich, J. Unraveling the Light-Induced Degradation Mechanisms of $CH_3NH_3PbI_3$ Perovskite Films. *Adv. Electron. Mater.* **2017**, 3 (12), 1700158.

(3) Lang, F.; Shargaieva, O.; Brus, V. V.; Neitzert, H. C.; Rappich, J.; Nickel, N. H. Influence of Radiation on the Properties and the Stability of Hybrid Perovskites. *Adv. Mater.* **2018**, 30 (3), 1702905.

(4) Eisenhauer, D.; Köppel, G.; Jäger, K.; Chen, D.; Shargaieva, O.; Sonntag, P.; Amkreutz, D.; Rech, B.; Becker, C. Smooth Anti-Reflective Three-Dimensional Textures for Liquid Phase Crystallized Silicon Thin-Film Solar Cells on Glass. *Sci. Rep.* **2017**, 7 (1), 1–10.

(5) Lang, F.; Gluba, M. A.; Albrecht, S.; Shargaieva, O.; Rappich, J.; Korte, L.; Rech, B.; Nickel, N. H. In Situ Graphene Doping as a Route toward Efficient Perovskite Tandem Solar Cells. *Phys. status solidi* **2016**, 213 (7), 1629–1629.

(6) Dittrich, T.; Lang, F.; Shargaieva, O.; Rappich, J.; Nickel, N. H.; Unger, E.; Rech, B. Diffusion Length of Photo-Generated Charge Carriers in Layers and Powders of $CH_3NH_3PbI_3$ Perovskite. *Appl. Phys. Lett*. **2016**, 109 (7), 73901.

(7) Dittrich, T.; Shargaieva, O.; Lang, F.; Nickel, N. H.; Rech, B.; Rappich, J. Dependence of the Transport Length in $CH_3NH_3PbI_3$ Powders on Light Soaking: A Surface Photovoltage Study. *32nd Eur. Photovolt. Sol. Energy Conf. Exhib.* **2016**, 1104–1107.

Conference contributions

Talks

Shargaieva, Oleksandra; Lang, Felix; Rappich, Jörg; Nickel, Norbert: A novel cation for hybrid perovskite band gap tuning, International Conference on Hybrid and Organic Photovoltaics (HOPV 17) Lausanne, Switzerland, 21.05.2017 - 24.05.2017

Shargaieva, Oleksandra; Lang, Felix; Rappich, Jörg; Dittrich, Thomas; Rech, Bernd; Nickel, Norbert: Influence of the grain size on electronic properties of methylammonium lead iodide, DPG Spring Meeting 2017, Dresden, Germany, 19.03.2017 - 24.03.2017

Shargaieva, Oleksandra; Lang, Felix; Rappich, Jörg; Klimm, Carola; Klaus, Manuela; Rech, Bernd; Nickel, Norbert: Micrometer size grains of hybrid perovskite through rapid melting procedure, DPG Spring Meeting, Regensburg, Germany, 06.03.2016 - 11.03.2016

Posters

Shargaieva, Oleksandra; Lang, Felix; Awino, Celline; Rappich, Jörg; Nickel, Norbert: Band gap tuning at the limits of the tolerance factor, The 3rd International Conference on Perovskite Solar Cells and Optoelectronics (PSCO 2017), Oxford, United Kingdom, 18.09.2017 - 20.09.2017

Shargaieva, Oleksandra; Lang, Felix; Dittrich, Thomas; Rappich, Jörg; Rech, Bernd; Nickel, Norbert: Grain size versus transport length in hybrid perovskite, The 2nd International Conference on Perovskite Solar Cells and Optoelectronics, Genova, Italy, 26.10.2016 - 28.10.2016

Shargaieva, Oleksandra; Lang, Felix; Rappich, Jörg; Klimm, Carola; Klaus, Manuela; Rech, Bernd; Nickel, Norbert: Micrometer size grains of hybrid perovskite through rapid melting procedure, International Conference on Hybrid and Organic Photovoltaics (HOPV16), Swansea, United Kingdom, 28.06.2016 - 01.07.2016

Shargaieva, Oleksandra; Lang, Felix; Rappich, Jörg; Klimm, Carola; Klaus, Manuela; Rech, Bernd; Nickel, Norbert: Micrometer size grains of hybrid perovskite through rapid melting procedure, Hybrid-Photovoltaics 2015 Symposium, Berlin, Germany, 10.12.2015 - 11.12.2015

Acknowledgements

First of all, I would like to express my gratitude to Prof. Dr. Klaus Rademann and Prof. Dr. Norbert Koch who kindly agreed to review this thesis. Especially, I would like to thank my mentor, Prof. Dr. Norbert Nickel, for giving me this opportunity to work on such an exciting topic as hybrid perovskites. Moreover, I wish to thank him for his guidance and inspiration during my work on this thesis.

I would like to acknowledge graduate school “Hybrid 4 Energy” for financial support and for this exclusive experience of being a member of a group of doctoral students from different parts of the world and science.

Also, I would like to thank Dr. Jörg Rappich, who always had time, patience, and often solution for my troubles. I thank Dr. Thomas Dittrich for investigation of my samples with surface photovoltage method and his expertise in so many different areas. Likewise, I thank Dr. Eva Unger for long and thoughtful discussions, which became my source of inspiration.

In addition, I would like to thank all of my colleges at Helmholtz Zentrum Berlin for their help, support, and friendly smile. Especially, I thank Marion Krusche for her constant help with paperwork and fighting with bureaucracy. I thank Carola Klimm for countless hours spent next to the microscope and beautiful pictures of my samples. In addition, I wish to thank Carola Ferber, Thomas Lüßky, and Andreas von Kozierowski for their technical support, which ensured smooth working in the labs.

I would like to thank my fellows from perovskite team and the group of N.H. Nickel for great experiments, discussions, and results. Especially, I thank Lukas and Marko for bringing a fun component in a daily working in labs. Also, I am grateful to Jessica Hänisch, my dedicated translator, who helped me so many times beyond count. I would like to thank Dr. Matthias Zellmeier and Dr. Felix Lang for a lot of fun, support, discussions, and proofreading. I highly appreciate the help of all my other collaborators, who have been essential for the work presented in this thesis.

Selbstständigkeitserklärung

Ich erkläre, dass ich die Dissertation selbständig und nur unter Verwendung der von mir gemäß § 7 Abs. 3 der Promotionsordnung der Mathematisch-Naturwissenschaftlichen Fakultät, veröffentlicht im Amtlichen Mitteilungsblatt der Humboldt-Universität zu Berlin Nr. 126/2014 am 18.11.2014 angegebenen Hilfsmittel angefertigt habe.

Berlin, den

_____

Oleksandra Shargaieva